Montanuniversität Leoben

Dissertation

Deformation-induced supersaturation of immiscible binary systems

Karoline Sophie Kormout

Leoben, November 2016

This work was financially supported by the Austrian Science Fund (FWF) in the framework of research project P24429 and by the European Research Council under ERC Grant Agreement No. 340185 USMS.

Erich Schmid Institute of Materials Science
Austrian Academy of Sciences
Jahnstraße 12
A-8700 Leoben

Affidavit

I declare in lieu of oath, that I wrote this thesis and performed the associated research myself, using only literature cited in this volume.

Karoline Sophie Kormout

Leoben, November 2016

Danksagung

Zuallererst möchte ich mich bei meinem Betreuer Prof. Reinhard Pippan für die Vergabe dieser Arbeit bedanken. Sein großes Wissen, sein unverbesserlicher Optimismus und seine grenzenlose Geduld haben die letzten Jahre wie im Flug vergehen lassen.

Vielen Dank an all die netten und hilfsbereiten Menschen des Erich Schmid Instituts. Besonderer Dank gilt Gabi und Wicki Felber für die großartige Unterstützung in allen TEM Angelegenheiten und Silke Modritsch für die unermüdliche Präparation in der Metallographie. Vielen Dank an Franz Hubner und Robin Neubauer für die schnelle Erledigung vieler Arbeiten in der Werkstatt. Bedanken möchte ich mich auch ganz herzlich bei Viktoria Schrutt, Daniela Brunner und Sabine Wilfling für die große Hilfe bei organisatorischen Angelegenheiten und das Hinwegsehen über meine oft mangelhaften Abrechnungen. Ein herzliches Danke an Peter Kutleša, der mir stets bei der HPT zu Hilfe war und mir mit seinem Humor in unzähligen Rauchpausen den Tag erleichtert hat. Vielen Dank auch an meine studentischen Mitarbeiter Magdalena Vasileva und Stefan Zeiler für ihr Fingerspitzengefühl und ihre endlose Geduld in der TEM Präparation.

Ein besonderer Dank geht an meine Bürokollegen, Peter Imrich, „Joe“ Xiang Zhou, Michael Reisinger und Manuel Pfeifenberger für die lustigen Gespräche und die entspannte Atmosphäre und natürlich an Thomas Leitner, für viele gemeinsame Höhen und Tiefen im Dissertantenleben und dafür, dass ich unsere Wette gewinnen durfte. Bei Toni Hohenwarter möchte ich mich für seine große Unterstützung während der letzten kritischen Monate und für die vielen Nachhilfestunden und Therapiesitzungen im Stadtcafé bedanken. Vielen Dank an meine TEM-Leidensgenossen Bernhard Völker und Tristan Harzer für viele motivierende Gespräche und an Stefan Wurster für die Weitergabe seiner Lebensweisheiten. Ein großer Dank geht auch an Lisa Krämer und Benjamin Schuh für viele schöne Stunden bei Konferenzen und ihre kulinarische Unterstützung. Außerdem möchte ich mich bei Andrea Bachmaier für jegliche Hilfe bei der Arbeit und viele anregende After-work-Besprechungen bedanken. Ein herzliches Danke auch an Marlene Kapp, Oliver Renk, Verena Maier-Kiener und Daniel Kiener für die gemeinsamen Stunden auf Konferenzen und abseits der Arbeit.

Vielen Dank an meine Freundinnen Irene Klissenbauer, Jennifer Freund und Christina Hofer, die mir immer zur Seite stehen.

Zuletzt möchte ich mich ganz herzlich bei meiner Familie bedanken. Allen voran meinen Eltern und meinen Omas für ihre grenzenlose und unermüdliche Unterstützung. Meinen Geschwistern Lisa, Joe, Ella, Fanny und Lenni möchte ich für die große moralische Unterstützung danken und dafür, dass immer was los ist, wenn ich nachhause komme.

Abstract

Metals immiscible in thermodynamic equilibrium can be forced into a metastable supersaturated state through plastic deformation as evidenced in numerous studies. Despite detailed investigations in the last decades, the underlying processes and the key parameters controlling deformation-induced supersaturation are still a controversial issue.

To understand how deformation-induced supersaturation is realized the fundamental deformation behaviors in immiscible composites need to be known. Many system-related characteristics such as hardness level, volume fraction and geometrical arrangement of the constituent phases can induce complex interacting deformation processes.

In order to study the deformation behavior and related supersaturation processes a systematic variation of the potential limiting parameters during high-pressure torsion is conducted on two different immiscible systems. Cu-Ag and Ag-Ni were chosen because they coincide concerning lattice structures and positive heat of mixing, but differ in their saturation hardness levels of the constituent phases.

In the Cu-Ag composites with initial phase dimension in the micrometer range the hardening behavior and microstructural evolution can be divided in three distinct stages. In the first stage in the beginning of the deformation process co-deformation of the individual phases takes place leading to a lamellar microstructure independent of composition and deformation temperature. In the second stage instead pronounced differences are observed. In composites with low and high Ag content in the second stage further co-deformation takes place, resulting in a single-phase supersaturated solid solution in the third stage, also referred to as saturation regime. In the medium composition range where the constituent phases are available in nearly equal volume fraction, the high number of phase boundaries restricts dislocation activity. As a consequence, pronounced shear band formation governs the refinement and hardening process in the second stage. Large strains are accommodated within shear bands accompanied by a strong refinement and supersaturation, while the lamellar matrix remains dual-phase and only partial supersaturation is achieved. The final composite is composed of Cu-rich, Ag-rich and single-phase supersaturated solid solution regions. To obtain a homogeneous single-phase supersaturated solid solution in the medium composition range lowering of the processing temperature to liquid nitrogen is necessary. At elevated temperatures decomposition is promoted due to thermodynamic driving forces and phase-separated composites evolve independent of composition. In general, a transition from complete single-phase supersaturated alloys at low deformation temperatures to fully phase-separated composites at elevated temperatures occurs. The temperature window for homogenous supersaturation depends on the volume fraction of phases.

In the Ag-Ni system the constituent phases have markedly different saturation hardness levels. The deformation behavior is therefore governed by strong strain localization in the softer Ag phase and elongation and repeated fracturing of the harder Ni particles. The effect of strain localization becomes more pronounced when the volume fraction of Ni is decreased. In a Ag-2.3wt%Ni composite the fragmentation of Ni is extremely delayed and retained Ni powder particles are still observed even at the highest applied strain level. Consequently, it takes high strains to reach the critical phase dimension required for dissolution and the supersaturation process is retarded as well.

In conclusion, a fundamental relation between the deformation mechanisms in the composites and the resulting degree of supersaturation exists, because inhomogeneous deformation modes can limit or delay the supersaturation process.

Contents

1 Introduction and aim of the thesis

The constantly increasing demands for high performance materials motivated extensive research on nanocrystalline materials in the last decades due to their exceptional mechanical properties. The fabrication of nanostructured materials can be realized by production methods such as rapid quenching, film deposition or severe plastic deformation (SPD). To make use of them in structural applications nanocrystalline materials in bulk form are requested, which is for example feasible with SPD techniques. In the last years strategies to reduce grain sizes down to the nanometer regime have been established, in which the introduction of second phases has shown promising results to reduce the grain size beyond the saturation state for single-phase materials [1]. In particular, composites of immiscible systems have increasingly gained attention in the material science community for manifold reasons. On the one hand, in these systems grain sizes of well below 50 nm can be reached, which leads to enormous Hall-Petch hardening. Great efforts to combine the enhanced mechanical properties with other functional features, for example in magnetic or electrical applications, are in progress [2–10]. Additionally, the thermal stability of nanocomposites with immiscible components is extraordinary high compared to single-phase nano-grained alloys or pure metals [11]. On the other hand, the occurrence of deformation-induced supersaturation and amorphization phenomena can lead to metastable phases with exceptional materials properties, as for example strength levels near the theoretical limit [12]. Moreover, they are used as model materials to study the basic deformation mechanisms in dual- or multi-phase materials during mechanical processing.

Deformation-induced mechanical mixing has been extensively investigated in ball-milled materials for several decades. Thereby a supersaturation of immiscible elements was documented in several studies, but the degree of mixing strongly varies for different material systems. Complete single-phase supersaturated solid solutions over the whole composition range were for example observed in the Cu-Ag [13] and in the Cu-Co system [14]. In the Cu-Fe system, a single-phase fcc solid solution was obtained up to Fe-contents of 60 at%, while the bcc solid solution was found to be stable up to 20 at% Cu [15]. In contrast, in the Ag-Fe system no solid solutions could be obtained [16]. Also in the Ni-Ag system, supersaturation was very limited, only 4.3 at% Ni could be dissolved in the Ag phase and 6.6 at% Ag in the Ni phase [17]. Moreover, amorphization was observed during ball milling of Cu-Cr [18] and Cu-W [19]. However, Yavari and Desré attributed the amorphization reaction to oxygen contamination during ball milling, which in fact represents a ternary system with a negative heat of mixing [20]. To avoid the problems that come along with the ball milling procedure, namely the undefined process parameters like applied strain, processing temperature and impurities, SPD techniques such as accumulative roll bonding (ARB) and high-pressure torsion (HPT) have been used to study the phenomenon of mechanical mixing in recent years. Similar results as in ball milling were observed in the aforementioned systems, for example in Cu-Ag and Cu-Fe supersaturated solid solutions could be obtained, while in Cu-W and Cu-Cr the degree of mixing was very limited. The observed variations in the degree of supersaturation depending on the material system were attributed by some authors to the different levels of the positive mixing enthalpy [16]. Others claimed that large differences in hardness of the constituent phases could lead to strain localization, which impedes the mixing process. A summary of the existing literature and ongoing debates concerning mixing processes and limiting factors for mechanical mixing can be found in paper IV.

The present study addresses the following open questions:

- What are the basic deformation mechanisms in these composites?
- What are the requirements and limits for deformation-induced supersaturation?
- Is there a correlation between the mechanical mixing process and the deformation behavior?

To answer these questions HPT processing on two selected material systems was performed. The Cu-Ag and Ni-Ag systems were chosen as model materials for various reasons. Both systems exhibit a positive enthalpy of mixing, which can be mainly attributed to the large lattice mismatch, and they do not possess intermetallic phases in the entire concentration range of the binary phase diagram. Ball milling studies on these systems revealed complete supersaturation in Cu-Ag, but very limited solubility in Ni-Ag. Moreover, they are ideal for comparative studies as the Cu-Ag system consists of two ductile phases and the Ni-Ag system exhibits strong hardness differences between the constituent phases.

The HPT process was chosen on account of several advantages compared to other SPD techniques. Since the material is deformed under high, nearly hydrostatic pressure and because the specimen dimensions remain unaltered, the process allows a crack-free deformation of numerous materials to very high strains. The initial material can be either bulk or powder, so that by blending and consolidation of elemental powders unlimited multiphase composite systems can be produced. Additionally, large chemical and structural inhomogeneities, which would arise from conventional casting in these systems, can be avoided. Therefore, the Cu-Ag and Ni-Ag composites were produced by blending elemental powders in the desired compositions and subsequent consolidation and deformation by HPT. Another significant reason for using HPT for this specific study is the possibility to adjust processing parameters such as applied strain, deformation temperature, strain rate and pressure accurately and in a wide range. Moreover, the process can be conducted in a monotonic or cyclic version. HPT deformation is therefore an ideal method to correlate microstructural changes with material properties and to study the mechanical mixing process systematically.

The quasi-constrained HPT setup used for this study is schematically displayed in Figure 1. A disk-shaped sample is placed between two anvils, which have cylindrical cavities in the center. After loading the anvils, which results in high, nearly hydrostatic pressures, they are rotated with respect to each other, thereby inducing a torsional strain. The applied shear strain γ can be calculated as:

$$\gamma = \frac{2\pi r}{t} n,$$

with the radius r, the thickness t of the sample and the number of rotations n. Technical details on the HPT process and the used setup can be found elsewhere [21].

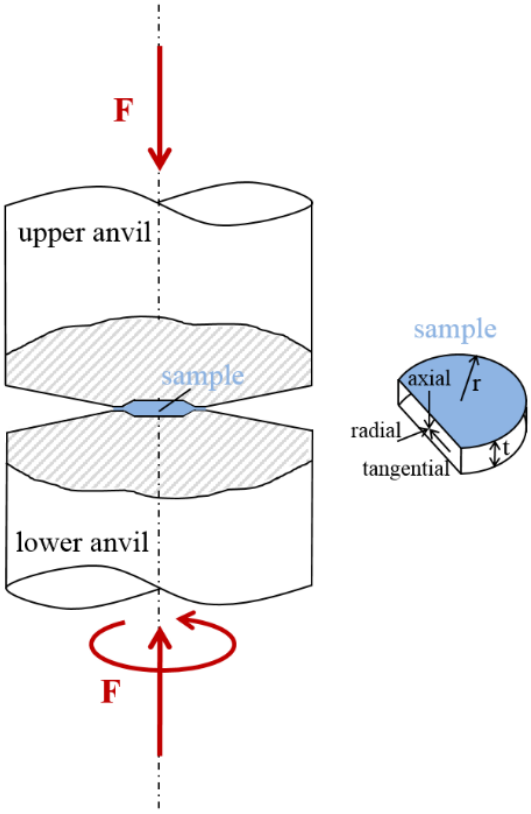

Figure 1: Schematic of the HPT process.

There are fundamental differences between the deformation of pure metals or single-phase alloys and the deformation of composites. The underlying mechanisms, which transform coarse-grained pure metals into an ultrafine-grained (UFG) state during SPD deformation, have been investigated intensively in the last two decades. The large number of accumulated dislocations are not randomly stored but arrange into new grain boundaries, and thereby subdivide the initial grains. The refinement process saturates at a certain strain level, which is usually about 20 for pure metals, then a so-called steady state or saturation regime is reached. A detailed overview on these processes can be found in [22]. In the saturation regime a dynamic equilibrium between grain refinement and restoration processes prevails and keeps microstructural features such as grain size, boundary length and boundary misorientation distribution on a constant level. In a detailed study on cold-rolled pure Cu by Renk et al. [23] grain boundary motion was identified as the dominant restoration mechanism. The saturation microstructure formed in pure metals is independent of the initial state of the material, as shown for example in Ni [24], and the saturation grain size and consequently the saturation hardness of pure metals in HPT depends mainly on the material, the deformation temperature, alloying elements and the amount of impurities [22,25].

In contrast, in composites more complex fragmentation processes usually take place. Only in the very beginning of the deformation process similar grain refinement processes as in pure metals are observable within the respective phases, as long as the phase dimensions are in the

micrometer range. Further refinement is governed by the characteristics of the composite like volume fraction and hardness levels of the constituent phases. A general observation in this context is that much higher strains than in pure metals are needed to reach a saturation, if a saturation is ever reached at all within reasonable amounts of applied strains. Moreover, contrary to pure metals or single-phase alloys, the initial arrangement of phases plays a key role, because geometrical changes of the phases dominate the subsequent microstructural evolution and deformation behavior. Finally, amorphization or supersaturation processes, which are in the focus of this study, can additionally influence the deformation process markedly. Overviews on the deformation processes in dual- or multi-phase materials can be found in [26] and paper IV.

2 Experimental results

2.1 The Cu-Ag system

Cu-Ag composites were produced by blending elemental powders in five compositions, Cu-10/25/50/75/90wt%Ag, and HPT processing for a maximum of 300 rotations at different deformation temperatures at a nominal pressure of 7.5 GPa. The samples are 8 mm in diameter and have a thickness between 0.45 and 0.55 mm. The following chapter is divided into three parts. First, the deformation process at room temperature (RT) and related hardness and microstructural changes will be described, with the main focus on the Cu-50wt%Ag composite. Then the supersaturation behavior depending on composition and processing temperature will be summarized. The last part will shortly outline the thermal stability and decomposition behavior of the Cu-50wt%Ag composite.

2.1.1 Microstructural evolution at room temperature

The microhardness as a function of applied strain is presented in Figure 2 exemplarily for the Cu-50wt%Ag composite, the hardness plots of Cu-10/25/75/90wt%Ag can be found in paper II. The hardness evolution can be divided in three distinct stages, labelled as A, B and C. In regime A the hardness increases slightly up to strains of γ~100. Between applied strains of γ~100 and 500 a strong hardness increase is observed, corresponding to regime B. Exceeding applied strains of γ~500 a constant hardness level is reached in regime C, referred to as saturation or steady-state regime. Such a hardness profile is characteristic for immiscible binary systems, and was also observed for the other compositions in the Cu-Ag system and for example in the Cu-Cr [27] and Cu-Co [28] systems. In the following the microstructural evolution for the different hardening regimes will be presented.

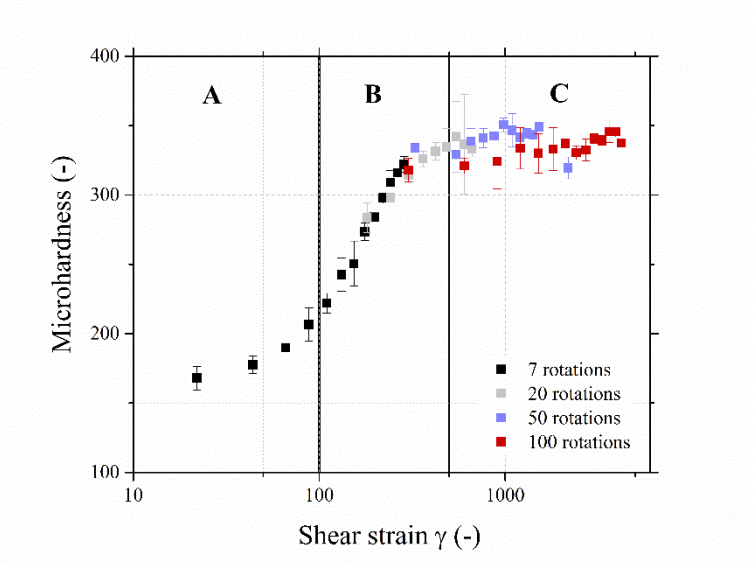

Figure 2: Vickers microhardness evolution with applied strain for the Cu-50wt%Ag composite. Measurements of four samples deformed for 7, 20, 50 and 100 rotations are included to cover a large applied strain range. Please note the logarithmic scale for the shear strain.

In Figure 3 the microstructural changes of the Cu-50wt%Ag composite in regime A are displayed. Figure 3a presents a backscatter-electron scanning electron microscopy (BSE-SEM) image of the initially spherical powder particles of the Cu-50wt%Ag powder blend. As shown in Figure 3b after compaction the particles are elongated in shear direction. The shear direction is parallel to the horizontal plane of the BSE-SEM images throughout the thesis. Ag and Cu regions appear in bright and dark contrast, respectively. In a more detailed image, Figure 3c, the original powder particles of Cu are still distinguishable due to the natural oxide layer on the particles, which is visible as a dark seam, as indicated with arrows in Figure 3c and d. Within the particles substructures were formed as shown for a Cu region in Figure 3d even before the shear deformation was applied. With ongoing deformation inside the individual Cu and Ag regions an UFG saturation grain structure was generated by similar mechanisms as in pure metals (for details on the fragmentation and saturation process see [22]). However, due to the natural oxide layer, it requires larger strains for the Cu phase to reach saturation than for the Ag phase, for details see paper II. With increasing strain the lamellar structure is continuously refined as the thickness changes of the Cu and Ag lamellae in Figure 3b, e and f imply.

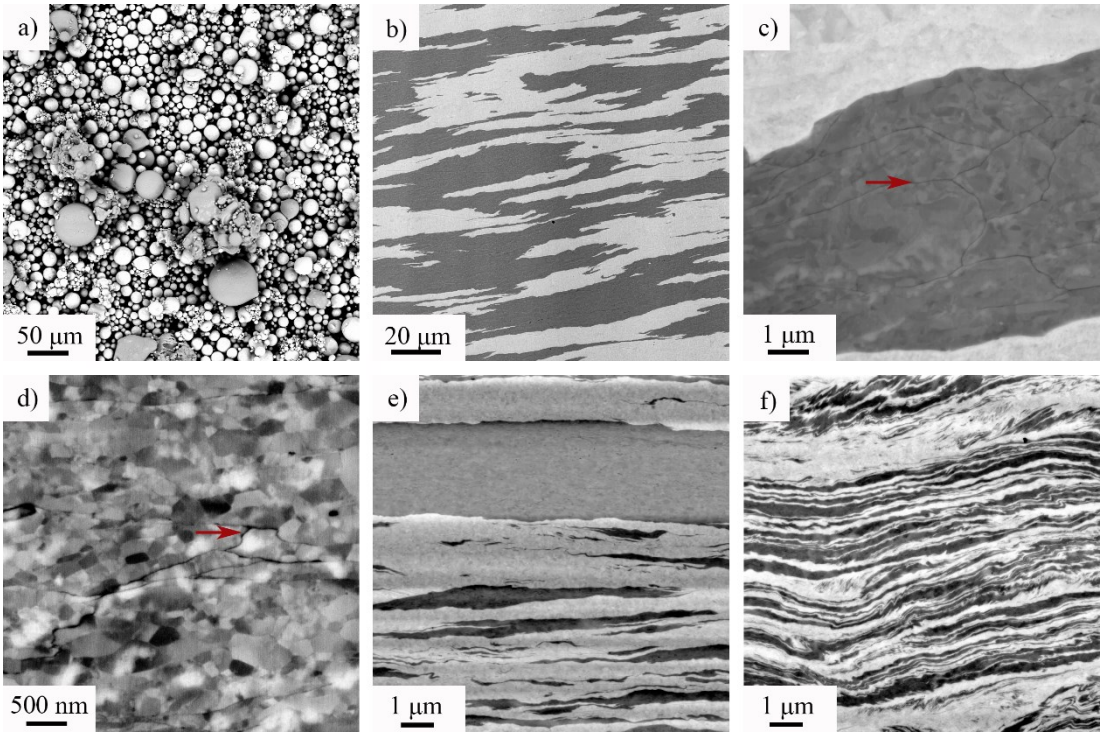

Figure 3: a) Image of the Cu-50wt%Ag powder blend. Micrographs in tangential direction for the Cu-50wt%Ag composite at different applied strain levels: b) and c) γ~0, d) detailed image of a Cu region showing an UFG structure, e) γ~25 and f) γ~125 revealing the refinement of the lamellar structure. All images are taken with BSE contrast.

The lamellar alignment and continuous thinning of the lamellae (corresponding to regime A in the hardness evolution) with the simultaneous formation of UFG structures inside the individual Cu and Ag phases was observed in the entire compositional range of investigated composites (see paper II). When the lamella thicknesses became comparable with the grain

size inside the lamellae, a further increase in hardness was observed, corresponding to the beginning of regime B.

In regime B distinct differences in the microstructural evolution and deformation behavior occurred depending on the composition. In composites with low and high Ag content (Cu-10/90wt%Ag), shown exemplarily for the Cu-10wt%Ag composite in Figure 4a and b, the Cu and Ag lamellae continued to refine uniformly in regime B. The minor phase was gradually dissolved in the matrix until in the saturation regime C a homogenous single-phase supersaturated nanocrystalline structure was formed, see Figure 4c. Transmission electron microscopy (TEM) bright-field (BF) and selected area diffraction (SAD) analyses for all compositions can be found in paper II. The supersaturation was also documented by Synchrotron X-ray diffraction (XRD) analyses, these results will be shown in the next section.

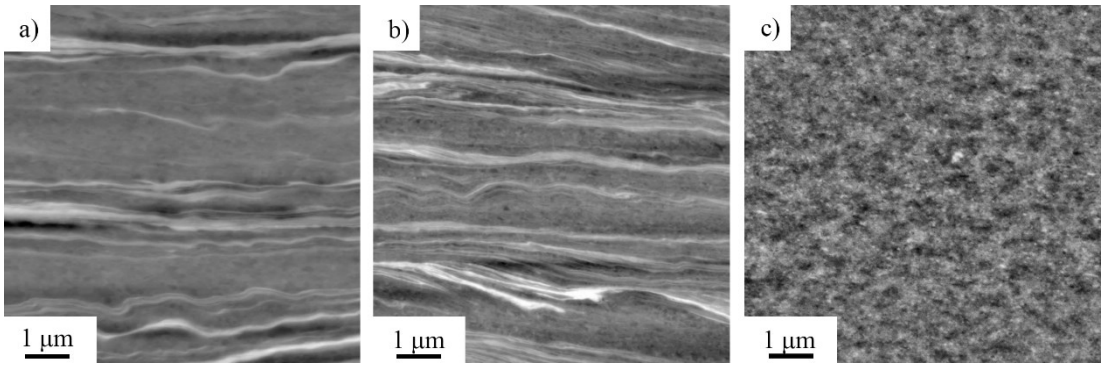

Figure 4: Microstructural evolution of the Cu-10wt%Ag composite imaged by BSE-SEM at applied strains of a) γ~190, b) γ~380 showing a continuous thinning of the minor phase and c) γ~1900 revealing a homogeneous nanocrystalline microstructure.

In contrast, the Cu-50wt%Ag composite deformed homogeneously up to applied strains of γ~190, before at higher strain levels shear band formation set in as seen in Figure 5a. With increasing strain new shear bands were continuously formed, see Figure 5b, and the lamellae were rotated with respect to the HPT shear plane. Further increase in strain led to a strong microstructural refinement, but no complete homogenization of the sample was achieved even at high applied strains of γ~1900, Figure 5c. TEM investigations showed that at a strain of γ~190 the lamella thickness has decreased from initially several micrometer to below 10 nm in some regions, Figure 5d. In these fine-lamellar regions shear banding is promoted, see Figure 5a and e. The shear bands have thicknesses between 100 and 300 nm, and inside the shear bands a nanocrystalline nearly equi-axed microstructure evolved. With the steady formation of new shear bands, a large volume fraction of the sample was transformed into this nanocrystalline structure, see Figure 5f. In addition the lamellar matrix is refined as well, compare the well-defined lamellae in Figure 5d with the lamellar structure with diffuse boundaries in Figure 5f or Figure 6a.

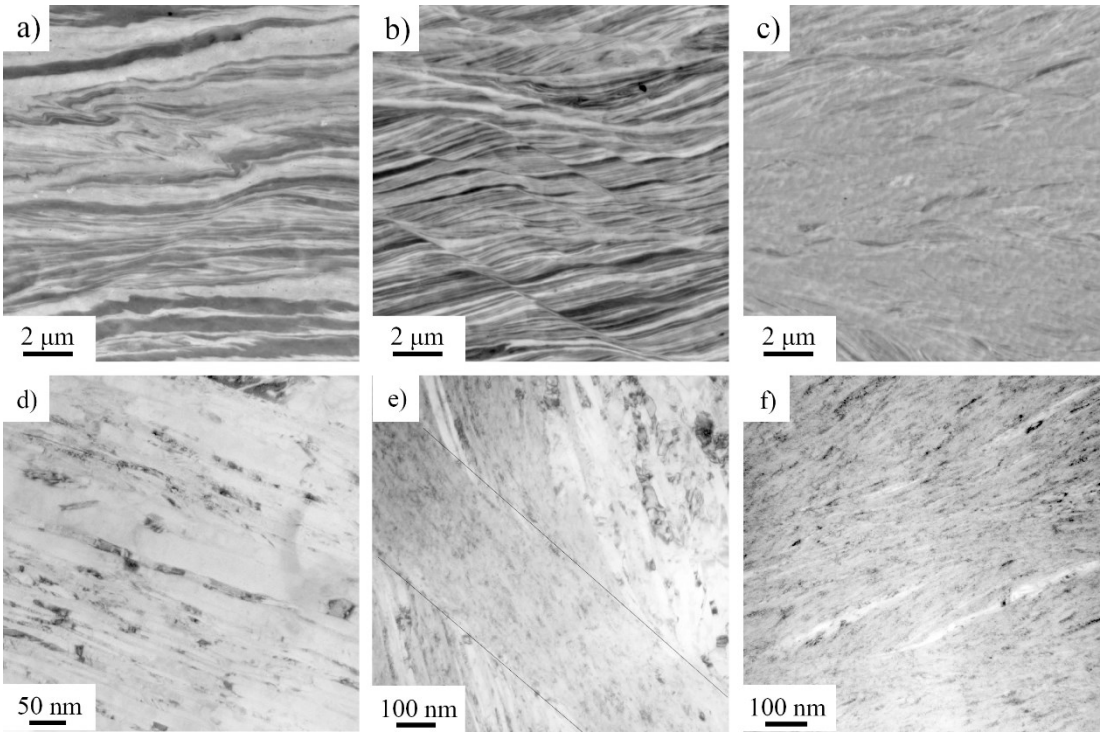

Figure 5: BSE-SEM microsgraphs in radial direction for the Cu-50wt%Ag composite at different applied strains. a) At γ~190 the first shear bands occurred. b) At γ~380 numerous shear bands were observed causing a lamella rotation. c) At γ~1900 inhomogeneities in the microstructure were still present. Corresponding TEM BF micrographs at the same strain levels d) γ~190, e) γ~380 and f) γ~1900.

Nevertheless, lamellar regions are retained even at an applied strain of γ~3800 as shown in the upper part of the TEM micrograph in Figure 6a. SAD analyses of the shear band in the lower part of the image in Figure 6a and the lamellar regions are shown in Figure 6b (the areas contributing to the SAD patterns are indicated by circles in Figure 6a). Azimuthal integrations obtained with PASAD analysis [29] revealed that a single fcc ring pattern is present in the shear bands, with positions of the diffraction rings in between the ones of pure Cu and Ag. Thus within the shear bands a supersaturated solid solution was formed, while the lamellar regions remained dual-phase (see the integration profiles in Figure 6c). In both regions a similar shear texture was observed apparent from the non-uniform intensities of the diffraction rings.

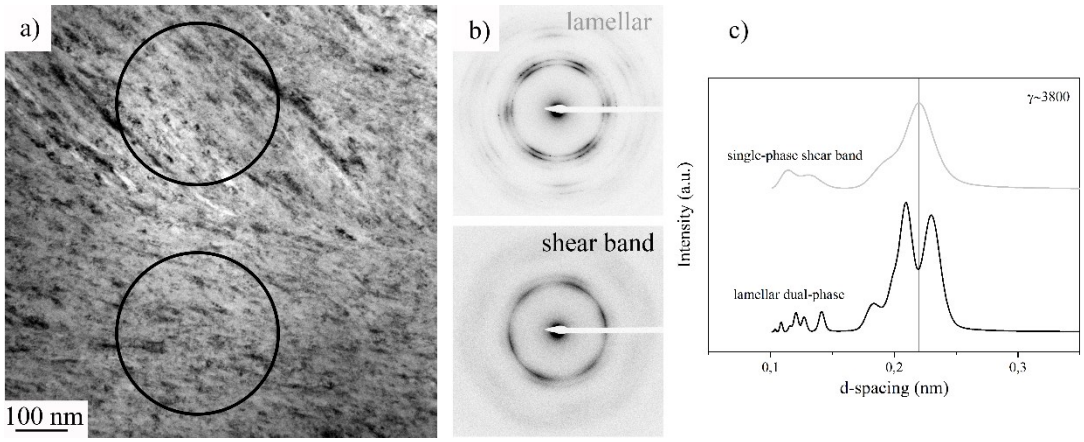

Figure 6: a) TEM BF image of the Cu-50wt%Ag composite at an applied strain of γ~3800 showing a region containing a shear band in the lower part of the image and a retained lamellar region in the upper part. b) Corresponding SAD patterns for the shear band and lamellar region with c) azimuthal integration revealing the single-phase supersatured solid solution generated in the shear band and the dual-phase state of the retained lamellar region.

For a detailed analysis of the deformation behavior, in particular the shear banding process, split sample experiments were conducted. Markers were cut by FIB into the polished radial cross-sections of samples deformed to different applied strain. Subsequently, the samples were put together with a matching counterpart into the HPT and further deformed with a comparably small strain increment. The FIB cuts were imaged by SEM before and after the additional deformation step, for further information on experimental details see paper III. In Figure 7 two experiments are shown performed on samples pre-deformed to strains of γ~250 and γ~1250, corresponding to regime B and C, respectively. The results revealed that in the hardness regime B the deformation is realized by a combination of uniform shear, see the distortion of the FIB grid in Figure 7a, and local shear band formation, Figure 7b. Instead in the saturation regime C the FIB grid was displaced at three positions by several shear bands, while the material between these shear bands remained undeformed, apparent from the vertical orientation of the FIB lines, see Figure 7c and detail in Figure 7d. Thus, in hardness regime C most of the imposed strain is carried by a few shear bands hindering further refinement of retained lamellar regions.

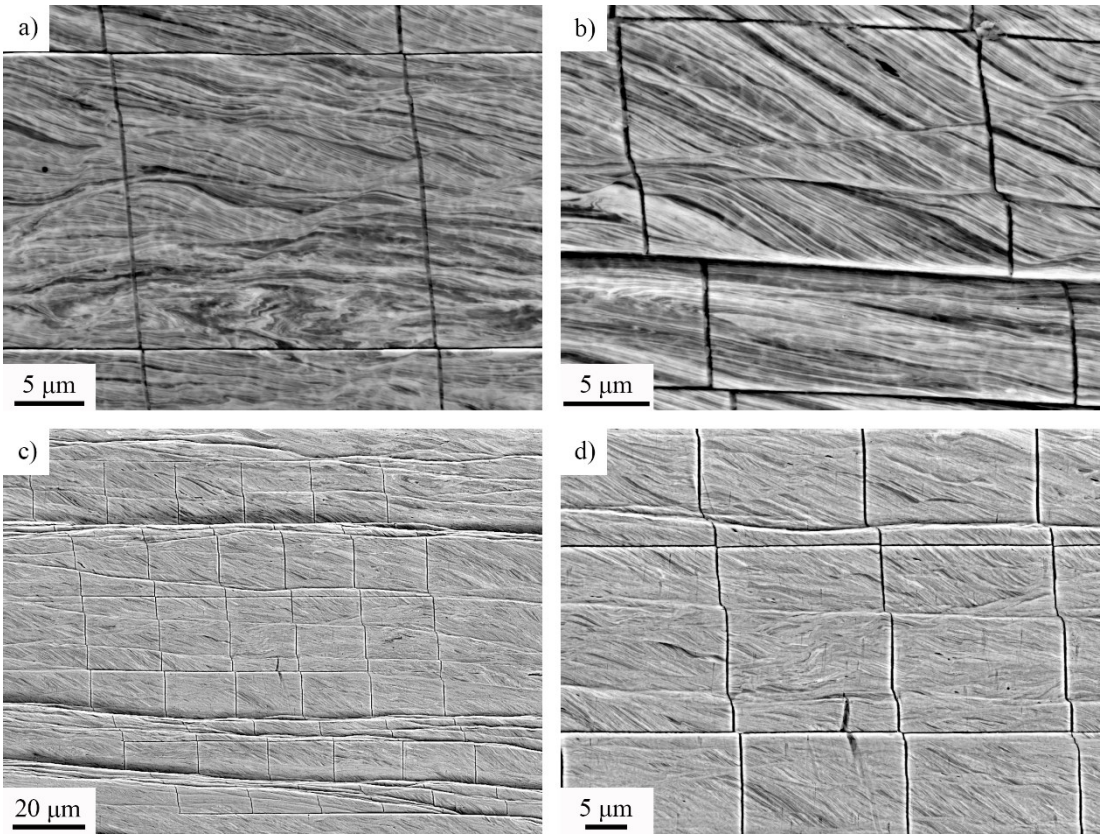

Figure 7: Split sample experiment for the Cu-50wt%Ag composite for a) and b) a sample pre-deformed to γ~250 plus an additional strain of 0.35 revealing that the deformation is realized by a combination of uniform shearing and shear band formation. c) A sample pre-deformed to a total applied strain of γ~1250 plus an additional strain of 1 showing that the deformation is mainly carried by shear bands.

To probe the local mechanical properties of the deformed samples nanoindentation measurements were performed. The sample was processed for 300 rotations, corresponding to an applied strain of γ~11300 at a sample radius of 3 mm. This sample was chosen because it exhibited large single-phase regions generated by shear bands and contained also lamellar regions. Figure 8a shows one of the load-indentation curves measured in a strain-rate jump test, for experimental details see [30]. The corresponding hardness data is displayed in the inset. The calculated mean value of several measurements revealed only a minimal difference in hardness for the two different microstructural states, see paper III. A detail of the load-indentation depth curve is additionally shown for the two tested regions. In single-phase regions, Figure 8b the occurrence of a jerky flow behavior was observed, indicating a different deformation behavior than in lamellar regions, Figure 8b, which exhibited a smooth continuous curve. Such pop-ins are typically observed for example in amorphous materials like bulk metallic glasses [31,32]. Also the difference in strain rate sensitivity is not pronounced.

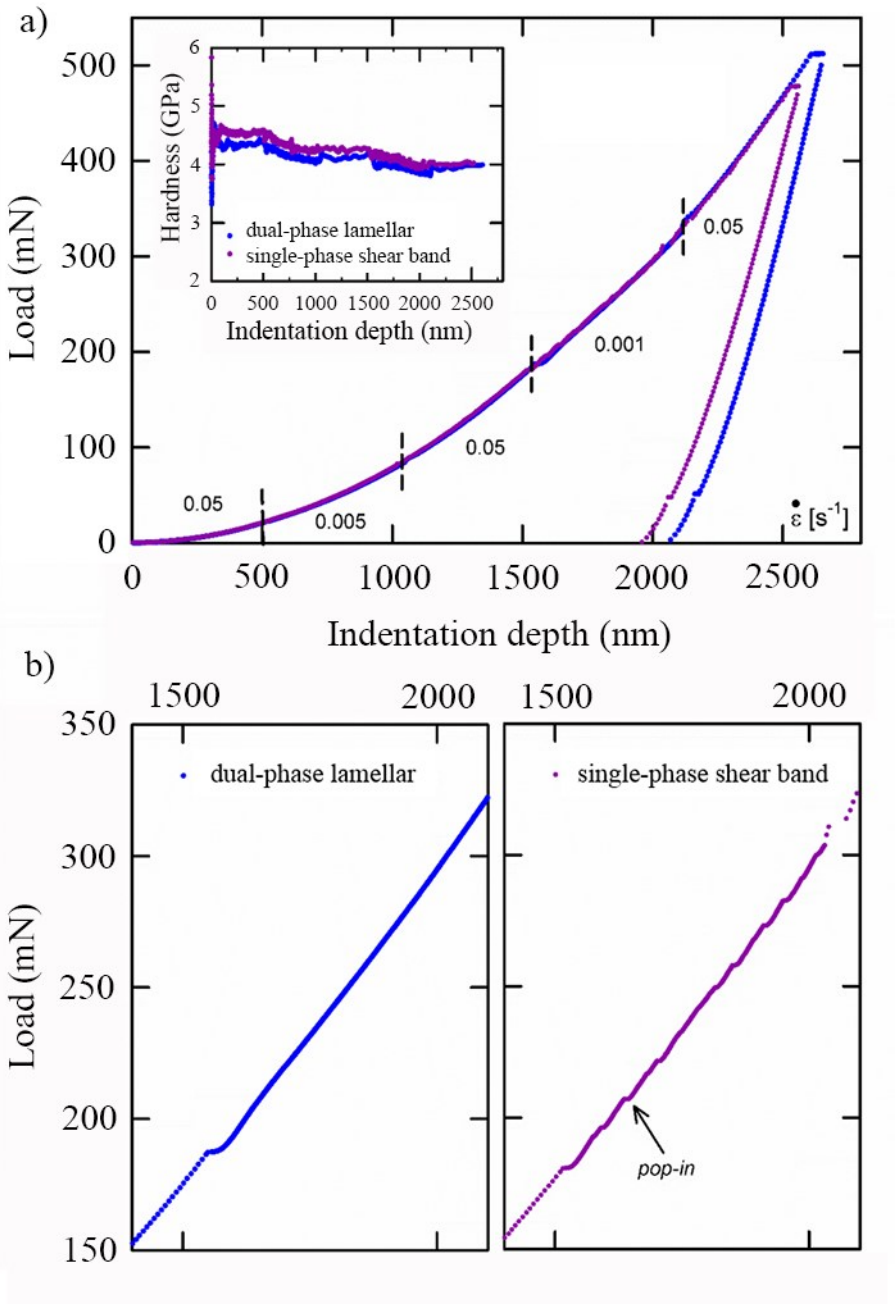

Figure 8: Nanoindentation measurements at RT for dual-phase lamellar and single-phase shear band regions. a) Load-indentation depth curve for the two tested regions with the hardness data in the inset. b) Details of the load-indentation depth curve for the lamellar and single-phase regions.

As revealed by TEM the grain size within the shear bands is similar at low and high applied strains, see Figures 5e and 6a and paper III. Therefore, it is plausible to assume that the hardness in these microstructural regions and there the flow stress during deformation is similar irrespective of the applied strain. This consideration suggests that at low applied strains (regime

B) a hardening in the shear bands occurs to a certain level and simultaneously new shear bands form. The lamellar regions further refine until their hardness approaches the hardness level of the shear band regions. Increasing the strain towards regime C the number of actively operating shear bands reduces and deformation is finally carried by a limited number of shear bands. Therefore no homogenization of the microstructure is obtained even at the highest applied strain. It should be noted that the deformation behavior during deformation is argued on the basis of hardness measurements. A detailed study on the formation and propagation of shear bands can be found in paper III.

In few HPT samples very thin (~200 nm) line features were observed, which had a slightly brighter contrast indicating a higher Ag content. One example is shown in Figure 9a on a HPT sample deformed to an applied shear strain of γ~1250, as indicated by an arrow. A FIB grid (without intermediate horizontal lines) was placed across the observed line feature. After an additional applied shear, see Figure 9b, this thin layer was clearly identified as a shear band. The upper part of the FIB marker was displaced for about 50 µm. Compared with the shear bands shown in Figure 7b and c this is a remarkable amount of shear for one single band. It was calculated that almost one third of the total applied deformation was accommodated by this single 200 nm shear band. A top view on this shear band shows that indeed the parts below and above are completely sheared off against each other and uncover a new surface (see Figure 9c, the imaged area and view direction is marked in Figure 9b).

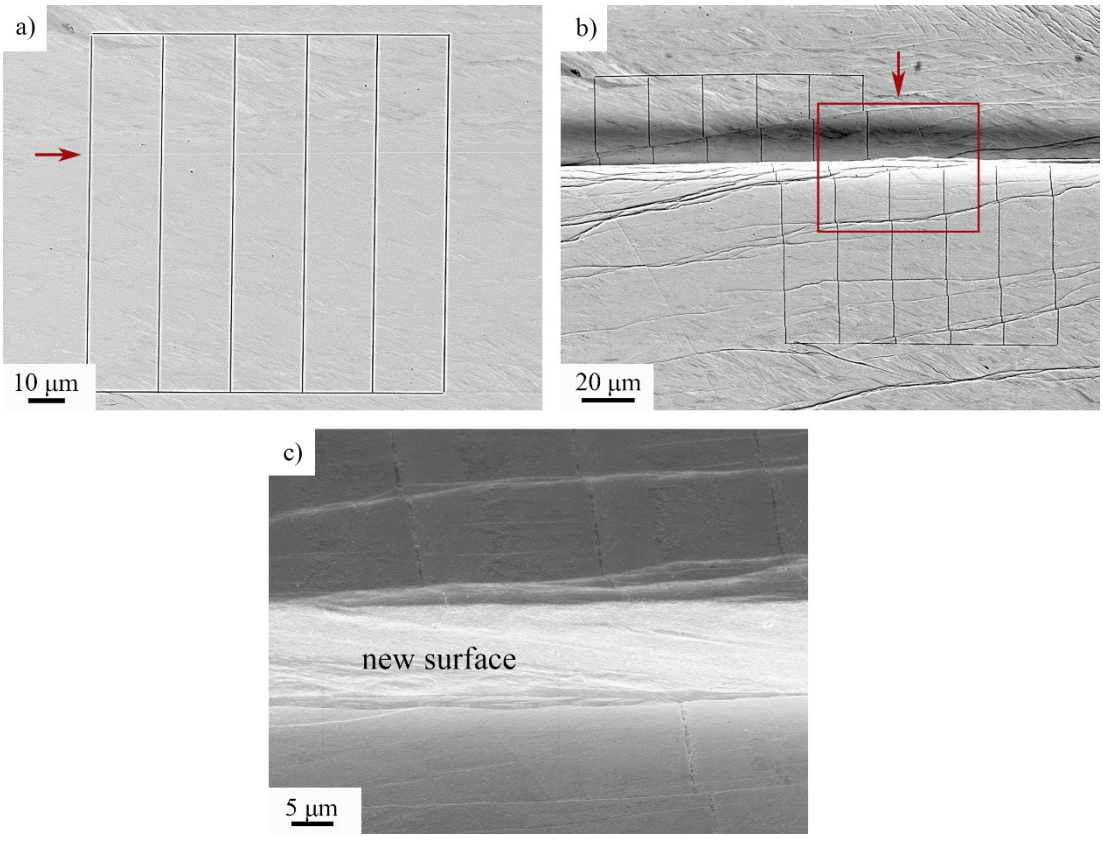

Figure 9: Split sample experiment for the Cu-50wt%Ag composite defomed at RT to an applied strain of γ~1250. a) Original FIB grid and b) FIB grid after applying an additional shear strain of γ~0.35. c) Top view on the split sample revealing the newly formed surface by the localized shear deformation.

The underlying deformation mechanism is assumed to be the same as in the commonly observed shear bands commencing in regime B. A precursor for such dominant shear bands could be the shear band bundles as shown in Figure 7c, which finally emerge into one single band. If such a shear band is developed, it can accommodate the entire applied shear strain, which means two parts of the HPT disk are simply sheared against each other without any deformation taking place in the rest of the sample. This hinders any further refinement of the microstructure. It is unclear which conditions lead to such dominant shear bands. Explanations could be the imperfect alignment of the anvils or an unfavorable initial arrangement of powder particles. Due to sample geometry and the imposed strain path this special shear band must be aligned almost perfectly parallel to the sample surface, only the position over the sample thickness can vary.

To summarize, HPT processing of Cu-Ag composites at RT leads to lamellar structures at low applied strains independent of composition. In the individual Cu and Ag phases UFG structures formed. With increasing strain in the Cu-10 and 90wt%Ag composites the respective minor phase becomes continuously thinned until it completely dissolves and a nanocrystalline, single-phase supersaturated solid solution forms. In the Cu-50wt%Ag composite the phases have similar volume fractions and after alignment to a lamellar structure a uniform thinning of the lamellae occurs until the formation of shear bands sets in. This localized deformation hinders homogenization of the composite and the final obtained microstructure is composed of the retained nano-lamellar matrix and nanocrystalline supersaturated regions generated by shear bands.

2.1.2 Influence of composition and processing temperature on supersaturation

To study the degree of supersaturation systematically HPT deformation at varying temperatures and to different applied strains was conducted for the Cu-10/50/90wt%Ag composites. The amount of dissolution was evaluated by lattice parameter changes recorded in synchrotron XRD measurements.

Figure 10 displays XRD patterns of the Cu-10wt%Ag composite at different strain levels and at the highest strain level deformed at RT, 100 °C, 200 °C and 300 °C. The profiles are plotted as a function of the d-spacing and the (111) Ag and Cu peaks are marked with lines. A comparison of the patterns for strains between γ~190 and 760 demonstrates that the Ag peaks diminished with increasing strain. Simultaneously, a clear peak shift of the Cu peaks induced by lattice parameter changes occurred, which indicates the dissolution of the Ag phase. The solute concentration calculated by using Vegard´s law gives a Ag concentration of below 1 at% at a strain of γ~190. The amount of Ag dissolved in the Cu phase increased to 1.2 at% Ag in the Cu phase at γ~380. When a strain of γ~760 was reached a single-phase alloy was obtained with the global composition of 8 at%. Between the XRD profiles recorded at γ~760 and 1900 no significant difference was observed, thus saturation was already reached at γ~760. At elevated deformation temperatures a change from a single-phase solid solution to a dual-phase composite with a transition between 100 and 300 °C occurred. At 200°C a partial supersaturation of 4 at% Ag in Cu was observed.

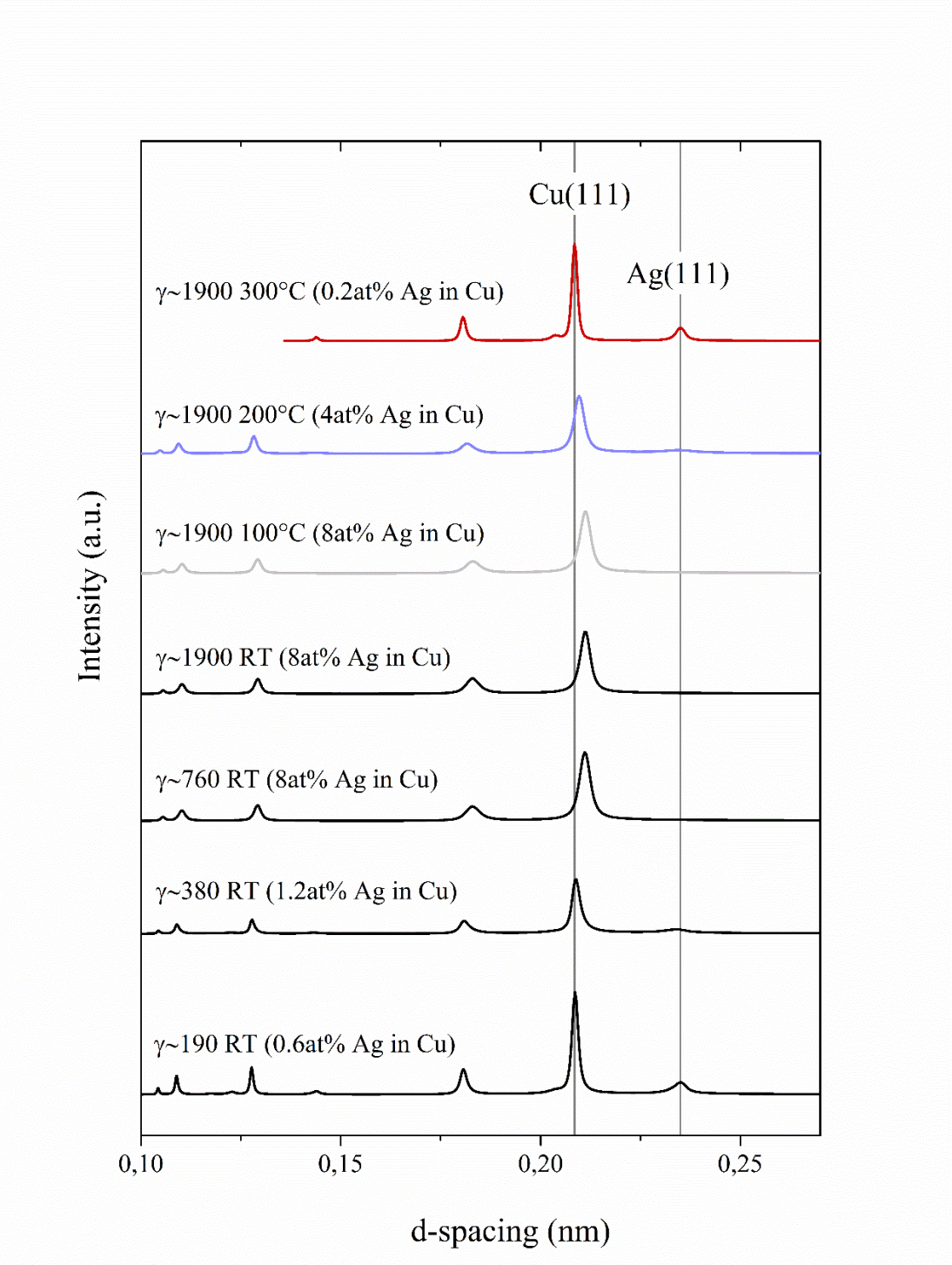

Figure 10: Synchrotron XRD patterns of the Cu-10wt%Ag composite deformed at RT for different strain levels and deformed at 100, 200 and 300 °C to the highest strain level. (Taken from paper V.)

The XRD patterns recorded for the RT-processed Cu-50wt%Ag composite at different strain levels are highlighted in Figure 11. The pronounced peak broadening with increasing strain indicates the severe grain refinement, which was also documented with SEM and TEM. At low strains only peaks from Cu and Ag are present, the supersaturated phase, which was generated in the shear bands, appeared at applied strains of γ~1900. In accordance with TEM investigations, the Cu and Ag phases retain even at the highest applied strain level. Evaluation of the peak shifts (compare the positions of the (111) Cu and Ag peaks at γ~190 and 1900) revealed that also in the lamellar regions partial supersaturation occurred, the amount of dissolution was determined to be about 8 at% Cu dissolved in the Ag phase and 2 at% Ag in the Cu phase.

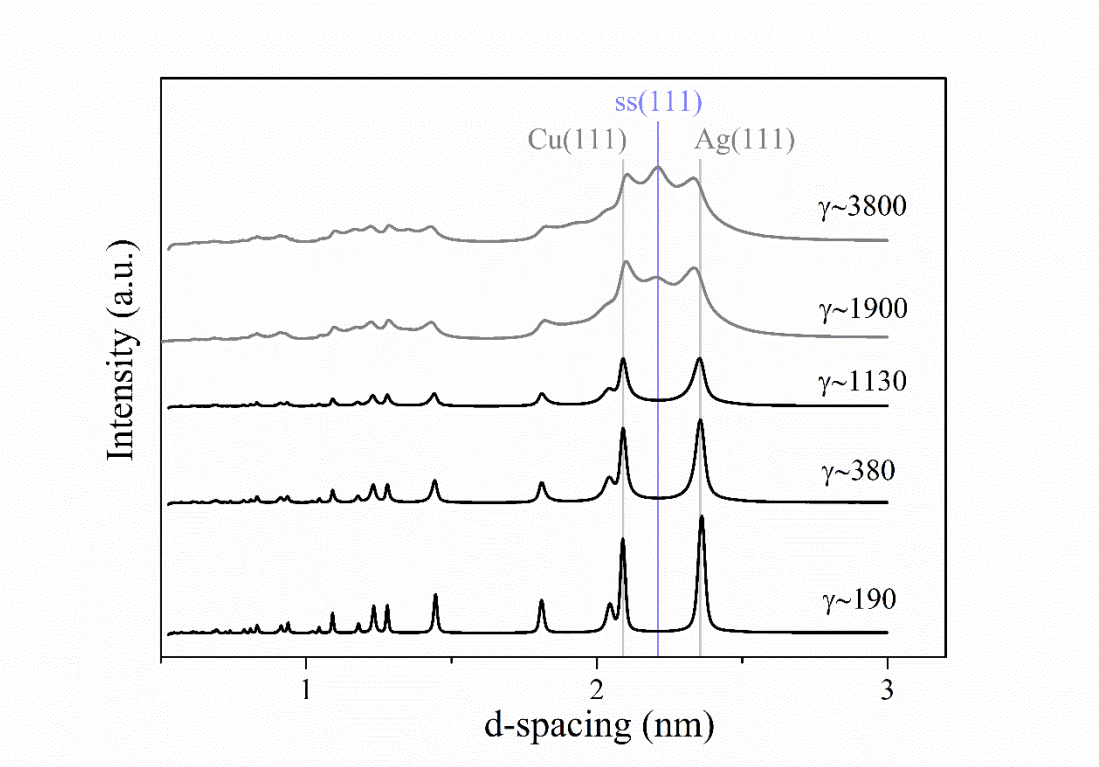

Figure 11: Synchrotron XRD patterns for the RT-processed Cu-50wt%Ag composite subjected to different strain levels. (Taken from paper V.)

A comparison of the XRD profiles of the Cu-50wt%Ag composite deformed to an applied strain of γ~1900 at processing temperatures of LN, RT and 200 °C is presented in Figure 12. At 200 °C a complete phase-separated composite evolved as apparent from the distinct Cu and Ag peaks. In contrast at LN only the supersaturated phase was observed, thus a single-phase alloy was formed. From the direct comparison of the different processing temperatures it becomes evident that a transition from complete supersaturation at low processing temperatures to complete phase separation at elevated temperatures occurred, with an intermediate mixed state in between.

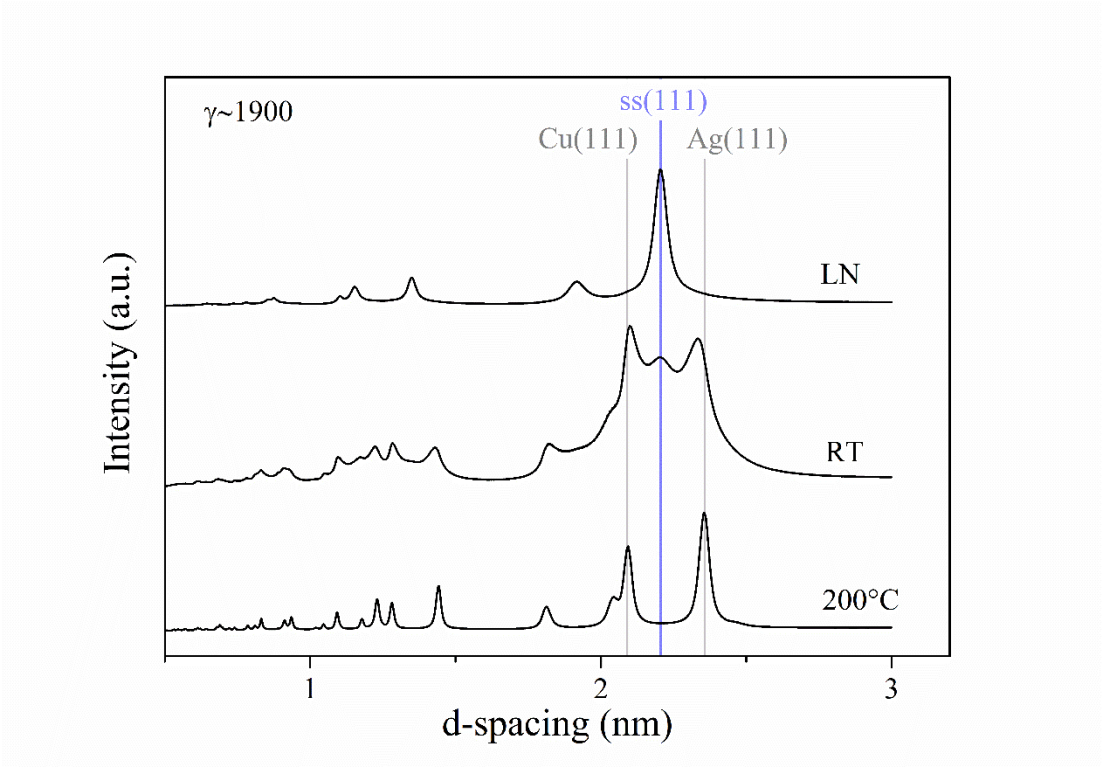

Figure 12: Synchrotron XRD patterns for the Cu-50wt%Ag composite processed to an applied strains of γ~1900 at LN, RT and 200 °C. (Taken from paper V.)

The microstructures of the Cu-50wt%Ag composite obtained at γ~1900 for different processing temperatures were also studied by TEM. As shown in Figure 13 in the saturation regime a homogeneous nanocrystalline microstructure was formed at LN temperature. The grains are slightly elongated and vary between 10 and 30 nm, as estimated from dark-field images. In the 200 °C and 300 °C processed Cu-50wt%Ag composites the grain size increased markedly to about 50 and 100 nm, respectively. SAD analyses confirmed the XRD results, that at LN a single-phase supersaturated solid solution was formed, while at 200°C and 300 °C a full decomposition into a dual-phase microstructure evolved.

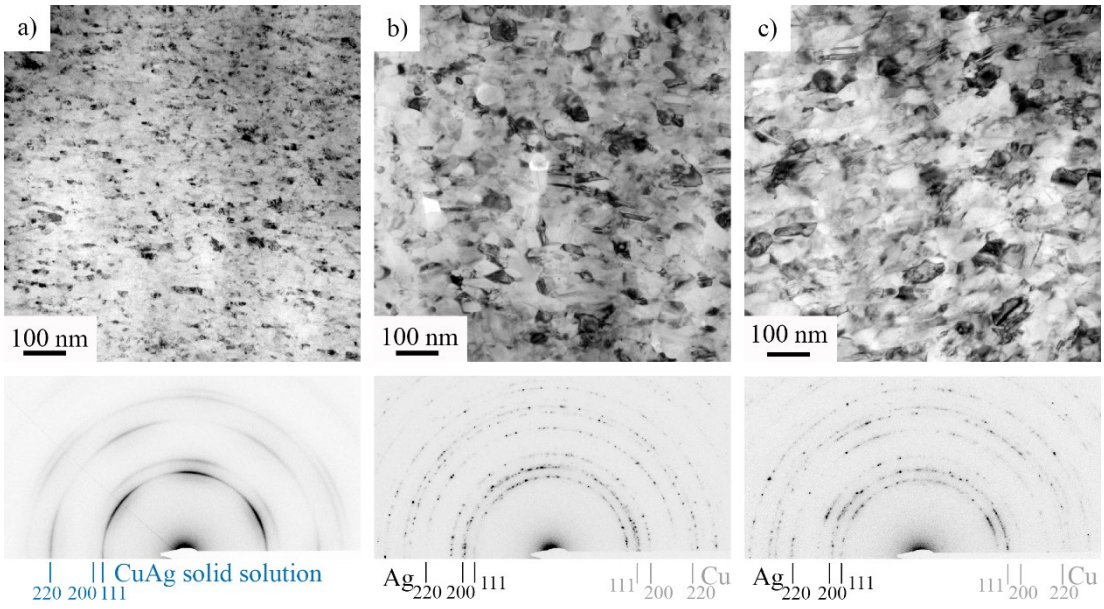

Figure 13: TEM BF images with corresponding indexed SAD patterns for the Cu-50wt%Ag composite deformed to an applied strain of γ~1900 at a) LN temperature, b) 200 °C and c) 300 °C.

The deformation processes leading to this saturation structures were studied by SEM. In Figure 14 a, b and c the microstructures of the Cu-50wt%Ag composite deformed to an applied strain of γ~380 are compared for processing at RT, LN and 200 °C, respectively. At RT the shear bands were distributed regularly. Thereby they caused a lamella rotation out of the HPT shear plane (compare with the parallel lamella alignment in Figure 5a). At LN also extensive shear band formation was observed but not as regular as in RT deformation. At a deformation temperature of 200°C a uniform lamellar structure inclined about 11° to the HPT shear plane was formed without any shear bands. To identify the differences between shear banding at RT and LN, which led to inhomogeneous microstructures at RT but single-phase supersaturated solid solutions at LN, additional experiments at RT and LN to higher strains, Figure 14d and e, and a combination of RT-deformation followed by LN-processing was performed. By comparing Figure 14d with 14e it becomes apparent that at LN a much stronger refinement took place towards a homogenous microstructure. In contrast, at RT no distinct further refinement was observed. A change in processing temperature from RT to LN, as shown in Figure 14f for a sample processed for γ~380 at RT and then for γ~190 at LN, led to stronger refinement compared to only RT deformation to the same strain. As mentioned earlier it was derived from nanoindentation experiments that pronounced hardening in the shear bands occurred. To explain the difference between shear band formation at RT and LN leading only at LN to complete single-phase microstructures, it is concluded that the difference in the hardness levels of the shear bands and lamellar regions is apparently higher at LN temperature. Therefore the lamellar matrix was progressively deformed by shear bands until a homogeneous single-phase alloy was obtained.

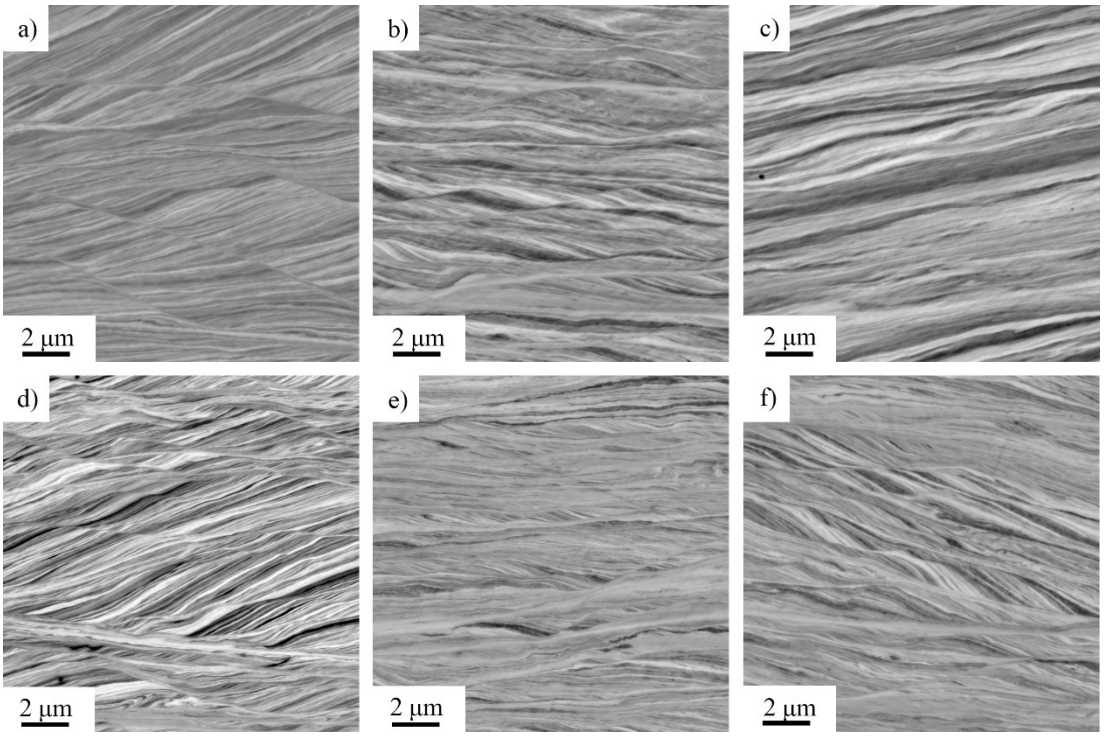

Figure 14: BSE-SEM micrographs in radial direction for the Cu-50wt%Ag composite. At an applied strain of γ~380 processed at a) RT showing regularly distributed shear bands causing a lamella rotation, b) LN temperature showing shear bands and c) at 200°C revealing a lamellar structure inclined to the shear plane without shear bands. At an applied strain of γ~570 processed d) at RT showing no distinct differences to γ~380 in a), e) at LN temperature revealing a strong and more homogenous refinement of the sample and f) processed at RT for γ~380 and additionally for γ~190 at LN temperature revealing a stronger refinement after the LN processing compared to only RT deformation.

In summary, in the Cu-10 and 90wt%Ag composites full supersaturation was achieved at RT. In the Cu-50wt%Ag composite a lowering of the processing temperature to LN was necessary to obtain a homogenous single-phase supersaturated alloy in this composition as well. In contrast, an increase in processing temperature to 200°C for the Cu-50wt%Ag and 300 °C for the Cu-10 and 90wt%Ag composites led to complete phase-separated composites. The recovery mechanisms maintaining the saturation microstructures in the single-phase alloys are presumably similar as in pure metals or conventional single-phase alloys. At elevated temperatures the underlying mechanisms are not clear, one possible process could be a balance between dissolution of shrinking grains and diffusion of solute atoms towards phase boundaries, for details see paper V.

2.1.3 Remarks on thermal stability and decomposition behavior

Due to the positive heat of mixing, it can be expected that decomposition of the supersaturated phase takes place upon annealing. A TEM *in-situ* heating experiment was conducted on a Cu-50wt%Ag sample deformed for 300 rotations, corresponding to an applied strain of γ~11300 at a radius of 3 mm. TEM BF micrographs and SAD patterns were recorded during stepwise heating up to 280 °C at different annealing temperatures. A single-phase supersaturated region was chosen for the experiment, the microstructures in the initial state and

at three annealing steps with corresponding SAD patterns are shown in Figure 15a to d. In Figure 16 the azimuthal integration profiles of the SAD patterns for annealing temperatures between 130 and 280 °C are additionally shown. The SAD pattern revealed the single-phase state of the investigated region, see Figure 15a and integration profile in Figure 16. As seen on the occurrence of a small shoulder in the integration profile originating from the diffraction peak of the Ag phase, indicated by an arrow in Figure 16, decomposition already started at 130 °C. Heating up to 175 °C resulted only in some minor modifications of the microstructure, as seen on contrast changes mainly in the thicker part of the sample (upper part of the TEM image). However, the decomposition process proceeded as seen in the integration profile, Figure 16, and on the inner diffraction ring in the SAD pattern corresponding to the (111) Ag which became apparent as indicated by an arrow in Figure 15b. At 210 °C a distinct (111) Ag peak was observed, see Figure 16, however in TEM BF micrographs no significant changes are seen. At 250 °C first grain growth was observed, which was also reflected by distinct spots in the SAD pattern, see Figure 15d. Phase decomposition completed at 280 °C as demonstrated by separate Cu and Ag diffraction rings, see integration profile in Figure 16.

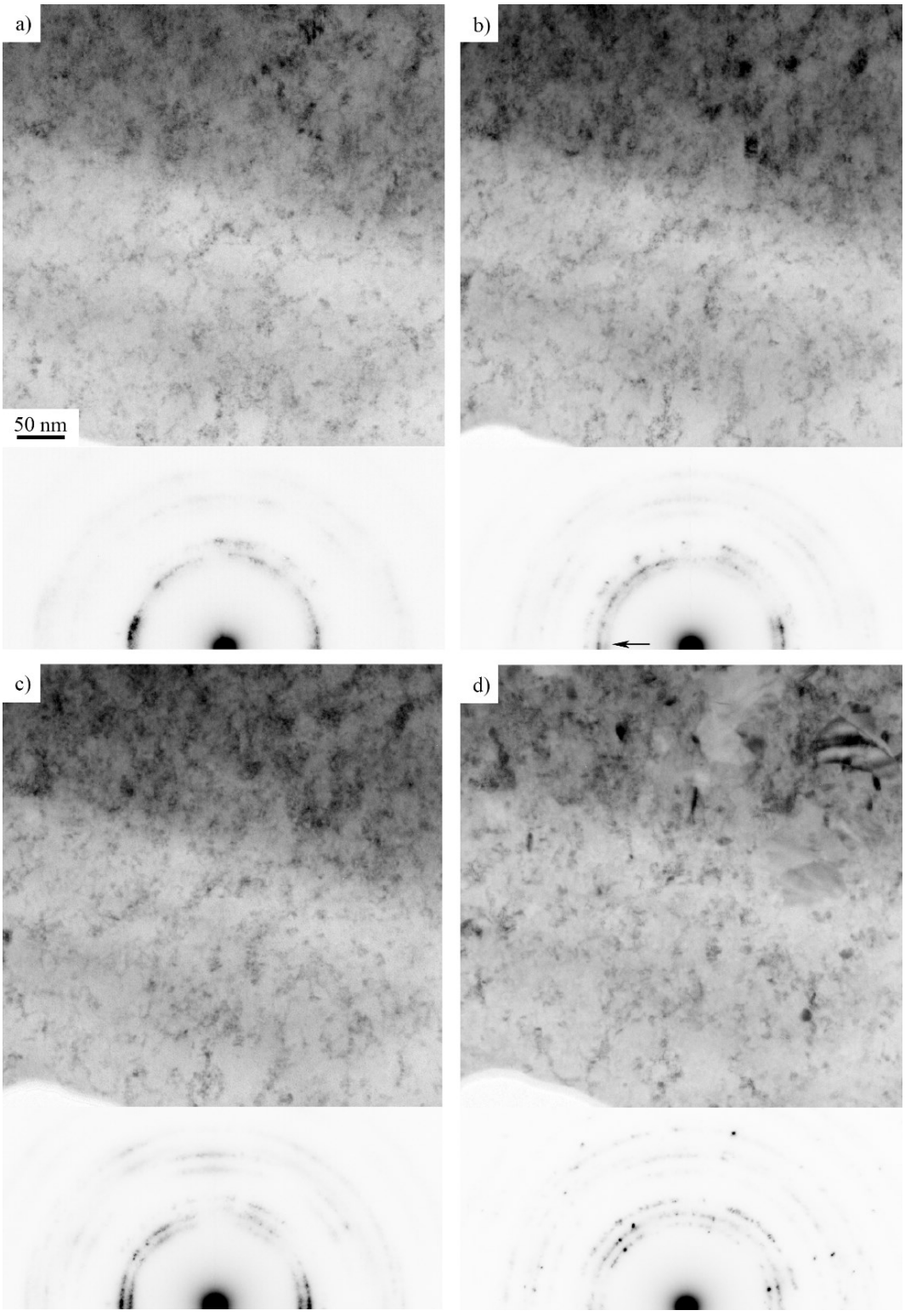

Figure 15: TEM BF micrographs and corresponding SAD patterns recorded in axial view during an *in-situ* heating experiment in the TEM, images recorded at a) RT, b) 175 °C, c) 210 °C and d) 250 °C.

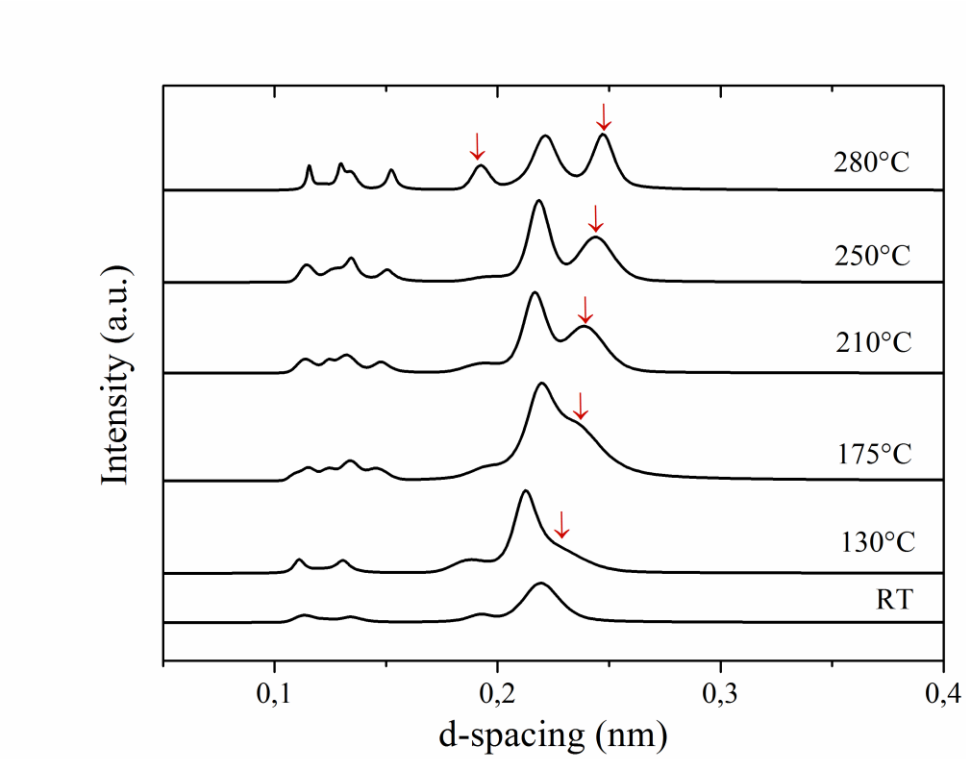

Figure 16: Integration profiles obtained from the SAD patterns recorded during the *in-situ* heating experiment for the different annealing temperatures. The relative shift between the different temperatures is affected by the experimental setup demanding a change between scanning TEM (STEM) and diffraction mode. Therefore the absolute positions of the peaks exhibit a slight shift.

Additionally, post-annealing for 2 h at 200 °C was conducted for the Cu-50wt%Ag sample deformed to 50 rotations, γ~1900 at a radius of 3 mm. The obtained results correspond to the findings of the *in-situ* heating experiment. Only minor grain growth was observed for single-phase and lamellar regions, as shown in Figure 17 a and b, respectively. SAD analysis revealed complete phase separation in both regions.

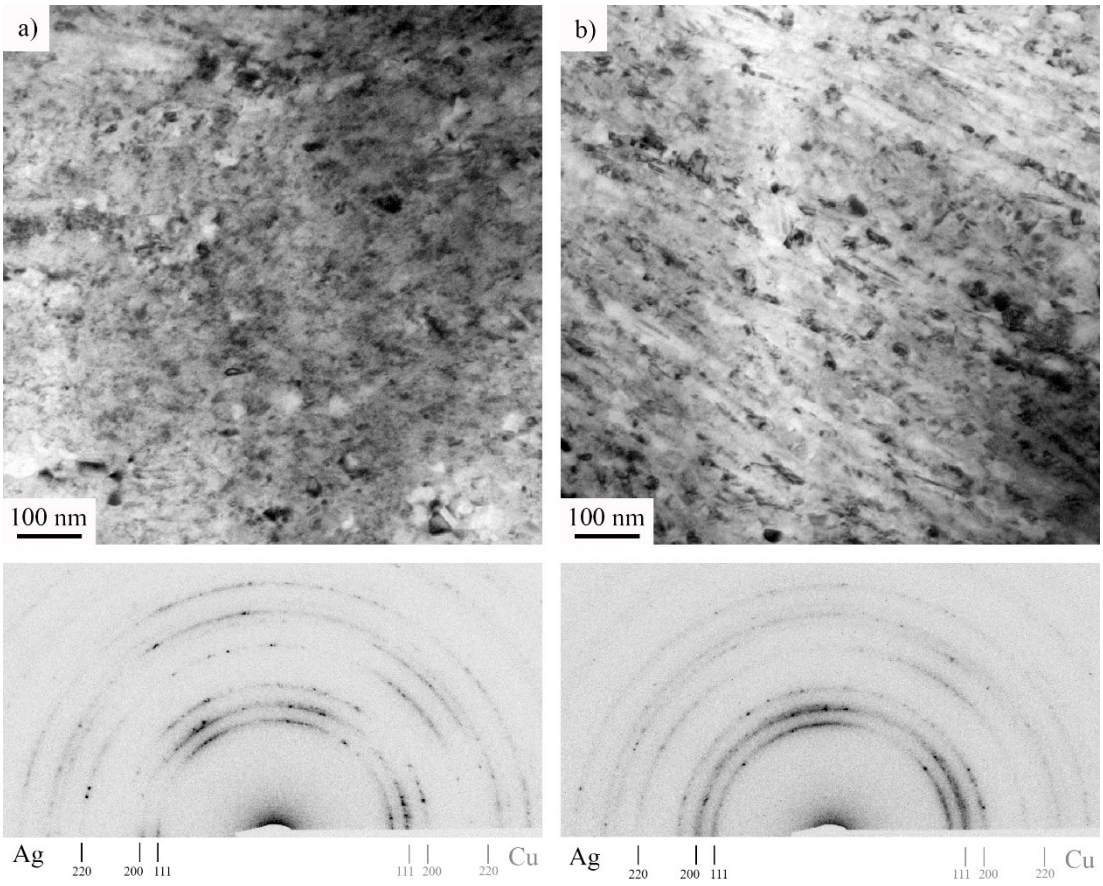

Figure 17: TEM BF images of a Cu-50wt%Ag sample post-annealed for 2h at 200 °C. a) Former single-phase region and b) lamellar region with corresponding SAD patterns.

2.2 Comparison with the Ag-Ni system

The Ag-Ni system differs from the Cu-Ag system mainly regarding the hardness levels of the constituent phases. To study the influence of the volume fraction of the hard phase, three powder blends were deformed. For the Ag-20/50wt%Ni composites powders with similar particle sizes of about 50 µm were used. Additionally a Ag-2.3wt%Ni composite, which corresponds to Ag-2vol%Ni, was blended with a Ni powder with a particle size between 4 and 7 µm and the 50 µm Ag powder. The harder Ni powder particles exhibited only minor shape changes after compaction and were embedded in the soft Ag matrix, see Figure 18a, b and c for Ag-50/20/2.3wt%Ni. This is in contrast to the Cu-Ag composites, in which both phases were deformed due to the low hardness of the powders, compare with Figure 3b. After applying a strain of γ~380 in the composite with the highest Ni content, Ag-50wt%Ni, a lamellar structure was formed as in the Cu-Ag composites, see Figure 18d. In the Ag-20wt%Ni and Ag-2.3wt%Ni composites original Ni particles were still retained, Figure 18e and f, indicating that the soft Ag matrix carried most of the imposed strain, however, part of the Ni particles deformed by elongation and fracturing. Apparently with increasing Ag content the accommodated strain was increasingly localized in the softer matrix while the fragmentation process of the harder Ni particles became retarded.

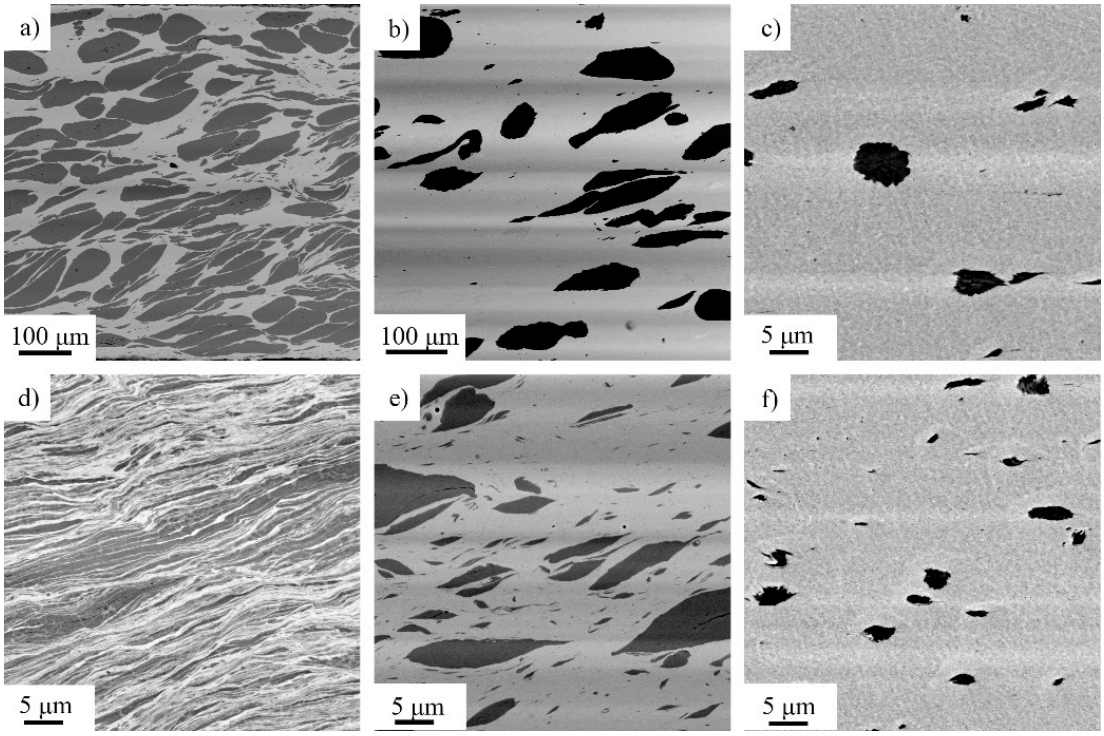

Figure 18: BSE-SEM micrographs recorded in tangential direction showing in the center of HPT samples, where the applied strain is nearly zero for a) Ni-50wt%Ag, b) Ni-20wt%Ag and c) Ag-2.3wt%Ni and micrograph recorded at an applied strain of γ~380 for c) Ag-50wt%Ni, d) Ag-20wt%Ni and e) Ag-2vol%Ni.

A further increase in strain led in the lamellar structure of the Ag-50wt%Ni composite to the formation of shear bands, which resulted in an inhomogeneous microstructure with nanocrystalline regions and retained UFG pure Ag and Ni regions, and even processing at LN

temperature did not lead to a homogeneous structure. Even more pronounced inhomogeneities were observed in the Ag-20wt%Ni composite, see paper IV.

In the Ag-2.3wt%Ni composite increasing the applied strain to γ~760 did not significantly refine the Ni particles, compare Figure 19a with 18f. However, in detailed SEM micrographs a further grain refinement was observed in the Ag matrix from γ~380 to γ~3800, see Figure 19b to f, indicating that some Ni was dissolved in the Ag phase and thereby stabilized a smaller grain size.

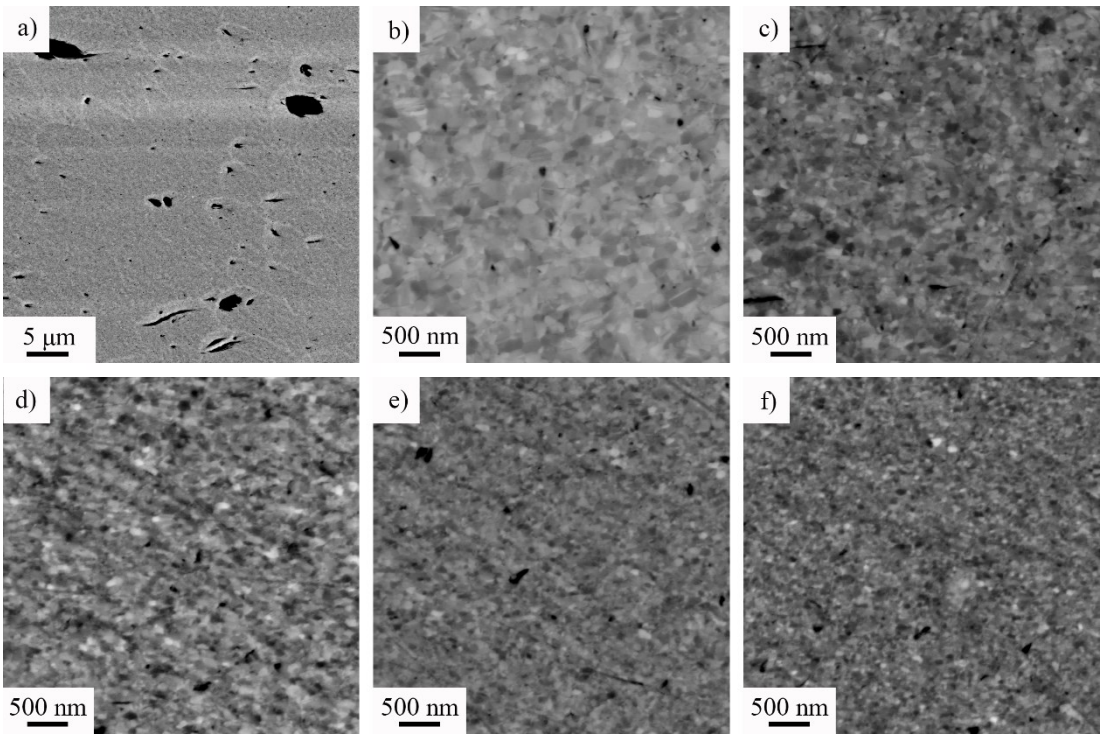

Figure 19: BSE-SEM micrographs of the Ag-2.3wt%Ni composite a) at an applied strain of γ~760, and of the Ag matrix in detail at b) γ~380, c) γ~760, d) γ~1250, e) γ~1900 and f) γ~3800.

The grain refinement process is well reflected in the hardness evolution of the composite, see Figure 20. The hardness increased strongly in the beginning up to strains of γ~1000, but it has not reached a saturation level. This evidence suggests that a homogeneous composite or single-phase alloy could be obtained, if extremely high strains were applied. Further studies are currently in progress to clarify possible supersaturation in Ag-Ni composites with very small amounts of Ni.

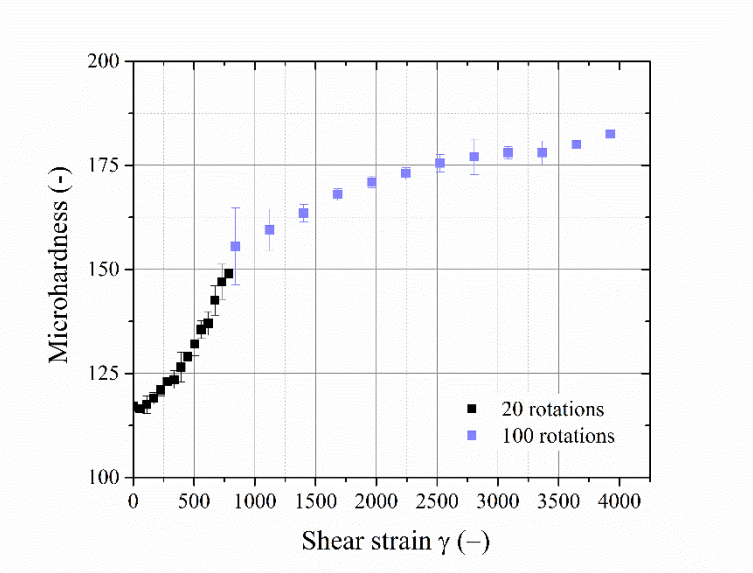

Figure 20: Vickers microhardness evolution as a function of the applied shear strain for the Ag-2.3wt%Ni composite. Measurements of two samples deformed for 20 and 100 rotations are included to cover a large applied strain range.

Compared to the Cu-Ag system, in Ag-Ni composites a different deformation behavior was observed. Co-deformation of Ag and Ni was only observed in the Ag-50wt%Ni composite at low strains before shear banding set in, similar as in the Cu-50wt%Ag composite. In Ag-Ni composites with higher Ag content pronounced strain localization in the softer Ag matrix occurred, causing a retardation of refinement process of the Ni particles, which mainly fragmented by elongation, necking and repeated fracturing. Thus a possible supersaturation process would require extremely high strains.

2.3 Short survey on proposed supersaturation mechanisms

Several concepts were suggested to explain the mechanism of deformation-induced supersaturation and they can be classified into two groups.

The first group defines a critical phase dimension as requirement for supersaturation. It was proposed that dislocations crossing phase boundaries play a key role in the mixing process, for example by Bellon and Averback in the so-called kinetic roughening model [33] or by Raabe et al. in the dislocation shuffling model [34]. If a certain phase dimension is reached the high stress levels enable dislocation glide across phase boundaries [35] and thereby transfer atoms from one phase into the other. Other researchers suggested that small fragments are generated during deformation, which could dissolve into the other phase due to the Gibbs-Thomson effect after reaching a critical size [34,36]. Mechanisms considering the stored energy in interfaces together with an increased defect density as driving force for supersaturation will only get effective if the phases reach nanometer dimensions and a huge amount of interfaces is available [14,15,37].

The second group of proposed mechanisms account for the high amounts of applied strain and are therefore independent of structural sizes. As a consequence, the supersaturation formation would commence with the onset of deformation. Processes similar to erosion or abrasion are hypothesized to gradually dissolve one phase into the other [38]. A fracture and rebonding process was also proposed [27]. The second group is mainly applicable to material systems with a hard and brittle second phase.

Naturally, an experimental verification of these assumptions and clear identification of the underlying supersaturation process is challenging even with highly sophisticated analytical methods such as TEM, atom probe tomography (APT) or nanoindentation, as they can only capture the microstructure and mechanical properties after the experiment. For example the deformation behavior at non-ambient conditions is characterized at RT. Nevertheless, the documented observations can give indications for the operating mechanisms. In this work the most detailed investigations were performed with the Cu-50wt%Ag composite. The supersaturation took place within shear bands as well as in lamellar regions to some extent. In the shear bands enormous amounts of strain are accommodated as revealed by split sample experiments, leading to an extreme grain refinement with consequent mixing of the phases. However, the basic deformation mechanism responsible for realizing these high strains is still unclear. RT nanoindentation experiments revealed only marginal differences in hardness between shear band and lamellar regions, but indicated different deformation behaviors in dual-phase lamellar and single-phase shear band regions, which exhibited a jerky flow behavior, see Figure 8. On the other hand, SAD analysis revealed a classical shear texture in shear band regions, which indicates the prevalence of dislocation activity rather than a transition to other deformation mechanisms such as grain boundary sliding or grain rotation, which are often erroneously considered in UFG or NC materials [39,40]. The same accounts for the lamellar regions, in which only a partial supersaturation was observed as revealed by synchrotron XRD measurements. The main difference in the evolution of the supersaturation as a function of external applied strain in these two regions is the large variation in the locally resolved shear strain. The dissolution seems to take place at phase boundaries which is apparent from the diffuse boundaries at very high strains, compare the lamellar structures in Figure 5d with 6a. Also in the Cu-Ag composites with high and low Ag content it requires a relatively high strain level to reach saturation, suggesting that the supersaturation process starts if the minor phase has reached a critical dimension. Based on these findings it can be argued that in the Cu-Ag

composites a certain phase dimension seems to be a requirement for supersaturation, which is presumably realized by dislocation glide across phase boundaries.

In contrast to Cu-Ag, in the Ag-Ni composites the constituent phases exhibit large hardness differences, which strongly influenced the deformation behavior. In general, in composites with a soft and a hard phase the deformation process is governed by strong strain localization in the soft phase, while the hard phase deforms mainly by elongation, necking and fracturing [41,42]. The effect of strain localization in the soft phase becomes even more pronounced when the hard phase has only a minor volume fraction, as shown for the Ag-2.3wt%Ni composite, in which the fragmentation of the Ni particles is extremely delayed. Nevertheless, the continuous grain refinement in the Ag matrix indicates indirectly a certain dissolution of Ni in the Ag phase. However, for a direct confirmation further XRD experiments need to be done in future. On the other hand, when the volume fraction of the hard phase is high enough strain localization can be prevented and complete supersaturation can be obtained, as demonstrated in Ag-70/90wt%Ni composites [43], which were deformed in a two-step HPT process (for experimental details see [44]). Comparisons can be drawn to the Cu-Co system, which deforms similar as the Ag-Ni system, and was intensively studied by Bachmaier et al. [11,28,38,45]. The most intriguing finding in these studies was that already at relatively low applied strains, $\gamma \sim 43$, the intermixing process started as proven with APT measurements [38], however, only in fragments of Cu or Co which had nanometer dimensions. Therefore a sequence of different processes was proposed. First small fragments are generated by an abrasion-like process which are then finally dissolved by a defect-based mechanisms like for example dislocation-shuffling.

In summary, the experimental observations indicate that a critical phase dimension is required in any case to enable deformation-induced supersaturation irrespective of material system and deformation temperature. However, the fundamental deformation processes in different material systems have a strong influence on the progression and efficiency of the mixing process depending if co-deformation of the phases or localized deformation dominates. An overview on deformation-induced supersaturation during HPT processing of the immiscible systems Cu-W, Cu-Cr, Cu-Fe, Cu-Ag, Cu-Co and Ni-Ag can be found in paper IV.

3 Summary and Conclusions

The main focus of this study was the process of deformation-induced supersaturation during SPD deformation of usually immiscible material systems. For this purpose the Cu-Ag system was chosen as model material and studied systematically for different compositions and processing parameters. For comparison also Ni-Ag composites were investigated in order to evaluate the influence of the differences in the hardness levels of the constituent phases.

Several factors determine the degree of supersaturation during HPT deformation of immiscible systems. On the one hand processing parameters, mainly the applied strain and the processing temperature are significant. And on the other hand characteristics of the material systems, namely the volume fraction and hardness levels of the constituent phases, which can strongly influence the deformation behavior.

The supersaturation process does not start until a certain strain level is reached leading to a critical phase dimension, as shown in detail in TEM investigations and synchrotron XRD analyses. In the Cu-10 and 90wt%Ag composites co-deformation of the constituent phases leads to continuous thinning of the minor phases during stage A and B until they completely dissolve in the matrix. In regime C a single-phase solid solution is obtained as shown schematically in Figure 21a. In the Cu-50wt%Ag composite pronounced shear band formation occurs in regime B. In regime C enormous strains are accommodated by shear bands resulting in complete supersaturation within the shear bands. Because most of the imposed strain is carried by few shear bands, the supersaturation process in the retained lamellar matrix is delayed and only partial supersaturation is achieved. Consequently, even at the highest applied strain level no homogeneous microstructure could be obtained, see schematic in Figure 21b. Due to the positive heat of mixing there is large thermodynamic driving force for decomposition if the temperature is increased and post-annealing experiments, see Figure 15, 16 and 17, clearly show that already at relatively low temperatures phase separation takes place. The individual phases sustain therefore at elevated processing temperatures, see Figure 21c, irrespective of applied strain. While in Cu-10 and 90wt%Ag composites single-phase solid solutions are achievable at RT, in the Cu-50wt%Ag composite the critical temperature for full supersaturation is below RT. A homogenous single-phase supersaturated solid solution could be obtained only by processing at LN temperature, see schematic in Figure 21d.

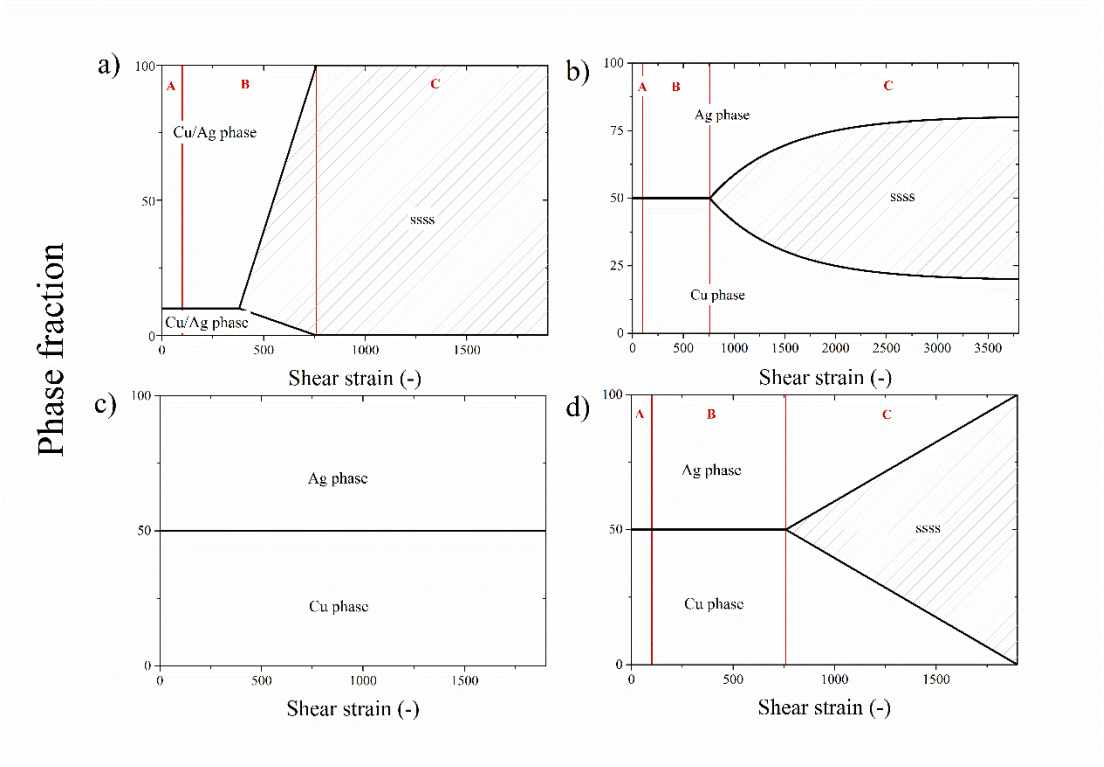

Figure 21: Phase fraction as a function of applied strain for a) the Cu-10wt%Ag composite at RT, for the Cu-50wt%Ag composite b) at RT, c) at 200 °C and d) at LN.

The obtained results for the Cu-Ag system are summarized in a "saturation phase diagram" in Figure 22. We use quotations marks because it is not a phase diagram in terms of an thermodynamic equilibrium but should visualize instead the microstructures obtained at the highest strain level at different processing temperatures and compositions.

In general, a transition from single-phase supersaturated solid solution to complete phase-separated composites takes place with increasing deformation temperature. Additionally, in the medium composition range shear band-assisted partial supersaturation can lead to composites with Cu-rich, Ag-rich and supersaturated phases (possessing the nominal composition of the composite). The temperature regime in which single-phase supersaturated solid solutions can be generated strongly depends on the volume fraction of the phases.

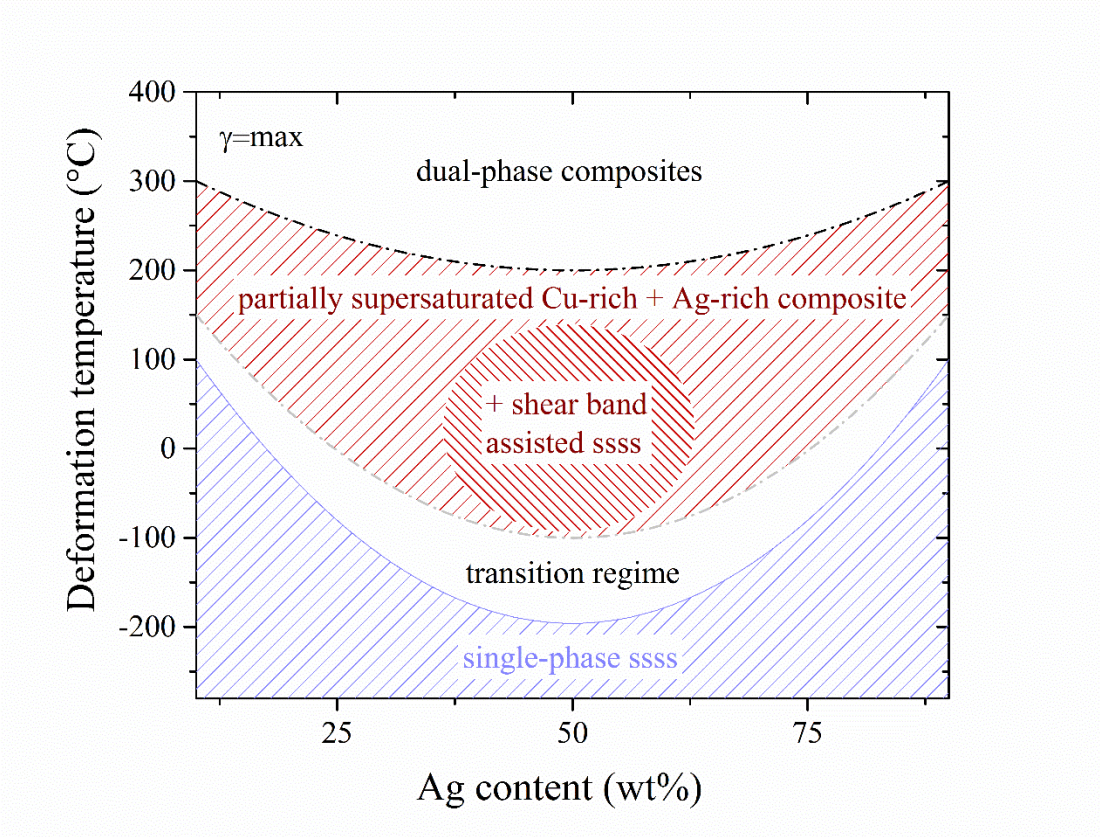

Figure 22: "Saturation phase diagram" for the Cu-Ag system with a single-phase supersaturated solid solution (ssss) zone at low processing temperatures and a dual-phase pure Cu and Ag zone at elevated temperatures. In between a dual-phase zone with Cu- and Ag-rich solid solutions exists. Additionally, in the medium composition range a shear band assisted supersaturated solid solution with the nominal composition is formed leading to a tri-phase zone. (Taken from paper V.)

In contrast to the Cu-Ag system, in which both phases have similar saturation hardness levels, in the Ni-Ag system the constituent phases exhibit a large hardness difference. Co-deformation of the phases only takes place when the Ni volume fraction is relatively high as in Ag-50wt%Ni. With decreasing Ni volume fraction pronounced strain localization in the softer Ag matrix occurs, as shown for the Ag-2.3wt%Ni composite, where the refinement of the Ni particles is extremely delayed, which possibly hinders a supersaturation process or at least demands very high applied strains.

In conclusion the volume fractions and hardness levels of the constituent phases control the deformation mechanisms of the composites during HPT processing and consequently influence possible supersaturation processes.

Bibliography

[1] A. Bachmaier, A. Hohenwarter, R. Pippan, New procedure to generate stable nanocrystallites by severe plastic deformation, Scr. Mater. 61 (2009) 1016–1019.

[2] J.D. Verhoeven, W.A. Spitzig, L.L. Jones, H.L. Downing, C.L. Trybus, E.D. Gibson, L.S. Chumbley, L.G. Fritzemeier, G.D. Schnittgrund, Development of deformation processed copper-refractory metal composite alloys, J. Mater. Eng. 12 (1990) 127–139.

[3] J. Bevk, J.P. Harbison, J.L. Bell, Anomalous increase in strength of in situ formed Cu-Nb multifilamentary composites, J. Appl. Phys. 49 (1978) 6031–6038.

[4] J.D. Embury, M.A. Hill, W.A. Spitzig, Y. Sakai, Microstructural Aspects of Materials for Nondestructive Long-Pulse High-Field Magnets, MRS Bull. (1993) 57–60.

[5] J. Freudenberger, N. Kozlova, A. Gaganov, L. Schultz, H. Witte, H. Jones, Magnetoresistance up to 50 T of highly strengthened Cu – Ag conductors for pulsed high field magnets, Cryogenics 46 (2006) 724–729.

[6] D. Raabe, K. Miyake, H. Takahara, Processing , microstructure , and properties of ternary high-strength Cu – Cr – Ag in situ composites, Mater. Sci. Eng. A291 (2000) 186–197.

[7] P. Gorria, D. Martínez-Blanco, R. Iglesias, S.L. Palacios, M.J. Pérez, J.A. Blanco, L. Fernández Barquín, A. Hernando, M.A. González, Magneto-volume effects in Fe-Cu solid solutions, J. Magn. Magn. Mater. 300 (2006) 229–233.

[8] P. Gorria, D. Martínez-Blanco, J.A. Blanco, M.J. Pérez, A. Hernando, L.F. Barquín, R.I. Smith, High-temperature induced ferromagnetism on γ-Fe precipitates in FeCu solid solutions, Phys. Rev. B 72 (2005) 014401.

[9] A.E. Berkowitz, J.R. Mitchell, M.J. Carey, A.P. Young, S. Zhang, F.E. Spada, F.T. Parker, A. Hutten, G. Thomas, Giant magnetoresistance in heterogeneous Cu-Co alloys, Phys. Rev. Lett. 68 (1992) 3745–3748.

[10] J. Wecker, R. Von Helmolt, L. Schultz, K. Samwer, Giant magnetoresistance in melt spun Cu-Co alloys, Appl. Phys. Lett. 62 (1993) 1985–1987.

[11] A. Bachmaier, M. Pfaff, M. Stolpe, H. Aboulfadl, C. Motz, Phase separation of a supersaturated nanocrystalline Cu-Co alloy and its influence on thermal stability, Acta Mater. 96 (2015) 269–283.

[12] Y. Li, D. Raabe, M. Herbig, P.-P. Choi, S. Goto, A. Kostka, H. Yarita, C. Borchers, R. Kirchheim, Segregation stabilizes nanocrystalline bulk steel with near theoretical strength, Phys. Rev. Lett. 113 (2014) 106104.

[13] K. Uenishi, K.F. Kobayashi, K.N. Ishihara, P.H. Shingu, Formation of a supersaturated solid solution in the Ag-Cu system by mechanical alloying, Mater. Sci. Eng. A 134 (1991) 1342–1345.

[14] C. Gente, M. Oehring, R. Bormann, Formation of thermodynamically unstable solid solutions in the Cu-Co system by mechanical alloying, Phys. Rev. B 48 (1993) 244–252.

[15] J. Eckert, J.C. Holzer, C.E. Krill III, W.L. Johnson, Mechanically driven alloying and grain size changes in nanocrystalline Fe-Cu powders, J. Appl. Phys. 73 (1993) 2794–2802.

[16] E. Ma, J.-H. He, P.J. Schilling, Mechanical alloying of immiscible elements: Ag-Fe contrasted with Cu-Fe, Phys. Rev. B 55 (1997) 5542–5545.

[17] J. Xu, U. Herr, T. Klassen, R.S. Averback, Formation of supersaturated solid solutions in the immiscible Ni–Ag system by mechanical alloying, J. Appl. Phys. 79 (1996) 3935–3945.

[18] Y. Ogino, T. Yamasaki, S. Murayama, R. Sakai, Non-equilibrium phases formed by mechanical alloying of Cr-Cu alloys, J. Non. Cryst. Solids 117/118 (1990) 737–740.

[19] E. Gaffet, C. Louison, M. Harmelin, F. Faudot, Metastable phase transformations induced by ball-milling in the CuW system, Mater. Sci. Eng. A 134 (1991) 1380–1384.

[20] A.R. Yavari, P.J. Desré, Thermodynamics and kinetics of amorphisation during mechanical alloying, Mater. Sci. Forum 88-90 (1992) 43–50.

[21] A. Hohenwarter, A. Bachmaier, B. Gludovatz, S. Scheriau, R. Pippan, Technical parameters affecting grain refinement by high pressure torsion, Int. J. Mat. Res. 100 (2009) 1653–1661.

[22] R. Pippan, S. Scheriau, A. Taylor, M. Hafok, A. Hohenwarter, A. Bachmaier, Saturation of Fragmentation During Severe Plastic Deformation, Annu. Rev. Mater. Res. 40 (2010) 319–343.

[23] O. Renk, A. Hohenwarter, S. Wurster, R. Pippan, Direct evidence for grain boundary motion as the dominant restoration mechanism in the steady-state regime of extremely cold-rolled copper, Acta Mater. 77 (2014) 401–410.

[24] M. Hafok, R. Pippan, Comparison of single crystalline and polycrystalline behavior under high pressure torsion, Mater. Sci. Forum 550 (2007) 277–282.

[25] R. Pippan, F. Wetscher, M. Hafok, A. Vorhauer, I. Sabirov, The Limits of Refinement by Severe Plastic Deformation, Adv. Eng. Mater. 8 (2006) 1046–1056.

[26] A. Bachmaier, R. Pippan, Generation of metallic nanocomposites by severe plastic deformation, Int. Mater. Rev. 58 (2013) 41–62.

[27] A. Bachmaier, G.B. Rathmayr, M. Bartosik, D. Apel, Z. Zhang, R. Pippan, New insights on the formation of supersaturated solid solutions in the Cu–Cr system deformed by high-pressure torsion, Acta Mater. 69 (2014) 301–313.

[28] A. Bachmaier, H. Aboulfadl, M. Pfaff, F. Mücklich, C. Motz, Structural evolution and strain induced mixing in Cu-Co composites studied by transmission electron

microscopy and atom probe tomography, Mater. Charact. 100 (2015) 178–191.

[29] C. Gammer, C. Mangler, H.P. Karnthaler, C. Rentenberger, Three-Dimensional Analysis by Electron Diffraction Methods of Nanocrystalline Materials, Microsc. Microanal. 17 (2011) 866–871.

[30] V. Maier, A. Hohenwarter, R. Pippan, D. Kiener, Thermally activated deformation processes in body-centered cubic Cr - How microstructure influences strain-rate sensitivity, Scr. Mater. 106 (2015) 42–45.

[31] J.M. Wheeler, R. Raghavan, J. Michler, *In situ* SEM indentation of a Zr-based bulk metallic glass at elevated temperatures, Mater. Sci. Eng. A 528 (2011) 8750–8756.

[32] A.L. Greer, Y.Q. Cheng, E. Ma, Shear bands in metallic glasses, Mater. Sci. Eng. R 74 (2013) 71–132.

[33] P. Bellon, R.S. Averback, Nonequilibrium Roughening of Interfaces in Crystals under Shear: Application to Ball Milling, Phys. Rev. Lett. 74 (1995) 1819–1822.

[34] D. Raabe, S. Ohsaki, K. Hono, Mechanical alloying and amorphization in Cu–Nb–Ag in situ composite wires studied by transmission electron microscopy and atom probe tomography, Acta Mater. 57 (2009) 5254–5263.

[35] A. Misra, R.G. Hoagland, Plastic flow stability of metallic nanolaminate composites, J. Mater. Sci. 42 (2007) 1765–1771.

[36] A.R. Yavari, P.J. Desré, T. Benameur, Mechanically Driven Alloying of Immiscible Elements, Phys. Rev. Lett. 68 (1992) 2235–2238.

[37] X. Quelennec, A. Menand, J.M. Le Breton, R. Pippan, X. Sauvage, Homogeneous Cu–Fe supersaturated solid solutions prepared by severe plastic deformation, Philos. Mag. 90 (2010) 1179–1195.

[38] A. Bachmaier, J. Schmauch, H. Aboulfadl, A. Verch, C. Motz, On the process of co-deformation and phase dissolution in a hard-soft immiscible Cu-Co alloy system during high-pressure torsion deformation, Acta Mater. 115 (2016) 333–346.

[39] H. Conrad, J. Narayan, On the grain size softening in nanocrystalline materials, Scr. Mater. 42 (2000) 1025–1030.

[40] N.Q. Chinh, P. Szommer, Z. Horita, T.G. Langdon, Experimental evidence for grain-boundary sliding in ultrafine-grained aluminum processed by severe plastic deformation, Adv. Mater. 18 (2006) 34–39.

[41] D. Edwards, I. Sabirov, W. Sigle, R. Pippan, Microstructure and thermostability of a W-Cu nanocomposite produced via high-pressure torsion, Philos. Mag. 92 (2012) 4151–4166.

[42] X. Sauvage, P. Jessner, F. Vurpillot, R. Pippan, Nanostructure and properties of a Cu-Cr composite processed by severe plastic deformation, Scr. Mater. 58 (2008) 1125–1128.

[43] A. Bachmaier, J. Keckes, K.S. Kormout, R. Pippan, Supersaturation in Ag–Ni alloy by two-step high-pressure torsion processing, Philos. Mag. Lett. (2013).

[44] A. Bachmaier, M. Kerber, D. Setman, R. Pippan, The formation of supersaturated solid solutions in Fe–Cu alloys deformed by high-pressure torsion, Acta Mater. 60 (2012) 860–871.

[45] A. Bachmaier, M. Stolpe, T. Müller, C. Motz, Phase decomposition and nano structure evolution of metastable nanocrystalline Cu-Co solid solutions during thermal treatment, IOP Conf. Ser. Mater. Sci. Eng. 89 (2015) 012017.

4 List of appended papers

Paper I

K.S. Kormout, B. Yang, R. Pippan

Transmission electron microscope investigations on Cu-Ag alloys produced by high-pressure torsion

IOP Conf. Series: Materials Science and Engineering 63 (2014) 012092.

Paper II

K.S. Kormout, B. Yang, R. Pippan

Deformation behavior and microstructural evolution of Cu-Ag alloys processed by high-pressure torsion

Advanced Engineering Materials 12 (2015) 1828-1834.

Paper III

K.S. Kormout, P. Ghosh, V. Maier-Kiener, R. Pippan

Deformation mechanisms during severe plastic deformation of a Cu-Ag composite

Accepted for publication in Journal of Alloys and Compounds

Paper IV

K.S. Kormout, R. Pippan, A. Bachmaier

Deformation-induced supersaturation in immiscible systems during high-pressure torsion

Submitted for publication in Advanced Engineering Materials

Paper V

K.S. Kormout, P. Ghosh, R. Pippan

Effect of processing temperature on deformation and supersaturation behavior during severe plastic deformation of Cu-Ag composites

In preparation

Remarks

In the appended papers, myself, Karoline Sophie Kormout, performed all experiments, the data analyses and the composition of the publications with the following exceptions:

- In **paper I**

  Dr. Bo Yang participated with helpful discussions.

- In **paper II**

- Dr. Bo Yang participated with helpful discussions.

- In **paper III**

  Dr. Pradipta Ghosh helped performing synchrotron XRD measurements and analyzing the data. Dr. Verena Maier-Kiener performed the nanoindentation experiments.

- In **paper IV**

  Dr. Andrea Bachmaier participated with giving ideas and helpful discussions.

- In **paper V**

  Dr. Pradipta Ghosh helped performing synchrotron XRD measurements and analyzing the data.

- My supervisor, Prof. Reinhard Pippan, participated in all the papers by giving the basic ideas for the publications and with helpful discussions during their preparation.

I Transmission electron microscope investigations on Cu-Ag alloys produced by high-pressure torsion

K.S. Kormout[1], B. Yang[1], R. Pippan[1,2]

[1]Erich Schmid Institute of Materials Science, Austrian Academy of Sciences

[2]Department of Materials Physics, Montanuniversität Leoben

Abstract. Cu-Ag alloys in three different compositions (Cu–25/50/75wt%Ag) were produced by powder consolidation followed by high-pressure torsion. Deformation was performed till a saturation regime was reached. The generated microstructures were investigated by transmission electron microscopy and vary from ultra-fine grained to nanocrystalline to even partially amorphous structures. Vickers hardness measurements show a strong increase in hardness compared with the pure metals, annealing at 130°C leads to an additional increase in hardness.

I.1 Introduction

Severe plastic deformation (SPD) techniques like high-pressure torsion (HPT) are well-known methods to produce nanostructured alloys from all kind of materials [1,2]. The fabrication of nanocrystalline composite alloys from usually immiscible elements has attracted interest due to possible novel properties, for example high electrical and thermal conductivity [3, 4]. Particularly mechanical alloying was used in the past to obtain and study this new type of alloys and related phenomena such as supersaturation and amorphization [5–8].

Processing materials with HTP leads to dense bulk materials under controlled deformation states. Depending on material and process parameters (like temperature, pressure) a critical strain is limiting a period of continuous grain refinement (and associated hardening) followed by a saturation regime, where no further changes take place. In this also called steady state regime the material is ultrafine-grained (UFG) or even nanocrystalline (nc) and exhibits special microstructural features characteristic for SPD materials [9]. In this study the eutectic Cu-Ag system [10] was chosen as model material, which has a positive heat of mixing, very low room temperature (RT) solubility, and a lattice mismatch of ~12%. The structural evolution in this system during ball milling has been investigated in few studies. Fcc supersaturated solid solutions have been reported over the whole composition range [11–13], and also amorphization occurred in some studies [7, 8]. One of the disadvantages of ball milling is the undefined applied strain, the effect of environment and an end product in powder form. In the present study the structural evolution during HPT after application of well-defined strains will be investigated.

I.2 Experimental

Due to the eutectic character of the CuAg system the microstructures strongly vary with the composition when produced by casting. Differences in the initial state of the material influence the deformation behavior and lead to a complex microstructural evolution of those alloys [16–18]. To avoid the influence of the initial microstructure elemental powders of Cu

(purity: 99.7 %, particle size: 63 µm) and Ag (purity: 99.99 %, particle size: 54 µm) were mixed in three different compositions (Cu-25/50/75wt% Ag). Then the powders were consolidated directly in the HPT tool, followed by immediate processing. The generated bulk material is disk shaped with diameter of 8 mm and a thickness of 0.5 mm. For each composition samples were processed for 100 rotations at RT, thus to a shear strain of γ=4400 at a radius of 3.5 mm. For the Cu-50wt% Ag composition additionally samples were produced at a processing temperature of 200 °C for 75 rotations (γ=3300 at a radius of 3.5 mm) and samples processed to 200 and 300 rotations at RT (γ=8800 and γ=13200 at a radius of 3.5 mm, respectively). The applied pressure was between 5 and 7.5 GPa, with a rotational speed of 0.6 rotations per minute. The evolving microstructure was investigated by transmission electron microscopy (TEM). TEM samples were prepared by a standard procedure: material was glued into Ti holders, followed by grinding, dimple grinding and ion milling till perforation using a Gatan PIPS 691 with 4kV and cooled with liquid nitrogen. TEM images were recorded in radial direction at a radius of 3.5 mm unless otherwise specified. Bright-field (BF), dark-field (DF) and selected area diffraction (SAD) patterns were recorded on a Philips CM12. High-resolution TEM (HRTEM) was conducted on a JEOL TEM/STEM 2100F at 200 kV equipped with an image-side C_S-corrector (CEOS). Grain sizes were determined by measuring grain areas by hand in TEM DF images and calculating an equivalent circle diameter. Vickers microhardness measurements were performed on a Buehler Micromet 5100 using a load of 500 g and indents were placed in 0.25 mm distances along the cross-section of the 8 mm disk. Hardness measurements were done for all three compositions on the samples processed for 100 rotations; in the as-deformed state, as well as in annealed samples. Annealing was performed after the HPT process at 130 °C for 30 min in air.

I.3 Results and discussion

During the HPT process the initial µm-sized powder particles are strongly refined through a repeated shearing process. The material was deformed until a steady state is reached.

The generated microstructures of Cu-25/50/75wt% Ag alloys in or near this saturation regime are shown in BF and DF TEM micrographs (see Figure I.1), the samples were processed for 100 rotations (a total shear strain of γ=4400 at a radius of 3.5 mm). All three specimens are homogenously refined (within the limits of TEM sample size). The Cu-25wt% Ag sample (see Figure I.1a and d) shows the largest grain size of 100±37 nm, which is between the ultra-fine grained (UFG) and nanocrystalline regime. The grains are equi-axed with sharp grain boundaries, showing various twins and other defects displayed as contrast variations inside the grains. The microstructures of Cu–50wt% and 75wt% Ag can be defined as nanocrystalline. The grains are slightly elongated in the 75wt% Ag sample (visible from DF images in Figure I.1f), and clearly elongated in the 50wt% Ag sample along the shear direction (see DF in Figure I.1e). Twins were found occasionally in Cu-75wt% Ag (encircled in Figure I.1c) and only rarely in the 50wt% Ag sample. Due to the very fine microstructure a clear identification of the grains and grain boundaries is difficult. A determination of the grain size of the Cu-50wt% Ag was not possible, for Cu-75wt% Ag a grain size of 31±10 nm was determined. It should be noted that grain sizes were measured from DF images with only few grains in favorable orientation, and therefore may not be representative. The trend however is evident from TEM micrographs. The strong grain refinement is also reflected in the SAD patterns. In the SAD pattern of the Cu-25wt% Ag sample (see inset in Figure I.1a) single spots are still visible in the rings due to relatively large grains (aperture size: 200 µm). In comparison a broadening of the rings in the Cu-50wt% and 75wt% Ag samples (see insets in Figure I.1b and c) demonstrates the very small grain size.

Vickers hardness measurements as a function of strain reveal for all three compositions a typical increase in hardness until a saturation level is reached (see Figure I.2a). The maximum hardness is decreasing with increasing Ag-content: with 378±4.5 HV for Cu-25wt% Ag, 343±6 HV for Cu-50wt% Ag and 300±4 HV for Cu-75wt% Ag (mean values calculated from 5 indents at the edge of the disk). All alloys exhibited higher hardness than the pure metals (for reference: maximum hardness for Cu ~215 HV [19] and for Ag ~100 HV); coupled with a finer grain size in the alloys compared with the pure metals, which usually show grain sizes in the UFG regime. The highest hardness was obtained in the Cu-25wt% Ag alloy, although the grain size is significantly coarser than in the other samples. One reason is the higher Cu-content due to the higher hardness of pure Cu. Additionally the high amount of twins are lowering the actual structural dimension for dislocation motion and therefore influence the hardness.

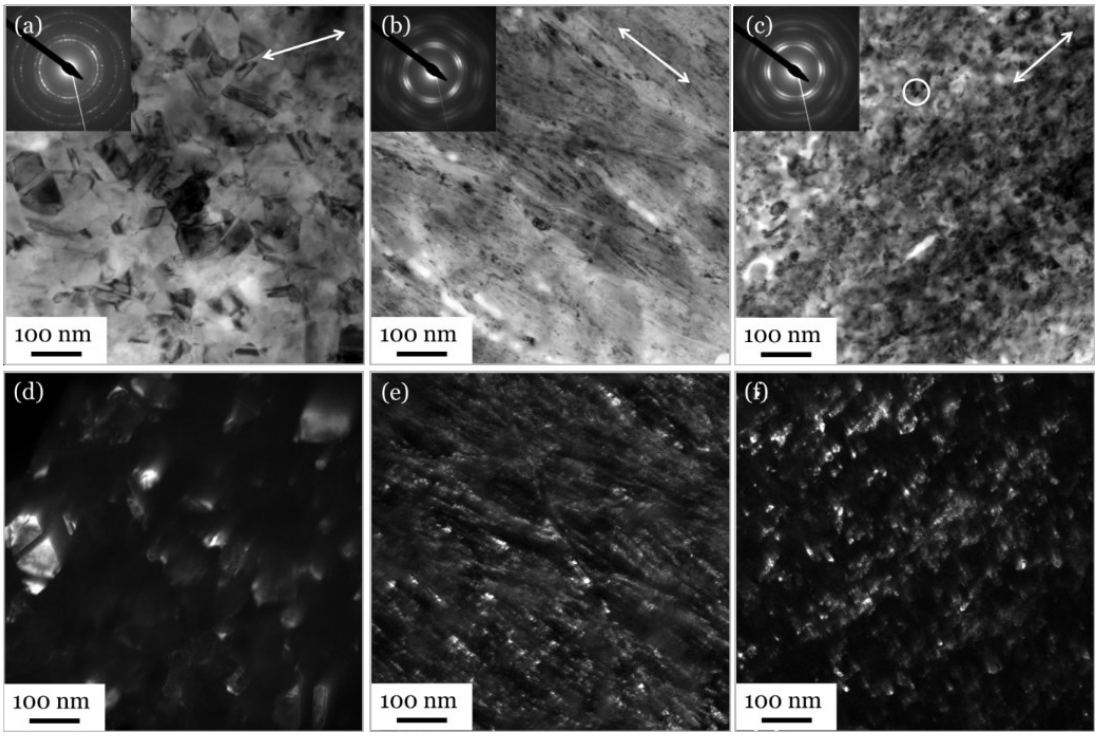

Figure I.1: TEM BF and DF images of (a) and (d) Cu-25wt% Ag, (b) and (e) Cu-50wt% Ag and (c) and (f) Cu-75wt% Ag with corresponding SAD pattern (see insets), all alloys deformed at RT to a total shear strain of γ=4400; the shear plane is indicated with an arrow.

In order to investigate the effect of sample preparation heating experiments were conducted. Annealing the samples at 130 °C for 30 min (which reflects the heat treatment in the sample preparation process) leads to a hardness increase (see Figure I.2b), indicating that some "recovery" processes had taken place, but no grain growth occurred. Such a hardness increase after annealing has been reported in several systems, in alloys as well as in pure metals. Bachmaier et al. [20] produced alloys in the immiscible Cu-Fe system by HPT, they obtained complete supersaturated solid solutions at lower and higher Cu content. Annealing those samples led to decomposition into the stable fcc Cu and bcc Fe phases, consequently to an increase in the fraction of interfaces in the material, which is causing the observed hardness increase. Anomalous hardening during annealing was also reported in pure Cu and Ni, caused by the formation of twins [21]. The distribution and type of twins, the grain size and

morphology and type of grain boundaries are fundamental for an understanding of the behavior of SPD deformed materials. A systematically study on the microstructural characteristics in as-deformed and annealed samples is an issue of further investigations.

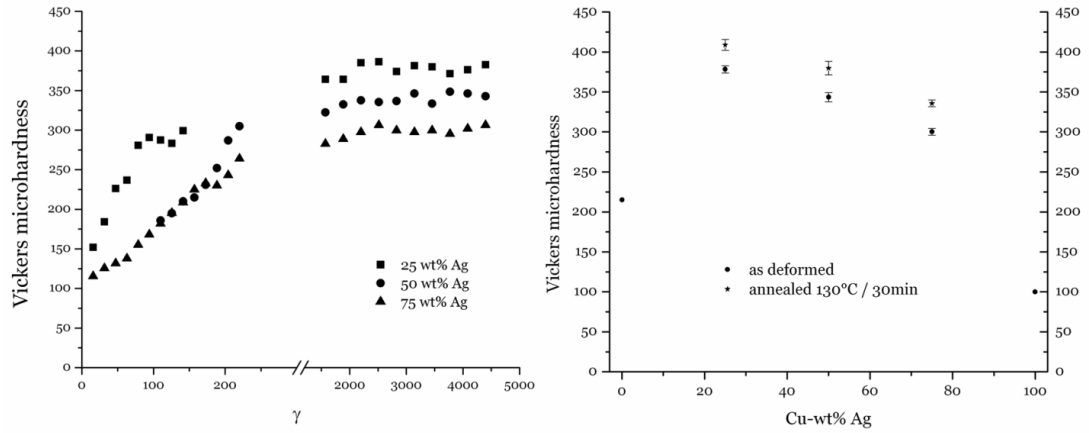

Figure I.2: (a) Vickers microhardness evolution as a function of strain for Cu-25/50/75wt% Ag, (b) Vickers microhardness depending on composition in the as-deformed and annealed state with reference values for pure Cu and Ag.

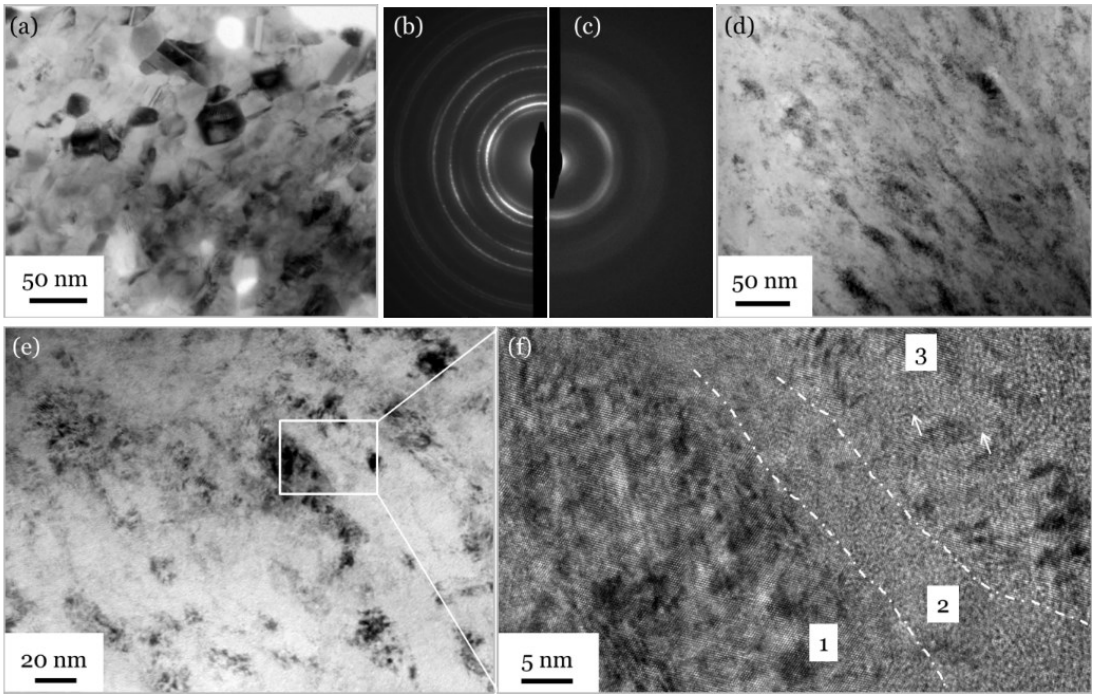

Figure I.3: TEM BF images and related SAD pattern of Cu50wt%Ag alloy processed by HPT to a total shear strain of (a) and (b) γ=3300 (processed at 200°C), (c) and (d) γ=8800 (processed at 200°C till γ= 2000, then at RT till γ=8800) and (e) γ=13200 (RT, recorded in plan-view) with high resolution image in (f).

Because the Cu-50wt% Ag sample shows an extremely fine and unusual structure, additional investigations were made on this composition. In Figure I.3a and d the microstructure of a sample processed at 200 °C is compared to a sample processed at RT (notice different applied shear strains of γ=3300 and γ=8800, respectively). The elevated processing temperature at 200 °C resulted in a coarser but still nanocrystalline microstructure with well-defined grains. The structure in Figure I.3d shows that further deformation to a strain of γ=8800 at RT lead to marginal additional grain refinement of the lamellar structure and a changed appearance compared with Figure I.1b. Structural elements are still elongated; contrast-rich darker grains are surrounded by bright featureless regions. The SAD pattern of the sample produced at 200 °C shows two sets of sharp diffraction rings including the Cu and Ag phase (see Figure I.3b). In the RT deformed sample (Figure I.3c) these rings broaden and merge into each other, pointing to a mixture of the two phases and extreme grain refinement. The change of the rings into diffuse halos indicates an amorphization of the structure.

Additional deformation to a strain of γ=13 200 brought no further refinement or amorphization of the microstructure (see Figure I.3e, observations in plan-view at a radius of 3.5 mm). HRTEM imaging revealed that the dark contrast-rich regions are crystalline with a complex defect structure (referred as regions 1 and 3 in Figure I.3f). Disordered regions (labelled as 2 in Figure I.3f) are apparent in between the crystalline regions, confirming the amorphous nature of the bright featureless areas. The amorphization mainly occurs between grains (at former grain or phase boundaries), but also starts inside the grains (see grain 3, indicated with arrows), dividing them into smaller segments.

I.4 Conclusion

Cu-Ag alloys in three compositions with Cu-25/50/75wt% Ag were produced using elemental powders and HPT processing. Due to similar hardness and shear modulus of Cu and Ag both phases are co-deformed uniformly. With evolving shearing and continuous refinement of the structural dimensions saturation in grain size and hardness is reached at very high strains. The obtained material characteristics are summarized in table I.1.

Table I.1: Summary of the obtained hardness values, grain sizes and microstructural characteristics.

	100% Cu	Cu-25wt%Ag	Cu-50wt%Ag	Cu-75wt%Ag	100% Ag
microhardness as-deformed HV	215 [19]	378±4.5	343±6	300±4.3	~ 100
microhardness annealed HV		409±7	380±8	335±4	
grain size [nm]	240 [19]	100 ± 37	-	31 ± 10	480 [22]
Microstructural features	UFG	UFG composite, numerous twins	nc, partial amorphization	nc composite, few twins	UFG

The resulting grain size and hardness depends strongly on composition. The Cu-25wt% Ag exhibited the largest grain size and surprisingly the highest hardness. With increasing Ag content the hardness is decreasing, despite a finer grain size of the alloys. In Cu-50wt% Ag samples a partial amorphous structure was obtained at very high strains, the disordering of crystallinity was not only observed at former grain or phase boundaries, but also appeared inside the grains, leading to further fragmentation.

HPT deformation at lower temperatures could lead to further amorphization. HPT processing and annealing experiments will be extended and properties of different material states will be studied systematically in further investigations.

Acknowledgement

We gratefully acknowledge the financial support of the Austrian Science Fund (FWF): P24429.

References

[1] R.Z. Valiev, R.K. Islamgaliev, I.V. Alexandrov, Bulk nanostructured materials from severe plastic deformation, Prog. Mater. Sci.45 (2000) 103–189.

[2] A. Bachmaier, R. Pippan, Generation of metallic nanocomposites by severe plastic deformation, Int. Mater. Rev.58 (2013) 41–62.

[3] E. Ma, Alloys created between immiscible elements, Prog. Mater. Sci. 50 (2005) 413–509.

[4] Y. Sakai, H.-J. Schneider-Muntau, ULTRA-HIGH STRENGTH, HIGH CONDUCTIVITY Cu-Ag ALLOY WIRES, Acta Mater. 45 (1997) 1017–1023.

[5] F. Wu, D. Isheim, P. Bellon, D.N. Seidman, Nanocomposites stabilized by elevated-temperature ball milling of Ag50Cu50 powders: An atom probe tomographic study, Acta Mater. 54 (2006) 2605–2613.

[6] Y.F. Sun, H. Fujii, T. Nakamura, N. Tsuji, D. Todaka, M. Umemoto, Critical strain for mechanical alloying of Cu–Ag, Cu–Ni and Cu–Zr by high-pressure torsion, Scr. Mater.65 (2011) 489–492.

[7] F. Wu, P. Bellon, A.J. Melmed, T.A. Lusby, FORCED MIXING AND NANOSCALE DECOMPOSITION IN BALL-MILLED Cu–Ag CHARACTERIZED BY APFIM, Acta Mater. 49 (2001) 453–461.

[8] S. Zghal, M.J. Hÿtch, J.P. Chevalier, R. Twesten, F. Wu, P. Bellon, Electron microscopy nanoscale characterization of ball-milled Cu–Ag powders. Part I: Solid solution synthesized by cryo-milling, Acta Mater. 50 (2002) 4695–4709.

[9] X. Sauvage, G. Wilde, S.V. Divinski, Z. Horita, R.Z. Valiev, Grain boundaries in ultrafine grained materials processed by severe plastic deformation and related phenomena, Mater. Sci. Eng. A 540 (2012) 1–12.

[10] T. B. Massalski, J.L. Murray, L.H. Bennet, H. Baker, Binary alloy phase diagrams. Metals Park, Ohio: American Society for Metals, 1986.

[11] T. Klassen, U. Herr, R.S. Averback, BALL MILLING OF SYSTEMS WITH POSITIVE HEAT OF MIXING: EFFECT OF TEMPERATURE IN Ag–Cu, Acta Mater. 45 (1997) 2921–2930.

[12] H. Shen, Z. Li, B. Günther, A.V. Korznikov, R.Z. Valiev, Influence of powder consolidation methods on the structural and thermal properties of a nanophase Cu-50wt%Ag alloy, Nanostructured Mater. 6 (1995) 385–388.

[13] R. Najafabadi, D.J. Srolovitz, E. Ma, M. Atzmon, Thermodynamic properties of metastable Ag-Cu alloys, J. Appl. Phys. 74 (1993) 3144–3149.

[14] H.W. Sheng, G. Wilde, E. Ma, The competing crystalline and amorphous solid solutions in the Ag – Cu system, Acta Mater. 50 (2002) 475–488.

[15] Z.Q. Li, H. Shen, L. Chen, Y. Li, B. Günther, Effect of compaction pressure on the microstructure of mechanically alloyed Ag37Cu63 alloy, Philos. Mag. 72 (1995) 1485–1493.

[16] Y.Z. Tian, S.D. Wu, Z.F. Zhang, R.B. Figueiredo, N. Gao, T.G. Langdon, Comparison of microstructures and mechanical properties of a Cu–Ag alloy processed using different severe plastic deformation modes, Mater. Sci. Eng. A 528 (2011) 4331–4336.

[17] Y.Z. Tian, S.D. Wu, Z.F. Zhang, R.B. Figueiredo, N. Gao, T.G. Langdon, Microstructural evolution and mechanical properties of a two-phase Cu–Ag alloy

processed by high-pressure torsion to ultrahigh strains, Acta Mater. 59 (2011) 2783–2796.

[18] Y.Z. Tian, J.J. Li, P. Zhang, S.D. Wu, Z.F. Zhang, M. Kawasaki, Microstructures, strengthening mechanisms and fracture behavior of Cu–Ag alloys processed by high-pressure torsion, Acta Mater. 60 (2012) 269–281.

[19] L. Krämer, Production and characterization of particle-stabilized nanocrystalline Cu for high temperature applications, diploma thesis, Montanuniversität Leoben, 2014.

[20] A. Bachmaier, M. Kerber, D. Setman, R. Pippan, The formation of supersaturated solid solutions in Fe–Cu alloys deformed by high-pressure torsion, Acta Mater. 60 (2012) 860–871.

[21] N. Jia, X. Zhao, D. Song, M.H. Zhou, Y.D. Wang, On the anomalous hardening during annealing of heavily deformed f.c.c. metals, Mater. Sci. Eng. A 527 (2010) 1143–1150.

[22] M. Hafok, R. Pippan, Influence of stacking fault energy and alloying on stage V hardening of HPT-deformed materials, Int. J. Mat. Res. 101 (2010) 1097–1104.

II Deformation Behavior and Microstructural Evolution of Cu-Ag Alloys Processed by High-Pressure Torsion

K.S. Kormout, B. Yang and R. Pippan

[1]Erich Schmid Institute of Materials Science, Austrian Academy of Sciences

[2]Department of Materials Physics, Montanuniversität Leoben

Abstract. In this study different Cu-Ag alloys (Cu-10/25/50/75/90wt% Ag) are produced by powder consolidation and subsequent high-pressure torsion processing. The microstructural evolution of the material state is investigated by SEM and TEM. Additionally, mechanical properties are characterized by Vickers microhardness measurements. The deformation mechanism changes from homogenous co-deformation in the very beginning of the process to shear banding. When the hardness reaches a saturation level, all compositions show grain sizes below 100 nm with a very high defect density and hardness compared to pure ultrafine-grained Cu or Ag. Single-phase solid solutions are reached at both high and low Ag content, in the medium composition range a mixture of single- and two-phase regions is observed.

II.1 Introduction

Severe plastic deformation (SPD) techniques have become suitable methods to produce bulk ultrafine-grained or nanocrystalline alloys from different material classes [1–4]. Even in otherwise challenging material systems such as immiscible systems the fabrication of nanocomposites or multi-phase materials is achievable [3,5–8]. The formation of supersaturated solid solutions (ssss) during SPD processing was already shown for several immiscible materials systems [9–12]. The proposed mixing mechanisms reach from diffusion-assisted approaches [13–15] over purely mechanical mixing mechanisms [16,17] to mechanisms considering the enormous amount of applied strain [9,18] in such processing routes.

To understand the mixing of the components, it is necessary to follow the deformation behavior during the SPD process. While the deformation mechanisms during high-pressure torsion (HPT) processing in pure metals or single-phase alloys are intensively investigated [19–22], in two- or multi-phase materials a detailed analysis is still needed. Depending on several material characteristics, such as composition/volume fraction of the components, differences in hardness/Young´s modulus, the initial size and shape of the existing phases, and the lattice structures, a variety of microstructures can evolve.

Cu-Ag alloys produced by conventional casting techniques show varying microstructures dependent on composition and cooling rate; different composites of Cu-rich, Ag-rich and eutectic phases can be formed. Tailoring the structure of such composites by cooling rate and subsequent heat treatment for specific properties was successfully realized by A. Gaganov and co-wokers [23] and K.S. Raju and co-workers [24]. Microstructural characteristics also strongly influence the deformation behavior and lead to a complex microstructural evolution

during SPD [25–27]. To avoid influences of initial microstructural features, processing of immiscible systems via a powder route was successfully realized [28,29]. During the HPT deformation, the compacted powder particles are continuously sheared. For large applied shear strains γ and co-deformation of the components, the thickness after deformation d of a component with an initial thickness of d_0 can be estimated with the following equation [29]:

$$d = \frac{d_0}{\gamma} \quad . \tag{II.1}$$

In order to study the underlying deformation mechanisms and the formation of ssss, the Cu-Ag system was chosen as a model material. The Cu-Ag system is a eutectic system with low solubility at room temperature and a lattice mismatch of about 12% [30]. Both elements have similar mechanical properties, therefore, it is expected that co-deformation will take place. The formation of ssss has been shown by several research groups [31–35], and even amorphization has been observed in this system [36]. These reasons make the Cu-Ag system an ideal model system to study deformation mechanisms in such composites and fundamental mechanisms that lead to mixing between immiscible elements during SPD processing.

II.2 Experimental details

In this study Cu (purity: 99.7 %, mean particle size: 63 μm) and Ag (purity: 99.99 %, mean particle size: 54 μm) powders were mixed in five compositions: Cu-10/25/50/75/90wt% Ag. The powder mixtures were consolidated directly in the HPT tool and subsequently deformed between 2 and 100 rotations, hence, a maximal shear strain γ of 4400 has been applied. The rotational speed was between 0.2 and 0.6 rotations per minute with a pressure of 7.5 GPa. The disk dimensions were 8 mm in diameter and 0.5 mm in thickness. Microstructural investigations were conducted using a scanning electron microscope (SEM) LEO1525 and a (scanning) transmission electron microscope (S)TEM JEOL JEM-2100F. Observation directions are specified in Figure II.1. TEM micrographs were recorded from the top view at a radius of 2.5 mm (±0.3 mm due to varying hole dimension and position). TEM samples were prepared by a standard procedure: grinding, polishing and dimple grinding with subsequent ion milling. Special care was taken to avoid any heating of the sample during preparation. Vickers hardness measurements were performed on a Buehler Micromet 5100 applying a load of 500 g across the transverse section of the HPT disk in distances of 0.25 mm each.

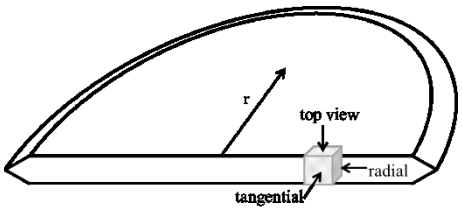

Figure II.1: Schematic diagram of a HPT disk: observation directions (top view, radial, tangential) are indicated.

II.3 Results

The initial powder particles, as shown in the SEM image in Figure II.2a for the powder mixture of Cu-50wt%Ag, have a rather broad particle size distribution (particle dimensions ranging from a few μm up to 100 μm). The particle shape can be considered as spherical for

the Ag powder; the Cu shows a dendrite-like shape. After compaction of the powder and HPT deformation to a strain of $\gamma = 75$ (two rotations at a radius of 3 mm), a lamellar microstructure is formed independent of alloy composition as shown in Figure II.2b-f. The Cu phases appear dark, the Ag phases bright due to different scattering factors. The initial powder particles are strongly elongated and the phase boundaries are aligned parallel to the shearing direction, with some phase boundaries showing serrations. In the Cu-10/90wt%Ag alloys (Figure II.2b and f) the respective minority phase is uniformly distributed with some isolated larger lamellae. In the medium composition range (Cu-25/50/75wt%Ag) a rather inhomogeneous structure was observed (Figure II.2c-e). Lamellae thickness varies strongly for Cu and Ag phases between only few nm and 2000 nm. Single lamellae can be hundreds of µm long.

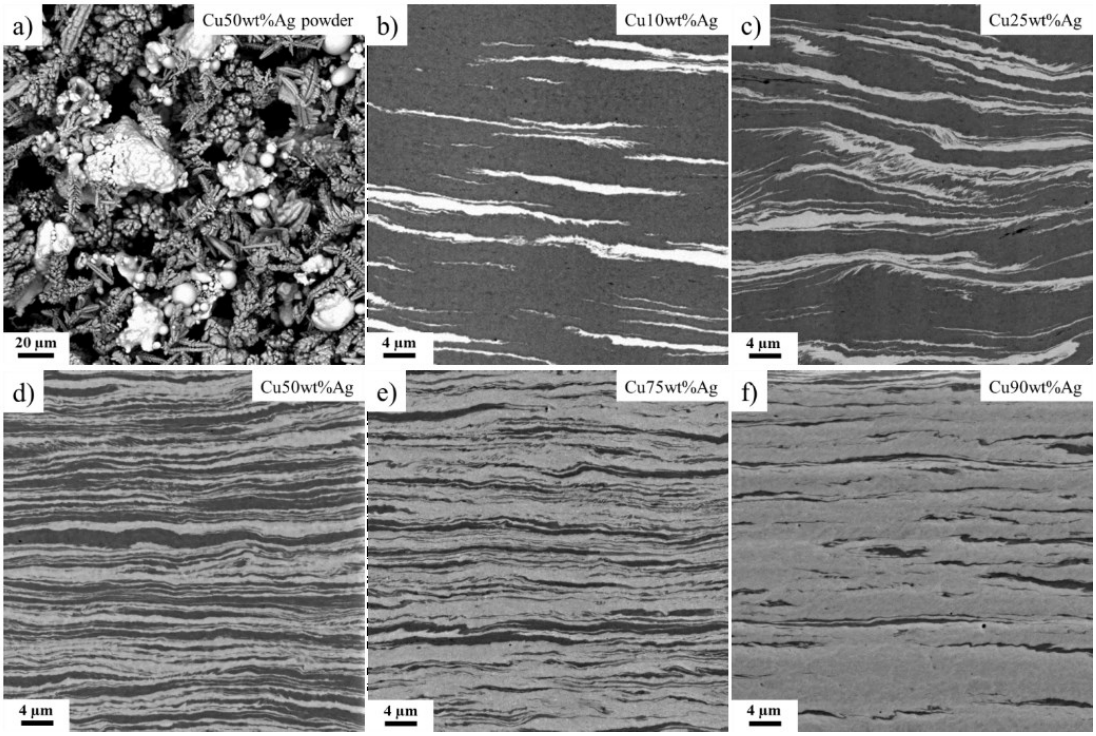

Figure II.2: SEM images (backscatter mode) of a) powder mixture of Cu-50wt%Ag, and different Cu-Ag alloys processed for two rotations, images observed at a radius of 3 mm ($\gamma = 75$) in the tangential direction: b) Cu-10wt%Ag, c) Cu-25wt%Ag, d) Cu-50wt%Ag, e) Cu-75wt%Ag, f) Cu-90wt%Ag.

Figure II.3 shows the microstructure observed in different viewing directions for Cu-50wt%Ag. A top view on the HPT disk reveals large Cu and Ag plates in the size range of the initial powder particles. The microstructures in the radial and tangential directions appear similar. In these directions the Cu/Ag phases are strongly elongated and aligned parallel to the shear plane. In the radial direction this alignment is even more pronounced, in the tangential direction the phase boundaries occur somewhat wavy. Serrated phase boundaries are observed in all viewing directions.

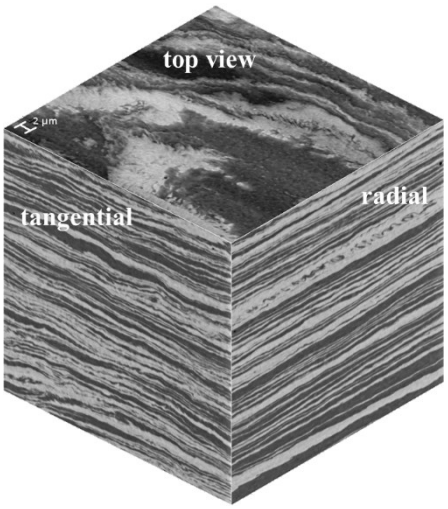

Figure II.3: SEM images observed in top view, tangential and radial directions at a $\gamma = 75$ for Cu-50wt%Ag.

From electron backscatter diffraction (EBSD) scans (see Figure II.4) changes in the grain size were verified. Comparing a Cu-rich region in the Cu-50wt% composite to pure Cu (both at strains of about 75) show similar grain sizes (Figure II.4a and b), while for the pure Cu deformed to a saturation level (30 rotations, shear strain $\gamma \approx 1100$) a finer structure was observed (see Figure II.4c). For Ag-rich regions in the Cu-50wt%Ag composite (Figure II.4d) a grain size comparable to that in pure Ag deformed to saturation (Figure II.4e) was observed.

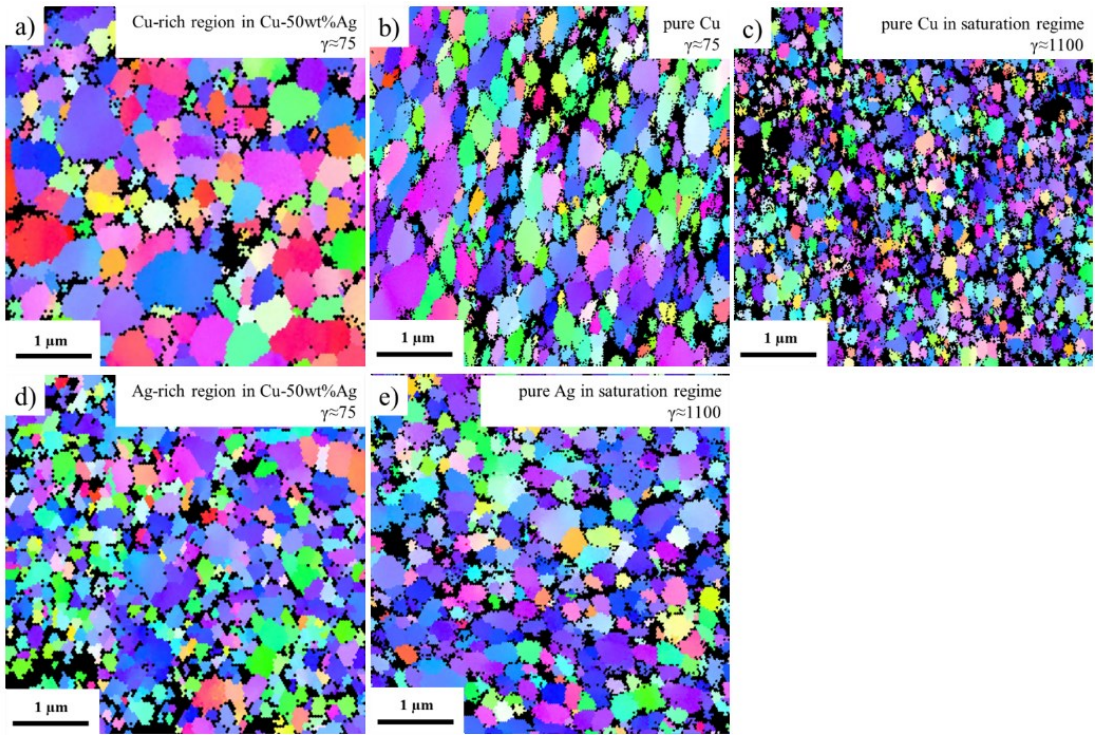

Figure II.4: EBSD scans of a) Cu-rich region in Cu-50wt%Ag, b)and c) pure Cu at different strains, d) Ag-rich region in Cu-50wt%Ag and e) pure Ag. Scans in a), b) and d) are recorded in top view at a radius of 3 mm on samples deformed for 2 rotations; scans in c) and e) are recorded in top view on samples deformed for 30 rotations.

After powder compaction the particles are flattened and there is no indication of the original powder shape as shown for Cu-50wt%Ag in Figure II.5a. The image was recorded in the center of the disk deformed for two rotations, the shear strain is nearly zero ($\gamma = 0$ to $\gamma = 7.5$, depending on uncertainties during cutting); the strain induced by the initial compression is about $\varepsilon \approx 20\%$. Increasing the strain up to $\gamma = 75$ leads to elongation and alignment of the particles as already shown for all compositions in Figure II.2. While at $\gamma = 75$ serrated phase boundaries are rarely found, by increasing the strain they become a major type of phase boundaries (see Figure II.5b). The phase boundaries are deviating from the strict alignment in the shear direction. An increase in strain to $\gamma = 188$ as shown in Figure II.5c results in further refinement of the lamellar structure; the grain structure can be only determined by SEM in larger remained lamellae as shown in detail in Figure II.5e. Bright bands are assumed to be Ag-rich and dark bands Cu-rich, a precise determination of the degree of intermixing, which possibly occurs at phase boundaries, is not possible at this point. In the brighter Ag-rich band the grain size is much smaller than in the darker Cu-rich band, both fit well to the EBSD scans at lower strains (see Figure II.4). Shear band-like features begin to appear as marked by an arrow in Figure II.5c. By reaching a strain of $\gamma = 250$, the microstructure is extensively refined (see Figure II.5d) compared to the initial coarse grained sample after compaction. In detailed images (Figure II.5f) one can still find lamellae with a thickness up to 300 nm as indicated by arrows. In the marked Cu-rich bands, individual grains can still be resolved; the grain size is strongly refined compared to Figure II.5e and is comparable to the grain size of pure Cu in the saturation regime as shown in the EBSD scan in Figure II.4c. At this state numerous shear bands can be found and the strict alignment in shear direction is almost completely lost. Instead,

most lamella packages are oriented under different angles, one example is indicated in Figure II.5d.

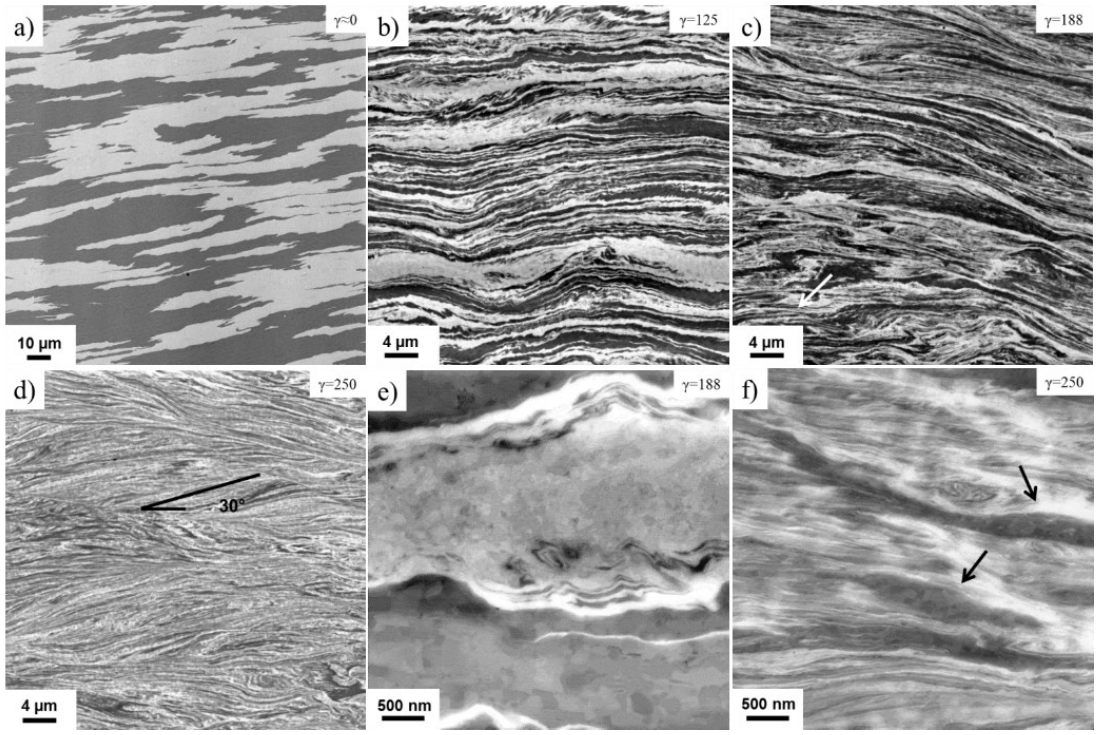

Figure II.5: SEM micrographs of the Cu-50wt%Ag alloy along the tangential direction deformed to a strain of a) $\gamma \approx 0$, b) $\gamma = 125$, c) $\gamma = 188$ with a shear band marked by the white arrow, d) $\gamma = 250$, lamella package orientation related to shear direction is indicated, and in higher magnifications for e) $\gamma = 188$ and f) $\gamma = 250$, black arrows mark Cu-rich bands.

The microstructural formation of the composites is also reflected in the hardness evolution. Three regimes can be identified in the hardness plot in Figure II.6 for all alloys. The very early evolution in hardness at γ smaller than 5 is not considered because a certain strain is required to obtain a bulk sample. Up to a shear strain of about 100, the hardness remains nearly constant before a strong increase is observed. At a strain of about 500, the hardness levels off again and a saturation regime is reached. The hardness evolution of pure Cu and a mean hardness value for pure Ag, both powders deformed maximum up to 30 rotations (when almost the whole sample is in the hardness saturation regime) is also included. Compared to the pure metals a strong increase in hardness is observed.

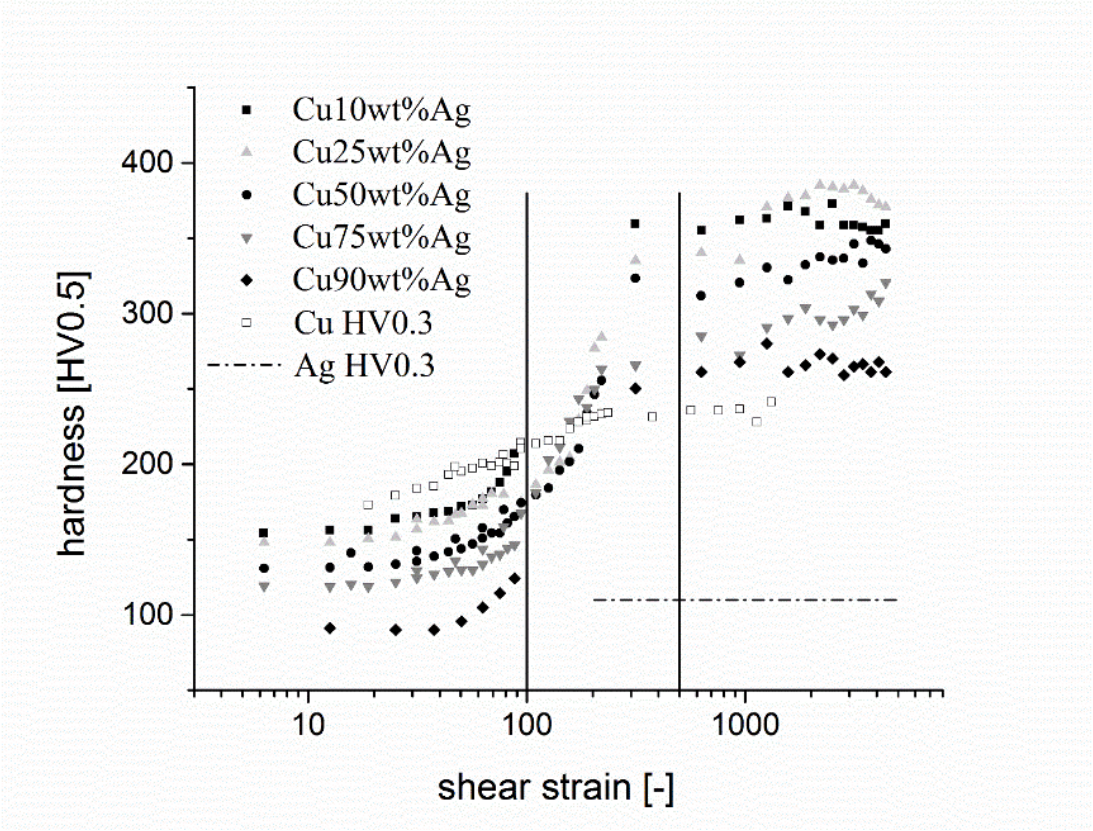

Figure II.6: Hardness evolution of Cu-10/25/50/75/90wt%Ag alloys and pure Cu; for Ag a mean hardness value in the saturation regime is included. Please note the logarithmic scale for the strain.

Microstructures of all alloys investigated in the hardness saturation regime at a strain $\gamma \approx 4400$ are shown in Figure II.7. It is evident that in all compositions nanocrystalline microstructures are formed. Similar microstructures were already published in reference [38], due to unknown period of heat treatment during sample preparation, the microstructures in the Cu-25/75wt%Ag samples are different to this study. In the Cu-50wt%Ag alloy, little influence of the preparation route was observed; a material state close to amorphous was found in both studies.

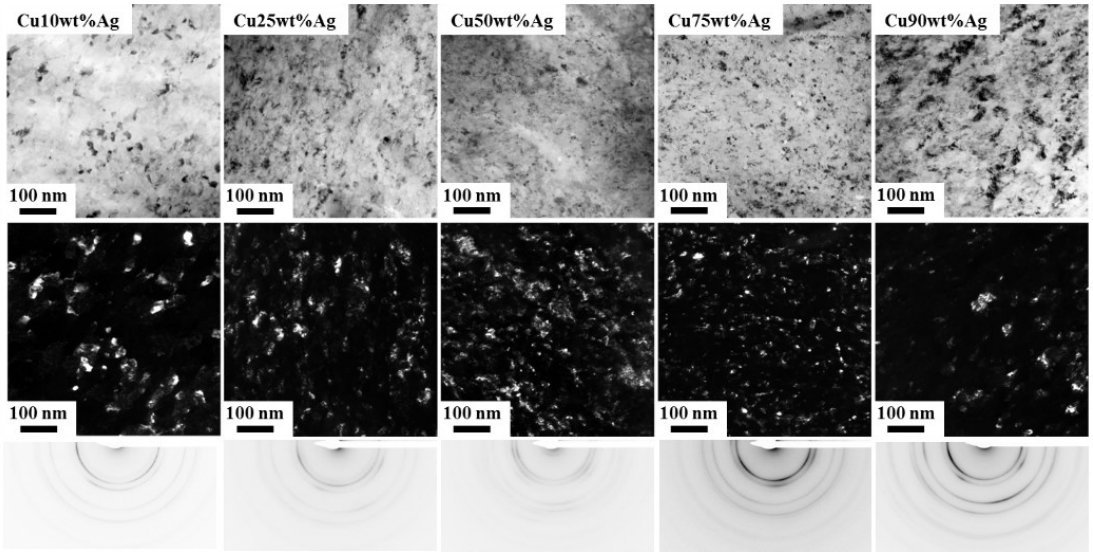

Figure II.7: TEM bright field (top row) and dark field (middle row) images, and selected area diffraction patterns (bottom row) of different Cu-Ag alloys observed at a radius of ~2mm (at a strain of $\gamma \approx 4400$) from the top view.

Dark speckles in the grain interior of the bright grains in dark field images (middle row in Figure II.7) indicate the very high defect density. Twins were found occasionally in Cu-10/90wt%Ag alloys. The evaluation of selected area diffraction patterns (examples shown in the bottom row in Figure II.7) revealed that Cu-10/90wt%Ag alloys are mostly single phase, although two-phase areas can be found, however, rare. While in the medium composition range, a mixture of single-phase and two-phase regions occurred. A detailed analysis of the highly complex microstructures and the degree of inhomogeneity in the alloys is beyond the scope of this paper, but is currently under investigation.

II.4 Discussion

The initial state of the microstructure after powder compaction, as shown in Figure II.5a, is already aligned in shearing direction. In the beginning of the deformation process, the powder particles are elongated and reduced in thickness (see Figure II.2). A very well aligned lamellar structure evolves. In Cu-10/90wt%Ag alloys, the respective minor phase is distributed uniformly, while at medium compositions Cu-25/50/75wt%Ag a variation in the starting lamella thickness between 1 and 50 µm occurred due to the rather broad particle size distribution. Following equation (II.1) after applying a shear strain of $\gamma = 125$, these lamellae are reduced to thicknesses between 8 and 400 nm. These differences are indeed observed as shown in Figure II.5b. In the interior of the separate Cu and Ag bands an ultrafine-grained structure is formed. It is assumed that the fragmentation inside these bands follows the same deformation mechanism as in pure metals, namely the formation of dislocation cells and blocks [20], and is usually finished at strains below $\gamma = 15$ for bulk samples. For powder compacted samples, a surface oxide layer can lead to stronger grain refinement and thus higher hardness than in high-purity bulk samples; the saturation regime in this case is delayed to higher strains as discussed by Bachmaier and co-workers [28]. Comparing EBSD scans for pure Cu as shown in Figure II.4 with the hardness evolution in Figure II.6 demonstrates that this observation is also valid for the Cu powder used in this study. However, it was not observed for the Ag

powder. Therefore, a constant hardness is observed in the beginning in the Ag-rich composites (Cu-75/90wt%Ag), while for Cu-rich composites (Cu-10/25/50wt%Ag) a slight increase is found. In this first hardness plateau, the lamellar structure of the composites is continuously refined while, additionally, the grain size in the Cu lamellae also decreases. Both phases, Cu and Ag, are deforming simultaneously (co-deformation). No localization of deformation was observed in this regime due to similar hardness and Young´s modulus of the two elements. The perfect alignment of the lamellae is becoming disturbed after increasing the strain up to about $\gamma = 100$ (compare Figure II.2d and Figure II.5b). The phase boundaries become serrated and wavy. This leads to an additional refinement of microstructural elements where single bands are divided in smaller fragments. This process accelerates the refinement of the microstructures towards a nanocomposite. With ongoing HPT processing, the deformation cannot be realized by solely dislocation motion and shear band-like features become visible, indicated by an arrow in Figure II.5c. These shear band features increase in number and are dominant at strains higher than 250. The microstructure is extremely refined, although pure Cu and Ag bands with spacing up to 300 nm still exist. The serration of phase boundaries and shear banding was also reported by Tian and co-workers for a Cu-28wt%Ag cast-alloy deformed by HPT [26] and for a cold-rolled Cu-71.9wt%Ag cast-alloy [39]. The initial Cu/Ag spacings in the eutectic regions were in the range of 1 μm. The serration of interfaces and also the shear banding started at lower strains than in the present study. These characteristics are consequently governed by the phase spacing.

When the saturation region is reached, refinement and fragmentation processes are in equilibrium with restoration processes. TEM analysis of the alloys, processed until the hardness saturation is reached, showed nanocrystalline microstructures for all compositions. While samples at high and low Ag content (Cu-10/90wt%Ag) are to a large extent single-phase, in the medium composition range, especially at Cu-50wt%Ag, a composite of two-phase and single-phase ssss regions were observed. At high and low Ag content, it is assumed that the inhomogeneities in the initial powder mixtures, as shown in SEM micrographs in Figure II.2, proceed up to very high strains. To overcome this problem of refinement of very coarse initial phases, a two-step HPT process could be used. This process has been successfully applied by Bachmaier and co-workers for the Cu-Fe and Ni-Ag system [29,37]. In these studies a second HPT deformation process was realized by cutting small disks out of a large HPT samples and the shear plane in the second HPT step is rotated by 90°. Because lamella alignment and the shear plane are perpendicular to each other, the continuing HPT process is much more effective. Much lower strains are needed for the same thickness reduction, as calculated in literature [29]. The fundamental deformation and mixing mechanism will accordingly also occur at lower strains, and possible final microstructural states can be investigated more easily.

In the case of Cu-50wt%Ag composites, it is believed that no homogenous single phase ssss CuAg can be obtained even at significantly larger strains or in the two-step HPT process. It might be that the final saturation state is a nanocomposite of Ag-rich and Cu-rich ssss. The limits of the amount of supersaturation and the deformation mechanisms which result in a saturation microstructure are not clear. These phenomena need a much deeper analysis, which is challenging even for pure metals [40], and are far beyond the scope of this paper.

II.5 Conclusion

Different Cu-Ag alloys (Cu-10/25/50/75/90wt%Ag) were processed by HPT up to shear strains of $\gamma = 4400$. It was shown that all compositions deform in a similar manner. In the beginning co-deformation of initial Cu and Ag powder particles was observed due to similar hardness and Young´s modulus of the components. Cu and Ag are strongly elongated and

aligned along the shear plane. In the interior of the Cu and Ag lamellae an ultrafine-grained structure is formed by dislocation motion similar to pure metals. At a strain of $\gamma = 188$, shear band-like features start to occur, which become dominant with ongoing deformation. When the hardness saturation is reached, a nanocrystalline microstructure is formed in all alloys. Homogenous single-phase ssss alloys were obtained only at low and high Ag contents, at medium compositions a composite of single-phase ssss and two-phase Cu-rich and Ag-rich ssss regions was observed. The limits of supersaturation are still unclear and further detailed analysis is needed. It is concluded that the deformation is independent of composition, but the initial particle size and distribution have an influence on the homogeneity of the alloys.

Acknowledgement

Funding for this work has been provided by the Austrian Science fund (FWF) under Project: P24429 and the European Research Council under ERC Grant Agreement No. 340185 USMS.

References

[1] R.Z. Valiev, R.K. Islamgaliev, I.V. Alexandrov, Prog. Mater. Sci. 45 (2000) 103.

[2] R.Z. Valiev, Y. Estrin, Z. Horita, T.G. Langdon, M.J. Zehetbauer, Y.T. Zhu, *Jom* **2006**, 33.

[3] A. Bachmaier, R. Pippan, *Int. Mater. Rev.* **2013**, *58*, 41.

[4] T.C. Lowe, R.Z. Valiev, *JOM* **2000**, 27.

[5] X. Sauvage, R. Pippan, *Mater. Sci. Eng. A* **2005**, *410-411*, 345.

[6] I. Sabirov, R. Pippan, *Scr. Mater.* **2005**, *52*, 1293.

[7] G. Wilde, H. Rösner, *J. Mater. Sci.* **2007**, *42*, 1772.

[8] K. Edalati, S. Toh, M. Watanabe, Z. Horita, *Scr. Mater.* **2012**, *66*, 386.

[9] A. Bachmaier, G.B. Rathmayr, M. Bartosik, D. Apel, Z. Zhang, R. Pippan, *Acta Mater.* **2014**, *69*, 301.

[10] S. Odunuga, Y. Li, P. Krasnochtchekov, P. Bellon, R.S. Averback, *Phys. Rev. Lett.* **2005**, *95*, 045901.

[11] X. Quelennec, A. Menand, J.M. Le Breton, R. Pippan, X. Sauvage, *Philos. Mag.* **2010**, *90*, 1179.

[12] X. Sauvage, F. Wetscher, P. Pareige, *Acta Mater.* **2005**, *53*, 2127.

[13] V.M. Farber, *Met. Sci. Heat Treat.* **2002**, *44*, 317.

[14] B.B. Khina, B. Formanek, *Defect Diffus. Forum* **2006**, *249*, 105.

[15] M. Angiolini, F. Cardellini, M. Krasnowski, G. Mazzone, A. Montone, M. Vittori-Antisari, *Microsc. Microanal. Microstruct.* **1995**, *6*, 601.

[16] P. Bellon, R.S. Averback, *Phys. Rev. Lett.* **1995**, *74*, 1819.

[17] D. Raabe, S. Ohsaki, K. Hono, *Acta Mater.* **2009**, *57*, 5254.

[18] I. Sabirov, O. Kolednik, R. Pippan, *Metall. Mater. Trans. A* **2005**, *36*, 2861.

[19] Y. Estrin, A. Vinogradov, *Acta Mater.* **2013**, *61*, 782.

[20] R. Pippan, S. Scheriau, A. Taylor, M. Hafok, A. Hohenwarter, A. Bachmaier, *Annu. Rev. Mater. Res.* **2010**, *40*, 319.

[21] H. Jiang, Y.T. Zhu, D.P. Butt, I.V. Alexandrov, T.C. Lowe, *Mater. Sci. Eng. A* **2000**, *290*, 128.

[22] K. Edalati, Z. Horita, *Acta Mater.* **2011**, *59*, 6831.

[23] A. Gaganov, J. Freudenberger, W. Grünberger, L. Schultz, *Z. Met.* **2004**, *95*, 425.

[24] K.S. Raju, V.S. Sarma, A. Kauffmann, Z. Hegedüs, J. Gubicza, M. Peterlechner, J. Freudenberger, G. Wilde, *Acta Mater.* **2013**, *61*, 228.

[25] J. Gubicza, Z. Hegedüs, J.L. Lábár, V.S. Sarma, A. Kauffmann, J. Freudenberger, *IOP Conf. Ser. Mater. Sci. Eng.* **2014**, *63*, 012091.

[26] Y.Z. Tian, X.H. An, S.D. Wu, Z.F. Zhang, R.B. Figueiredo, N. Gao, T.G. Langdon, *Scr. Mater.* **2010**, *63*, 65.

[27] Y.Z. Tian, S.D. Wu, Z.F. Zhang, R.B. Figueiredo, N. Gao, T.G. Langdon, *Scr. Mater.* **2011**, *65*, 477.

[28] A. Bachmaier, A. Hohenwarter, R. Pippan, *Scr. Mater.* **2009**, *61*, 1016.

[29] A. Bachmaier, M. Kerber, D. Setman, R. Pippan, *Acta Mater.* **2012**, *60*, 860.

[30] T.B. Massalski, J.L. Murray, L.H. Bennet, H. Baker, *Binary Alloy Phase Diagrams*, American Society For Metals, Metals Park, Ohio **1986**.

[31] M. Pouryazdan, D. Schwen, D. Wang, T. Scherer, H. Hahn, R.S. Averback, P. Bellon, *Phys. Rev. B* **2012**, *86*, 144302.

[32] S. Ohsaki, S. Kato, N. Tsuji, T. Ohkubo, K. Hono, *Acta Mater.* **2007**, *55*, 2885.

[33] H. Shen, B. Günther, H. Schäfer, Z. Li, Z. Qi, *Scr. Metall. Mater.* **1995**, *32*, 1677.

[34] F. Wu, P. Bellon, A.J. Melmed, T.A. Lusby, *Acta Mater.* **2001**, *49*, 453.

[35] S. Zghal, M.J. Hÿtch, J.-P. Chevalier, R. Twesten, F. Wu, P. Bellon, *Acta Mater.* **2002**, *50*, 4695.

[36] H.W. Sheng, G. Wilde, E. Ma, *Acta Mater.* **2002**, *50*, 475.

[37] A. Bachmaier, J. Keckes, K.S. Kormout, R. Pippan, *Philos. Mag. Lett.* **2013**.

[38] K.S. Kormout, B. Yang, R. Pippan, *IOP Conf. Ser. Mater. Sci. Eng.* **2014**, *63*, 012092.

[39] Y.Z. Tian, Z.F. Zhang, *Scr. Mater.* **2013**, *68*, 542.

[40] O. Renk, A. Hohenwarter, S. Wurster, R. Pippan, *Acta Mater.* **2014**, *77*, 401.

III Deformation mechanisms during severe plastic deformation of a Cu-Ag composite

K.S. Kormout[1], P. Gosh[1], V. Maier-Kiener[2], R. Pippan[1]

[1]Erich Schmid Institute of Materials Science, Austrian Academy of Sciences

[2]Department of Physical Metallurgy and Materials Testing, Montanuniversität Leoben

Abstract. A Cu-37at%Ag composite was produced by high-pressure torsion processing of elemental Cu and Ag powders at room temperature. The initial micrometer-sized powder particles were compressed directly in the high-pressure torsion tool and subsequently deformed to different strain levels. The microstructural evolution was studied in detail by scanning and transmission electron microscopy and synchrotron X-Ray measurements, and related to the mechanical properties by microhardness and nanoindentation measurements. The HPT process led to an alignment of Cu and Ag into a lamellar composite microstructure. With increasing applied strain the Cu and Ag lamellae were continuously thinned and simultaneously an ultrafine-grained microstructure was formed in the separate Cu and Ag lamellae. When the lamella spacing reached values lower than the respective grain sizes inside the lamellae, a further lamella thinning occurred causing a significant hardness increase of the composite. At lamella spacings below 50 nm deformation started to localize in 150-300 nm broad shear bands, which surprisingly exhibited no softening. Instead, the steady formation of new shear bands aided to transform the lamellar structure into a nanocrystalline equi-axed microstructure and additionally rotated the lamellar matrix towards the shear plane. This process led to an additional refinement of the alloy and a hardness increase until a constant hardness level was obtained. Combined analyses by synchrotron X-ray and transmission electron microscopy measurements revealed that, after reaching the saturation microhardness level, mechanical mixing of Cu and Ag occurred in the shear bands, which can be attributed to the enormous strains accommodated in the shear bands. Due to the localized deformation by shear bands, structural and chemical homogenization of the alloy was not achieved even at very high applied strains. The final microstructure was composed of nanocrystalline single-phase supersaturated regions embedded in a residual nano-lamellar matrix.

III.1 Introduction

Nanocrystalline composites are a promising class of materials for technical applications because of their high structural and thermal stability compared to single-phase materials. For instance, the copper based metal matrix composites used as conductors for pulsed high field magnets [1–4] require high thermal and electrical conductivity with simultaneous high strength. These superior characteristics are attained with the introduction of phase boundaries. Extraordinary mechanical and physical properties of Cu-Ag composites were first reported in vapor-quenched [5] and wire drawn alloys [6]. The developments in wire drawn Cu-based alloys have shown an extreme increase in tensile strength [2,4,7].

Several efforts were made in the past years to understand how interface structure and phase spacing influence the mechanical properties [8–10]. The extensive studies on layered fcc-bcc

Cu-Nb composites showed that the fundamental nature of deformation mechanism changes with decreasing layer thickness. For layer thicknesses larger than 100 nm conventional dislocation pile-up model could explain the observed Hall-Petch strengthening; however, at layer thicknesses of few tens of nanometer confined layer slip becomes important. Further reduction in layer thickness to several nanometers promote the dislocations to cross the interfaces, leading to strong strain localization [11]. Besides the phase spacing the characteristics of the interfaces can also influence the mechanical properties [8,12]. Finite element simulations have shown that the interface structure and associated texture evolution can affect the deformation mechanisms, in particular the formation of shear bands [13–15], which is a common feature in severe plastic deformation (SPD) processed Cu-Ag alloys [16,17].

Another interesting aspect of immiscible material systems like Cu-Ag is the formation of supersaturated solid solutions and amorphization during severe plastic deformation. Early studies on the ball milling of Cu-Ag system have shown that supersaturated solid solutions can be obtained over the whole composition range [18]. Although, several hypothesis were proposed to explain the mechanism of supersaturation and amorphization [15-20], due to the undefined applied strain a direct correlation between deformation-induced changes and the material state remained unclear [19]. In order to overcome this constraint other SPD processes like accumulative roll bonding and high pressure torsion (HPT) have been used in recent years [17,20–23]. The HPT technique is especially attractive due to the possibilities of better controlled processing parameters tunable in a wide range of temperature, pressure, strain rate and applied strains.

The HPT deformation of cast Cu-Ag alloys have shown that the starting microstructure can strongly influence the deformation behavior. For inhomogeneous cast structures, which are composed of single phase Cu- or Ag-rich regions and eutectic phases, deformation leads to inhomogeneous evolution of the microstructure and a strain hardening behavior different from that of single-phase alloys [16]. In contrast to the cast microstructures, HPT deformation of Cu and Ag powders provides more homogeneous initial microstructures over the complete range of composition [24].

In the present study we address these issues by HPT deformation of Cu-37at%Ag elemental powders. The initially micrometer-sized particles facilitated investigations on the deformation processes over a wide range of structural length scales. Samples deformed to different strain levels were used to study fundamental deformation mechanisms and their corresponding influence on the microstructure and mechanical properties.

III.2 Experimental

The commercially pure powders of Cu and Ag (99.97%, 625 mesh and 99.99%, 500 mesh, from Alfa Aesar), with a particle size of about 20 to 50 μm, were mixed to obtain a Cu-37at%Ag composition. The powders were filled directly into the steel anvils and consolidated in the HPT tool. The HPT processing was performed with an applied pressure of 7.5 GPa and a rotational speed between 0.2 and 0.6 rotations/min at room temperature (RT). Samples were deformed between 1 and 100 rotations, the corresponding applied shear strain γ is calculated with

$$\gamma = \frac{2\pi r}{t} n, \qquad \text{(III.1)}$$

where r is the radius, t the thickness of the disk and n is the number of rotations. The resulting disks were 8 mm in diameter with a thickness between 0.45 and 0.6 mm. Detailed information on the HPT process used in this study can be found elsewhere [25]. During HPT processing the specimen and the anvils were cooled with compressed air to avoid heating of the sample. Due to uncertainties in the sample preparation process of samples (exact radius and exact thickness of the sample of the investigated area), for the calculated shear strains only approximate values can be given.

Microstructural investigations were performed with a Zeiss Leo 1525 scanning electron microscope (SEM), a Philips CM12 operated with 120kV and an image-side C_S-corrected JEOL JEM-2100F operated with 200 kV transmission electron microscopes (TEM). The SEM samples were prepared by conventional polishing with diamond paste and colloidal silica and a final polishing with Buehler Vibromet. The TEM samples were prepared by standard dimple grinding with subsequent ion milling. Special care was taken to avoid any heating of the sample during preparation.

The local deformation processes were analyzed with a split HPT disk as shown in Figure 1 [26]. The HPT disks, previously deformed to 5, 10, 50 and 100 rotations, were cut at a radius of about 2 mm as indicated in Figure 1a (which corresponds to applied shear strains of γ~18, 125, 250, 1250 and 2500, respectively). The cross-section surface was polished and 100 × 100 µm grids were engraved into the polished surface by focused ion beam (FIB) technique (see Figure 1b). At least three grids were made across the thickness of each disk. After FIB cutting, a matching counterpart of an HPT disk made of pure Cu was put together with the sample into the HPT tool and further deformed for 5 or 15°, corresponding to applied shear strains of γ~0.33 or 1, respectively (see Figure 1c). Before and after these additional HPT deformation steps the displacement of the FIB markers was analyzed with SEM.

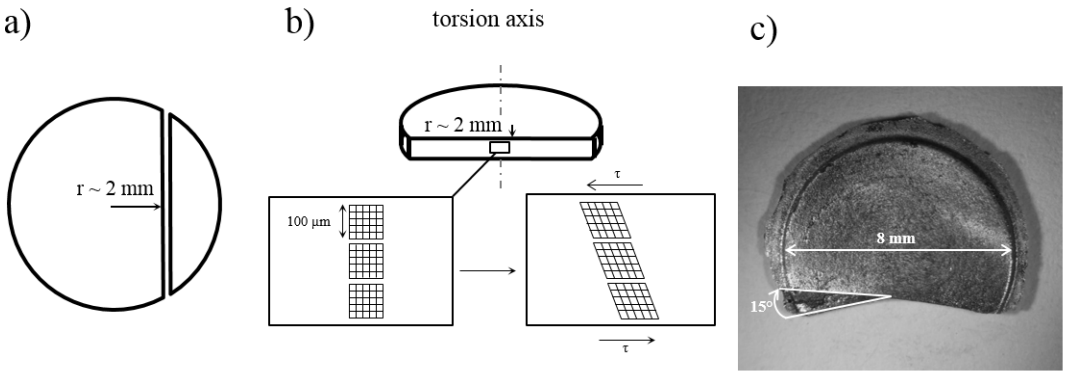

Figure III.1: Schematic of the experimental procedure for split samples: a) the HPT disk is cut at a radius of ~2 mm. b) cutting of FIB markers in the polished cross-section of the HPT disk. c) HPT disk deformed to an additional rotation of 15° (γ~1).

Synchrotron X-ray diffraction (XRD) experiments were performed at the PETRA III P07 beamline at the DESY Photon Science facility (Hamburg). The diffraction measurement was conducted on samples deformed to γ~190, 380, 1900 and 3800 using a beam energy of 111 keV. The primary and secondary slit of 0.5 × 0.5 mm^2 and 0.7 × 0.7 mm^2, respectively were used to improve the microstructure statistics. The measured transmission diffraction patterns were analyzed with FIT 2D software [27]. A single peak analysis of 111 peaks of Cu,

Ag and the supersaturated phase [28] was performed for estimation of coherent domain size and root mean square (RMS) strain. The diffraction pattern of CeO_2 (NIST standard reference 674b) was used as reference for instrumental broadening.

Vickers hardness measurements were performed with a Buehler Micromet 5100 using a maximum load of 500 gf along the cross section of the HPT disk in distances of 250 µm each. Local mechanical properties at room and elevated temperatures were investigated by nanoindentation testing carried out with a platform Nanoindenter G200 (Keysight Tec). All indentations were performed with three-sided Berkovich pyramids (for room temperature testing: diamond; for high temperature testing: sapphire), tip shape and frame stiffness calibrations were performed with Fused Silica in a regular period of time according to the Oliver Pharr method [29]. Further, a continuous stiffness measurement unit (CSM) was used to collect depth dependent mechanical data (hardness and modulus), by measuring the contact stiffness continuously over indentation depth by superimposing a sinusoidal load signal (standard parameter: 45 Hz, 2 nm oscillation amplitude). Tests were performed in load controlled mode (max. load: 1 mN; Loading Time: 5 s) for small scale mechanical properties mapping as well as in constant strain-rate mode (max. indentation depth: 2500 nm; standard indentation strain-rate: 0.05 s^{-1}) for bulk properties of the different regions. Hardness and Young's Modulus (poisson ratio 0.32) were calculated according to Oliver-Pharr without considering pile-up influences. A significant influence of an indentation size effect can be excluded due to the nanocrystalline microstructure. In addition and for a further understanding of the contributing thermally activated deformation processes, nanoindentation strain rate jump test under ambient conditions (23-28 °C room temperature) [30] and at elevated temperatures (100 – 300 °C) [31] were performed on a set of selected samples. High temperature (HT) testing was realized by a Surface Tec (Hückelhoven, Germany) laser heating unit, which allows the individual heating control of tip and sample. In the case of HT testing, strain rate jump tests were performed at several temperatures during heating to capture any effect on the deformation behavior due to the annealing. Abrupt strain rate changes were applied every 500 nm indentation depth in a repetitive manner between 0.05, 0.005 and 0.001 s^{-1} for RT and between 0.05, 0.01 and 0.005 s^{-1} for HT testing.

III.3 Results

III.3.1 Microstructural and hardness evolution

A comparison of the Vickers hardness evolution with applied strain, Figure 2, showed a strong hardness increase in the Cu-37at%Ag (Cu37Ag) composite, compared to pure Cu (powder and bulk oxygen-free high-conductivity (OFHC) Cu) and pure Ag (powder). The hardness of samples deformed to 7, 20, 50 and 100 rotations were measured in order to cover a wide range of applied strains. As the powders were directly compacted in the HPT tool, it required an applied strain of about γ~10 to fully bond the particles together. The hardness profile reflected the general characteristic of immiscible composite material systems [23,24]. Three distinct stages in the hardening behavior can be clearly distinguished for γ>10. Between γ~10 and 100 the hardness increased slightly from about ~160 HV to ~210 HV. This was followed by a strong hardness increase up to γ~500. At γ~500 the hardness saturated to a maximum hardness level of ~342 HV. The bulk Cu had a significant lower saturation hardness (~150 HV) compared to the consolidated Cu powder (~230 HV). Pure Ag showed a saturation hardness of ~110 HV without any significant difference in the hardening behavior between powder and bulk material.

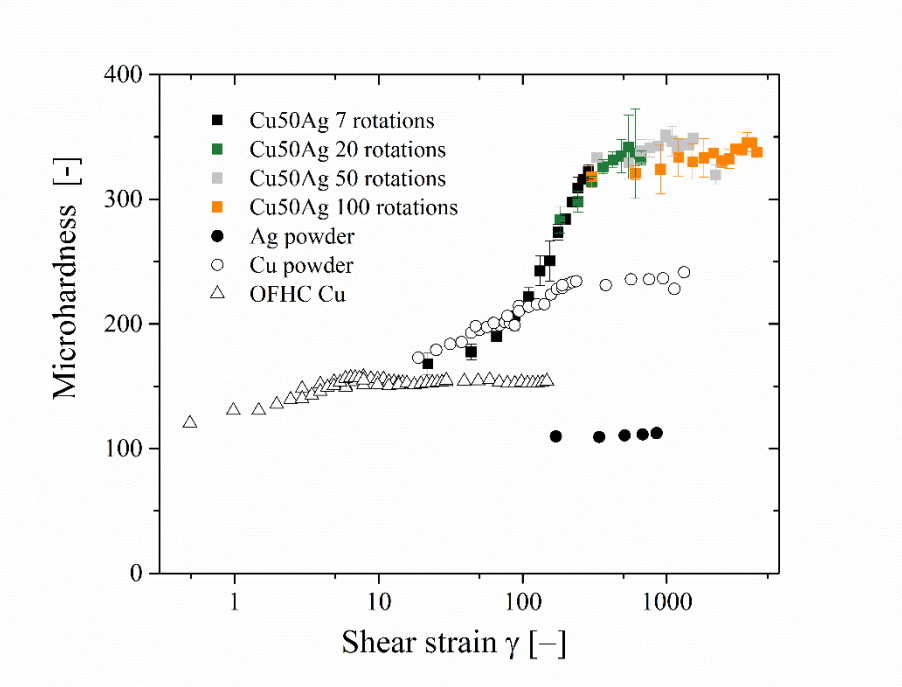

Figure III.2: Vickers hardness evolution with applied strain for pure Cu (powder and OFHC bulk material), pure Ag powder and Cu37Ag composite. For the Cu37Ag composite 4 samples deformed to 7, 20, 50 and 100 rotations are included in the analysis.

In the following section the microstructural evolution in the different hardness regimes are described sequentially. After one rotation (γ~18 at a radius of 2 mm) a lamellar structure evolved (Figure 3a) with alternating Cu and Ag bands, appearing in dark and bright contrast, respectively. A mean lamella thickness of 740 nm was estimated from a line interception method, however, the lamella thickness distribution is very broad ranging from well below 100 nm to several micrometer. This is a result of the broad initial particle size distribution, possible particle clustering and the imperfect distribution of Cu and Ag particles after the powder mixing process, causing that strong structural inhomogeneities were present at the beginning. Inside the Cu and Ag lamellae an ultrafine-grained (UFG) structure was formed. As noted in a previous study [24], Ag reaches the saturation hardness and microstructure at much lower applied strains than Cu. When the shear strain was increased further, the separate Cu and Ag lamellae were continously thinned and at strain of γ~190, both, also Cu reached the corresponding saturation hardness and UFG microstructure of the bulk material, with sizes between 200 and 300 nm. At this hardness level first shear bands, oriented at ~30° to the horizontal shear plane, appeared in fine-lamellar regions (Figure 3b), while micrometer-sized Cu and Ag lamellae were still present at other regions (top and bottom area of the image in Figure 3b). At higher applied strains (γ~380) the number of shear bands increased (Figure 3c). However, the measured shear band angles tend to decrease with increased shear strain (from ~30° measured at the very first shear bands to below 15° measured at γ~380). Thus the shear bands caused a rotation of the lamellae compared to the parallel alignment at lower applied strains (compare Figure 3a and c).

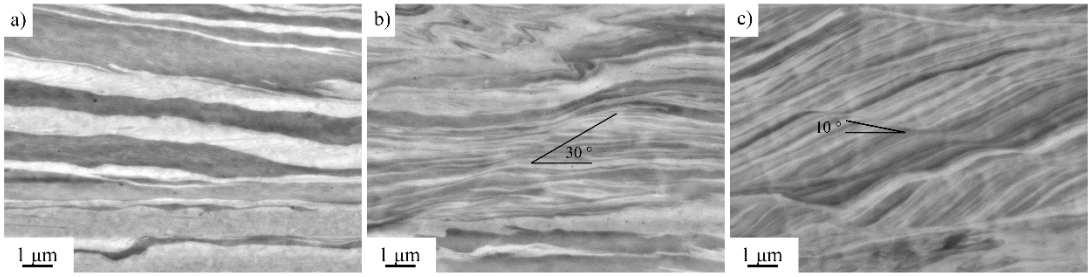

Figure III.3: SEM images using back-scatter electrons in radial direction for different applied strains, Cu appears dark and Ag bright. a) For γ~18 showing alternating Cu and Ag lamellae with spacing ranging from 100 nm to about 1 µm. b) At γ~190 the first shear bands are observed under angles of ~30°. c) At γ~380 numerous shear bands run through the lamellar regions at angles of ~ 10° inducing a rotation of the lamellae orientation.

Further insights are provided by TEM: at a strain of γ~190 banded regions were observed with a wide range of lamella spacings between 100 nm (see scanning TEM (STEM) bright-field (BF) image in Figure 4a) to few micrometers (see SEM in Figure 3b). Moreover, larger orientation changes were observed along longitudinal section of thinner lamellas (see contrast changes in Figure 4a) while in the transverse section the lamellae substructures were only observed for lamella spacings larger than 50 nm. It must be noted, that the SEM images yield larger lamellae spacings than the spacing revealed by TEM (compare Figure 3b and Figure 4a) due to the limited resolution of the SEM. At a strain of γ~380 numerous shear bands occurred, one example is shown in the micrograph in Figure 4b. The shear band is about 300 nm wide and runs through the nano-lamellar/UFG matrix. In STEM BF no distinct grain structure could be identified in the shear band, only small contrast variations indicate the very small grain size. The STEM high-angle annular dark-field (HAADF) imaging combined with EDX measurements revealed chemical variations in the shear band (see Figure 4c). With increasing applied strain the number of shear bands increased, as seen in Figure 4d, γ~1900 and Figure 4e, γ~3800. The shear bands showed no intense broadening and no apparent changes in their microstructure. The lamellar regions continue to refine and chemical variations strongly decrease as found by EDX line scans in Figure 4f. In Figure 5a, at γ~3800, two regions can be distinguished, a dual-phase lamellar in the upper part of the image and a shear band in the lower part. The corresponding selected area diffraction (SAD) patterns (Figure 5b, the areas contributing to the diffraction patterns are roughly marked by circles) were analyzed using the profile analysis of SAD (PASAD) plug-in for Digital Micrograph [32]. The azimuthal integration given in Figure 5c shows clear differences between the lamellar region, where fcc rings from Cu and Ag were present, and the shear band region, where only one set of fcc rings was observed, implying the formation of a single-phase supersaturated solid solution. In both, single- and dual-phase regions, the grain structure is extremely refined and textured, with non-uniform intensities along the diffraction rings.

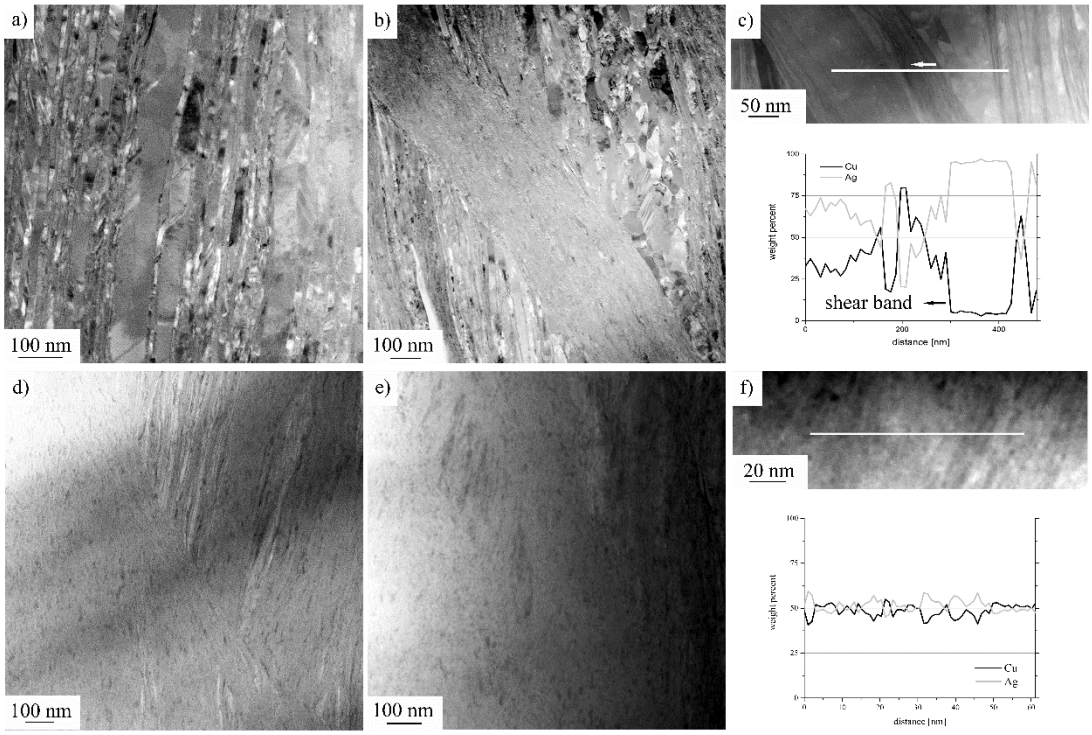

Figure III.4: STEM bright field micrographs in radial direction for different applied strains. a) Fine-lamellar region with lamella thickness down to below 10 nm at γ~190. b) A shear band running through the lamellar/UFG matrix at γ~380, c) with EDX line scan indicated in the high-angle annular dark field STEM. Microstructure deformed to d) γ~1900 and e) γ~3800 showing an increase in regions deformed by shear bands. f) EDX line scan at γ~3800 showing a chemical homogenization of the alloy.

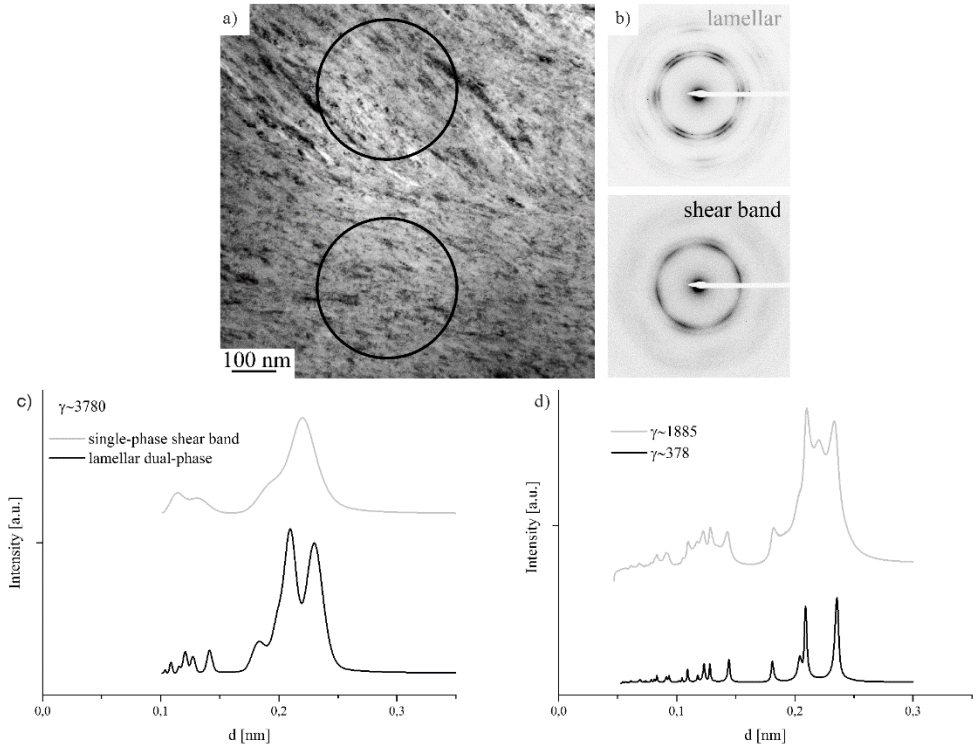

Figure III.5: a) TEM bright field image at γ~3800 with a lamellar region in the upper half of the image and a region deformed by a shear band in the lower part of the image. b) Corresponding selected area electron diffraction (SAD) patterns (the areas contributing to the SAD patterns are indicated by circles in a)) for the lamellar and the shear band region. c) Azimuthal distribution of SAD patterns of b) showing diffraction rings of Cu and Ag in the lamellar regions and a single-phase diffraction pattern for the shear band region; d) synchrotron X-ray measurements for γ~380 and γ~1900 showing the occurrence of a third phase in the diffraction pattern at γ~1900.

The presence of this supersaturated phase was also confirmed by synchrotron XRD measurements, see Figure 5d. Table 1 lists the lattice parameters, coherent domain sizes and inhomogenous RMS strains calculated from single peak analysis, which was performed on samples deformed to 5, 10, 50, and 100 rotations, corresponding to applied strains of γ~190, 380, 1900 and 3800, respectively. The lattice parameters of Cu and Ag changed after 50 rotations, indicating the incorporation of Ag and Cu atoms, respectively. Additionally the supersaturated phase appeared, with a lattice parameter of ~0.38 nm corresponding to 66 at% Ag. The coherent domain sizes of Cu and Ag reduced continuously with increased applied strain, consistent with SEM and TEM investigations, while the RMS strain, which represents the amount of defects in the lattice, became significant after 50 rotations (γ~1900). Once the supersaturated phase was formed, it showed no significant increase in coherent domain size and the RMS strain was significantly larger than for Cu and Ag. It is interesting to note that the RMS strain of the supersaturated phase reduced with increasing deformation at 100 rotations (γ~3800).

Table III.1: Results of synchrotron X-ray measurements showing the atomic percent of Cu calculated from lattice parameters, coherent domain sizes and root mean square strains for Cu, Ag and the supersaturated phase (ss-phase) of samples deformed to 5, 10, 50 and 100 rotations, corresponding to applied strains of γ~188, 378, 1885 and 3780, respectively. Numbers in parentheses represent the errors.

Sample	Shear strain	Atomic percent of Cu			Coherent domain size, L (Å)			Root mean square strain, $<\varepsilon^2>^{1/2}$ (10^{-3})		
		Ag	SS phase	Cu	L_{Ag}	$L_{SS\ phase}$	L_{Cu}	$<\varepsilon^2>_{Ag}^{1/2}$	$<\varepsilon^2>_{ss\ phase}^{1/2}$	$<\varepsilon^2>_{Cu}^{1/2}$
5 rotations	190	0		100	23,8 (8,2)	-	31,1 (14,7)	1.6 (4.0)	-	0.6 (9)
10 rotations	380	0		100	14,9 (3,2)	-	28,9 (12,7)	-		1.8 (3.0)
50 rotations	1900	7,8	66	95	4,6 (0,3)	3,4 (0,2)	8,5 (1,1)	6.2 (1.0)	23 (0.2)	5.8 (1.0)
100 rotations	3800	6,8	62	94	4,1 (0,2)	4,2 (0,3)	11,2 (1,9)	7.2 (0.8)	17 (0.3)	8.9 (0.7)

III.3.2 Local deformation behavior

At applied shear strains of γ~125 (Figure 6a), deviations from ideal shear deformation were observed, revealed by many steps in the inclined FIB grid. Detailed imaging of the markers (Figure 6b) showed that the deformation was more homogenous in regions with a very fine lamellar structure. In other regions, with coarse Cu and Ag lamellae (width of >1μm), strong localized deformation was observed. At γ~250, although the hardness has not reached the saturation level (see hardness plot in Figure 2), many shear bands were observed, as can be seen on the FIB grid in Figure 6c. Two shear bands, which contributed strongly to the accommodation of the applied shear strain, are marked with arrows. Between shear bands the FIB lines are vertical, indicating that the material remained nearly undeformed (Figure 6d). These micrographs suggest that not all shear bands were operating simultaneously (one inactive shear band is indicated by an arrow in Figure 6d). Additionally, besides the shear bands, there were also regions, which deformed by uniform shear, shown by the uniform inclination of the FIB markers in Figure 6e. At higher applied strains (γ~1250), when the hardness plateau was reached, the whole sample was refined by shear bands. In Figure 6f and 6g two FIB grids are presented exemplarily. A combination of shear bands and homogenous deformation was observed in a fine lamellar microstructure in Figure 6f. The FIB markers were inclined at different angles suggesting variations in the amount of accommodated strain for different regions. In contrast to Figure 6f, the FIB grid in Figure 6g showed a region, which deformed mainly by shear bands. As indicated by arrows the grid was displaced at three positions, where shear bands seem to concentrate. The area in between these bundles remained undeformed, which can be seen on the vertical position of the FIB lines. At a shear strain of γ~2500, very few regions deformed by uniform shear are visible indicating that shear banding is the dominant deformation mechanism (see Figure 6h).

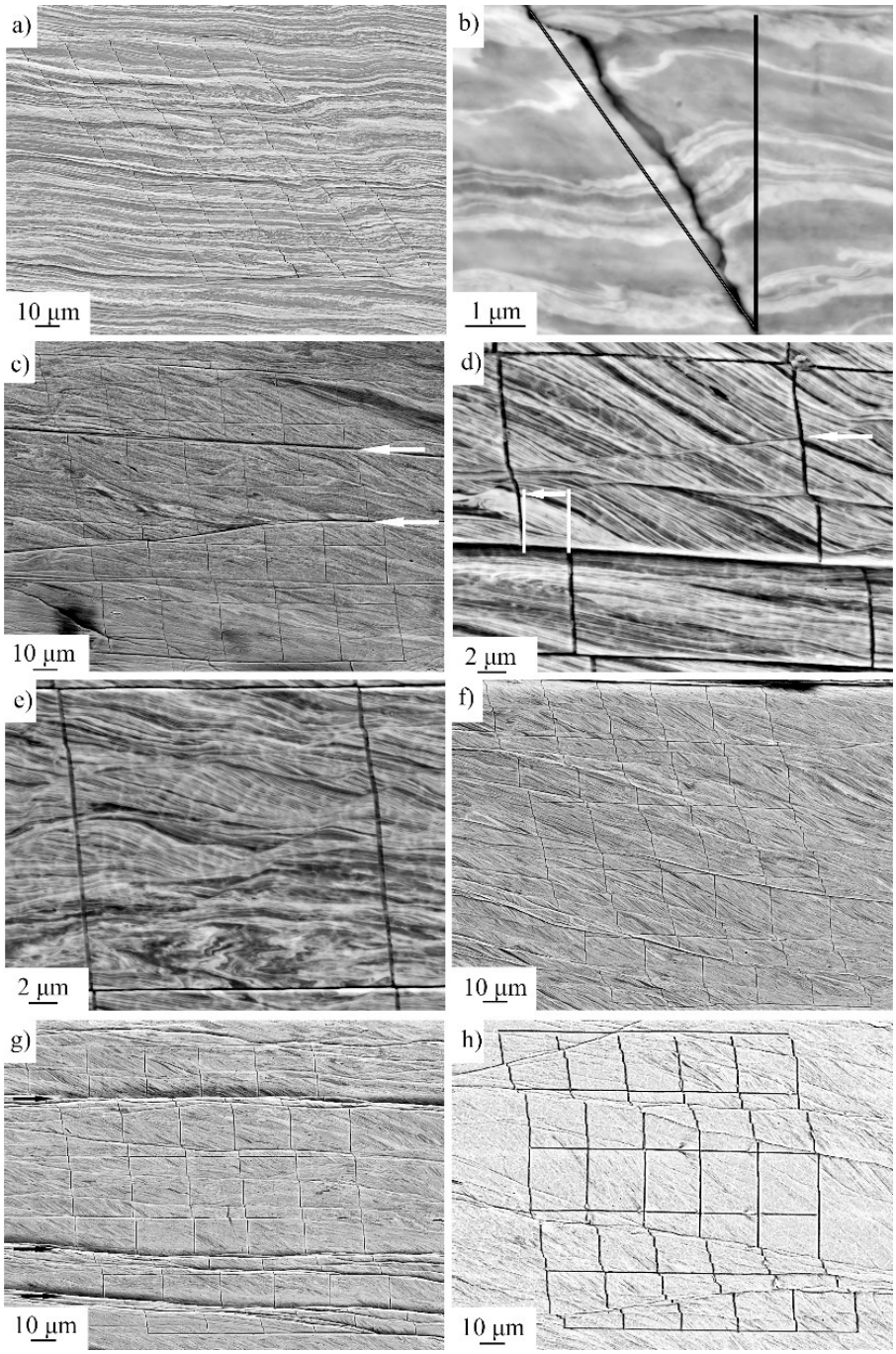

Figure III.6: SEM images using back-scatter electrons of the split samples. a) γ~125+1, the FIB grid is in general uniformly sheared, but local variations are seen. b) Detail of a) revealing regions that sheared uniformly and strong local deformation of broader retained Cu and Ag lamellae. c) γ~250+0.35 with several shear bands shifting the FIB grid. d) detail of c) showing a shear band, which displaced the FIB grid of about 2 µm and an inactive shear band marked by an arrow. d) detail of uniformly sheared regions of c). f) γ~1250+1, showing a combination of shear bands and uniform shear of the grid. g) γ~1250+1, the grid is displaced mainly at three positions by shear bands (marked with arrows). h) γ~2500+1, the deformation is mainly carried by shear bands.

III.3.3 Nanoindentation experiments

As the single-phase regions in samples deformed to 100 rotations (γ~3800) were too small to probe with nanoindentation, a sample deformed to extremely high strains (300 rotations or γ~11300), which showed large single- and dual-phase regions, was chosen. Several nanoindentation maps (one RT example is shown in Figure 7a) and strain rate jump tests were performed at RT, 70, 100, 150 and 200°C. At RT the hardness difference between single-phase and dual-phase regions was very small, measurements at elevated temperatures showed that exceeding 70°C the hardness drops continuously, see Figure 7b (mean values of minimum 4 measurements). It must be noted that phase decomposition starts at 100°C, but grain growth not until 250°C, which was confirmed by TEM investigations with *in-situ* and *ex-situ* annealing experiments. The decrease in hardness is somewhat stronger in the dual-phase regions than in the single-phase regions. Strain rate jump tests revealed a small strain rate sensitivity, but no pronounced difference between single- and dual-phase regions was observed, see hardness data in Figure 7c (the Young´s modulus is shown in the inset).

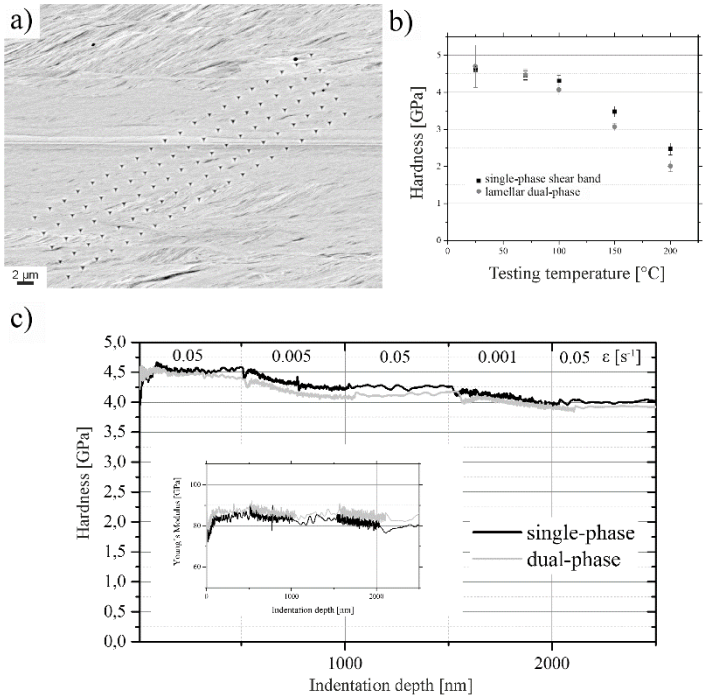

Figure III.7: Nanoindentation measurements for single-phase and dual-phase regions. a) Nanoindentation hardness at different temperatures. Strain-rate jump tests at room temperature, c) Hardness, strain rates are indicated, and Young´s modulus as inset.

III.4 Discussion

In pure metals and single-phase alloys HPT deformation leads to a microstructural refinement accompanied by intense hardening until an equilibrium of fragmentation and restoration processes is reached, which is typically between γ~10-30, accompanied with a constant hardness in this regime [33]. However, in immiscible material systems, as in the present study, a more complex fragmentation and hardening behavior is observed. By studying the microstructural changes, the hardness evolution can be divided in four regimes, as indicated

schematically in Figure 8 (labeled A to D). In the following section the different hardness regimes are discussed concerning their prevailing deformation mechanisms during HPT processing.

III.4.1 Deformation at strains γ<190 (regime A and B)

In the first stage of hardening, labeled as regime A in Figure 8, a simultaneous thinning of the lamellae and a grain refinement inside the Cu and Ag lamellae occurred. Due to the fragmentation and distribution of the natural oxide layer of the Cu powder, which leads to stabilization of a finer grain structure [34], the Cu powder showed more pronounced hardening compared to bulk high purity bulk Cu, as seen in the hardness plot in Figure 2. The oxide layer caused a delay of saturation in grain size and in hardness as well. The Ag powder instead reached a steady state at strains of γ~10, implying that as soon as the powder particles were sufficiently bonded together to obtain a dense sample, the Ag phase had reached the saturation grain size, independent of lamella spacing (see also EBSD data in Reference [24]). Thus, in the first stage of hardening, Ag showed no change in grain size, while Cu continued to refine, causing a hardness increase up to an applied strain of γ~100. The basic mechanisms leading to the saturation grain structure were similar as in pure metals, namely the formation of dislocation cells and cell blocks, which gradually transform into an UFG structure [33]. In lamellae, which already reached the saturation microstructure (complete Ag phase and part of Cu phase), the grain size is maintained by grain boundary mediated mechanisms [35].

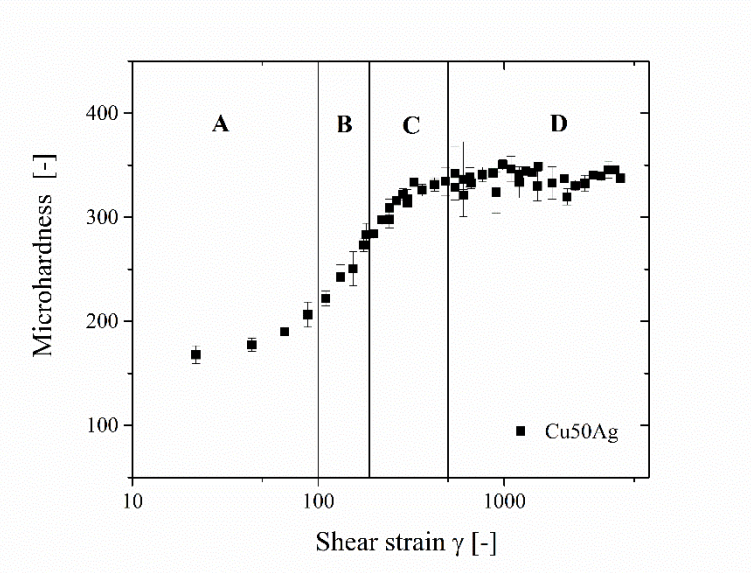

Figure III.8: Stages in the hardening of the Cu37Ag composite. A: formation and saturation of an UFG structure in the separate Cu and Ag lamellae, B: Cu and Ag lamellae have reached thicknesses in the range of their respective saturation grain sizes, further co-deformation of Cu and Ag lamellae referred to as dual-phase refinement. C: occurrence of shear bands causing further dual-phase refinement and a rotation of the lamellae. D: localized saturation: deformation is mainly limited to shear bands, in which a single-phase supersaturated solid solution is formed.

The split samples, see Figure 6a and b, showed that larger residual lamellae deformed stronger compared to fine-lamellar regions, leading to a homogenization of the structural sizes. At a strain of γ~100 the lamella spacing in some regions reduced below the respective

saturation grain size of the Cu and Ag phases (which is about 150 to 250 nm), with only one grain across the width of the lamella (see STEM image in Figure 4a). Then further uniform reduction of Cu and Ag phase spacing, referred to as dual-phase refinement (regime B in Figure 8), occurred. Simultaneously Cu reached the saturation grain size. This refinement led to further increase in hardness until a critical phase spacing is reached and shear localization set in.

III.4.2 Deformation at strains γ>190 (regime C and D)

At applied shear strains of γ~190 the first shear bands were observed, marking the beginning of regime C (see Figure 8), which ends with reaching the saturation hardness regime D at γ~500. As shown in split samples in Figure 6d to h, the deformation is realized by a combination of uniform shear of the lamellae and localized shear bands from γ~190 up to γ~1250. The characteristics of the shear bands formed in regime C and D will be discussed regarding their impact on microstructural changes and their contribution to the accommodation of the imposed shear strain.

III.4.2.1 Shear bands in regime C

Extensive studies in the past have shown that shear band formation is primarily dictated by very low hardening rates or lamellar structures, such as heavily twinned alloys or lamellar dual-phase composites [36–42]. Detailed investigations on Cu-Al [37,40] and α-brass [43] have shown that local lattice bending and/or necking of twin lamellae can provide necessary inhomogeneities which act as precursors to the shear bands. On the other hand Jia et al. [44] suggested that the presence of wide grain size distributions can facilitate deformation localization in larger grains and thus initiate shear bands to accommodate the macroscopic strains. For the Cu37Ag powder composite, an inhomogeneous microstructure was present from the beginning (Figure 3b) due to the broad particle size distribution and particle clusters and shear bands were observed to initiate only at thinner lamellae, see Figure 3b.

At a certain point new sets of shear bands are nucleated to accommodate the imposed strain, this caused the lamellae to rotate out of the HPT shear plane with increasing strain. Nanoindentation measurements (see Figure 7) showed that the hardness difference between single-phase shear band regions and remaining lamellar regions is very small. Because the shear band structure shows no changes with increasing applied strain, it can be assumed that the hardness in the shear bands formed in regime C have the same hardness as the shear bands in regime D. A hardening in the shear bands was suggested by Blicharski et al. in austenitic steel [41], and could explain why shear bands stop to operate (see Figure 6e) and additionally promote the continuous formation of new shear bands in regime C, when the surrounding matrix material is still nano-lamellar or UFG (see Figure 4b). Thus the density of shear bands increases with subsequent deformation. Additionally, the lamella spacing decreases with increase in strain, as seen in micrographs, and also the coherent domain size of Cu and Ag reduced continuously; however, the RMS strain did not show any significant change. Thus, the accumulated deformation was also accommodated by thinning of lamellae. The steady formation of shear bands and the consequent rotation of lamellae blocks to an inclined angle together with further co-deformation of lamellar regions maintained the applied strain. The continuous transformation of lamellar regions into a nanocrystalline microstructure and additionally a further refinement of the lamellae leads to a strong hardening from ~230 HV at γ~190 to the maximum of ~342 HV in the hardness saturation regime. The development of a shear band network leading to lamella rotation accelerates the refinement of the microstructure. Moreover, the structural inhomogeneities leveled out with increasing strain, because coarser lamellae deform stronger compared to thinner lamellae. At an applied strain of about 500 the

hardness saturation regime was reached (equivalent to regime D in Figure 8). The structure at this point is composed of many lamella blocks inclined to the HPT shear plane, separated by shear bands with a nanocrystalline microstructure. Larger retained lamellae are not present anymore.

III.4.2.2 Shear bands in regime D

At γ>1000, the hardness value is saturated and a supersaturated phase appeared. The XRD measurements at γ~1900 showed very fine coherent domain size and large RMS strain, suggesting massive accumulation of defects. Interestingly, the RMS strain of the supersaturated phase was much larger than the one of the Cu and Ag lamellae. Moreover, the chemical mixing was observed in both Cu (~5 at% Ag) and Ag (~7 at% Cu) (see table 1). With increasing applied strain a reduction in shear band angle from 30° to 10° was observed (see Figure 3 and 6). So in regime D a limited number of shear bands were running nearly parallel to the macro shear plane of the HPT deformation (Figure 6h and i), and accommodated most of the imposed shear strain. In these shear bands enormous shear strains were realized, in single shear bands they can exceed levels of γ>10 at global applied strains of γ<1. Taking for example the shear band in Figure 6e, which caused a shift of the FIB marker by 3.3 µm, and taking a shear band thickness of 300 nm (as seen in TEM images in Figure 4), the calculated shear strain γ is about 11 (at a global applied strain of 0.35). Hence 30 nm grains or lamellae would refine to below 3 nm in this shear band (according to $d = \frac{d_0}{\gamma}$ [45]). This led to massive chemical mixing and the formation of a single-phase supersaturated solid solution inside the shear bands. Surprisingly, the global composition is attained in the new supersaturated solid solution, which showed a corresponding lattice parameter of ~0.38 nm. At very high strains the grain size of the lamellar matrix approaches the grain size of the shear band (see Figure 5a and table 1). Very similar hardness levels of these different microstructural states caused a simultaneous deformation by shear bands and uniform shear of lamellar regions. Thus mechanical mixing occurred in the shear bands, where extremely high strains are accommodated, but in addition also in lamellar regions, when the phase spacing reached a critical limit of 5 nm and less (see table 1, ~7at% Cu in Ag and ~6at% Ag in Cu are solved as calculated by Vegard´s law).

The question of a possible temperature rise in operating shear bands is still under debate [46,47]. Nanoindentation measurements of the Cu37Ag composite at different temperatures, Fig. 7b, have shown that at elevated temperatures the lamellar dual-phase regions have a lower hardness than the single-phase regions. Thus a temperature rise in the shear bands does not cause a softening in the shear bands compared to the nearby matrix. Additionally, a temperature rise during processing cannot exceed 70°C, because the hardness of the single- and dual-phase regions show no difference below this value; otherwise the deformation would preferentially take place in dual-phase regions only.

The very small differences in hardness and strain rate sensitivity together with the parallel orientation of the shear bands to the HPT shear plane led to a retardation of deformation in the lamellar regions by shear bands. In addition also an effect of a temperature rise was excluded, which could promote a transformation of retained lamellar regions. Therefore it seems that extremely high applied strains would be needed to reach a homogenous single-phase supersaturated solid solution.

III.5 Summary and conclusion

A Cu37Ag composite was produced by powder compaction and HPT processing to a wide range of applied strains. The evolving microstructures were linked with changes in the hardness and the local deformation behavior. The following conclusions can be drawn:

i) At applied shear strains below $\gamma \sim 100$ a lamellar composite is formed. In the separate Cu and Ag phases an UFG structure evolves by similar mechanisms as in severely plastically deformed pure metals. The grain refinement leads to an increase in hardness as in pure metals.

ii) The lamella spacing reduces to the saturation grain size of pure Cu and Ag at $\gamma \sim 100$. Further thinning of them induces a strong increase in hardness. The microstructure is refined by uniform co-deformation of the Cu and Ag lamellae up to applied strains of $\gamma \sim 190$.

iii) At $\gamma \sim 190$ shear band formation starts. The localized shear inclined to the lamella orientation in the shear bands leads to a strong refinement to a nanocrystalline dual-phase structure. New shear bands are formed continuously to accommodate the applied strain, thereby causing a rotation of the lamellae. With ongoing deformation a large volume fraction is deformed by shear bands resulting in an increase in hardness until saturation is reached. A complex balance between shear banding and co-deformation of Cu and Ag lamellae leads to an enormous refinement.

iv) At $\gamma \sim 3800$ the major part of deformation is carried by shear bands running nearly parallel to the HPT shear plane, and slow down the homogenization process of the material. These shear bands in the hardness saturation regime accommodate very high strains, leading to substantial mixing of Cu and Ag in the shear bands. The newly formed single-phase supersaturated solid solution maintains the global composition.

v) The final obtained microstructure at room temperature is composed of supersaturated single- and lamellar Cu-Ag dual-phase regions.

Acknowledgement

Funding of this work has been provided by the European Research Council under ERC Grant Agreement No. 340185 USMS and by the Austrian Science Fund in the framework of research project P24429-N20. Further financial support by the Austrian Federal Government (837900) (in particular from the Bundesministerium für Verkehr, Innovation und Technologie and the Bundesministerium für Wirtschaft, Familie und Jugend) represented by Österreichische Forschungsförderungsgesellschaft mbH and the Styrian and the Tyrolean Provincial Government, represented by Steirische Wirtschaftsförderungsgesellschaft mbH and Standortagentur Tirol, within the framework of the COMET Funding Programme, is appreciated. The measurements leading to these results have been performed at the Test Beam Facility at DESY Hamburg (Germany), a member of the Helmholtz Association (HGF). We gratefully acknowledge the assistance by Dr. Torben Fischer.

References

[1] J. Freudenberger, N. Kozlova, A. Gaganov, L. Schultz, H. Witte, H. Jones, Magnetoresistance up to 50 T of highly strengthened Cu – Ag conductors for pulsed high field magnets, Cryogenics 46 (2006) 724–729.

[2] A. Gaganov, J. Freudenberger, W. Grünberger, L. Schultz, Microstructural evolution and its effect on the mechanical properties of Cu – Ag microcomposites, Z. Met. 95 (2004) 425–432.

[3] W. Grünberger, M. Heilmaier, L. Schultz, Development of high-strength and high-conductivity conductor materials for pulsed high-field magnets at Dresden, Phys. B 294-295 (2001) 643–647.

[4] K. Han, J.D. Embury, J.R. Sims, L.J. Campbell, H.-J. Schneider-Muntau, V.I. Pantsyrnyi, A. Shikov, A. Nikulin, A. Vorobieva, The fabrication, properties and microstructure of Cu – Ag and Cu – Nb composite conductors, Mater. Sci. Eng. A267 (1999) 99 – 114.

[5] S. Mader, A.S. Nowick, H. Widmer, Metastable evaporated thin films of Cu-Ag and Co-Au alloys-I Occurence and morphology of phases, Acta Metall. 15 (1967) 203–214.

[6] G. Frommeyer, G. Wassermann, Microstructure and anomalous mechanical properties of *in situ*-produced silver-copper composite wires, Acta Metall. 23 (1975) 1353–1360.

[7] K. Han, J.D. Embury, J.J. Petrovic, G.C. Weatherly, Microstructural aspects of Cu-Ag produced by the Taylor wire method, Acta Mater. 46 (1998) 4691–4699.

[8] N.A. Mara, I.J. Beyerlein, Review: effect of bimetal interface structure on the mechanical behavior of Cu-Nb fcc-bcc nanolayered composites, J. Mater. Sci. 49 (2014) 6497–6516.

[9] A. Misra, J.P. Hirth, R.G. Hoagland, Length-scale-dependent deformation mechanisms in incoherent metallic multilayered composites, Acta Mater. 53 (2005) 4817–4824.

[10] P.M. Anderson, T. Foecke, P.M. Hazzledine, Dislocation-Based Deformation Mechanisms in Metallic Nanolaminates, MRS Bull. (1999) 27–33.

[11] A. Misra, R.G. Hoagland, Plastic flow stability of metallic nanolaminate composites, J. Mater. Sci. 42 (2007) 1765–1771.

[12] R.G. Hoagland, R.J. Kurtz, C.H. Henager Jr., Slip resistance of interfaces and the strength of metallic multilayer composites, Scr. Mater. 50 (2004) 775–779.

[13] N. Jia, F. Roters, P. Eisenlohr, D. Raabe, X. Zhao, Simulation of shear banding in heterophase co-deformation: Example of plane strain compressed Cu-Ag and Cu-Nb metal matrix composites, Acta Mater. 61 (2013) 4591–4606.

[14] N. Jia, D. Raabe, X. Zhao, Texture and microstructure evolution during non-crystallographic shear banding in a plane strain compressed Cu–Ag metal matrix composite, Acta Mater. 76 (2014) 238–251.

[15] J.S. Carpenter, S.C. Vogel, J.E. LeDonne, D.L. Hammon, I.J. Beyerlein, N.A. Mara, Bulk texture evolution of Cu-Nb nanolamellar composites during accumulative roll bonding, Acta Mater. 60 (2012) 1576–1586.

[16] Y.Z. Tian, S.D. Wu, Z.F. Zhang, R.B. Figueiredo, N. Gao, T.G. Langdon, Microstructural evolution and mechanical properties of a two-phase Cu–Ag alloy processed by high-pressure torsion to ultrahigh strains, Acta Mater. 59 (2011) 2783–2796.

[17] S. Ohsaki, S. Kato, N. Tsuji, T. Ohkubo, K. Hono, Bulk mechanical alloying of Cu–Ag and Cu/Zr two-phase microstructures by accumulative roll-bonding process, Acta Mater. 55 (2007) 2885–2895.

[18] K. Uenishi, K.F. Kobayashi, K.N. Ishihara, P.H. Shingu, Formation of a supersaturated solid solution in the Ag-Cu system by mechanical alloying, Mater. Sci. Eng. A. 134 (1991) 1342–1345.

[19] S. Zghal, M.J. Hÿtch, J.-P. Chevalier, R. Twesten, F. Wu, P. Bellon, Electron microscopy nanoscale characterization of ball-milled Cu–Ag powders. Part I: Solid solution synthesized by cryo-milling, Acta Mater. 50 (2002) 4695–4709.

[20] S.N. Arshad, T.G. Lach, M. Pouryazdan, H. Hahn, P. Bellon, S.J. Dillon, R.S. Averback, Dependence of shear-induced mixing on length scale, Scr. Mater. 68 (2013) 215–218.

[21] M. Pouryazdan, D. Schwen, D. Wang, T. Scherer, H. Hahn, R.S. Averback, P. Bellon, Forced chemical mixing of immiscible Ag-Cu heterointerfaces using high-pressure torsion, Phys. Rev. B. 86 (2012) 144302.

[22] X. Sauvage, R. Pippan, Nanoscaled structure of a Cu–Fe composite processed by high-pressure torsion, Mater. Sci. Eng. A. 410-411 (2005) 345–347.

[23] A. Bachmaier, G.B. Rathmayr, M. Bartosik, D. Apel, Z. Zhang, R. Pippan, New insights on the formation of supersaturated solid solutions in the Cu–Cr system deformed by high-pressure torsion, Acta Mater. 69 (2014) 301–313.

[24] K.S. Kormout, B. Yang, R. Pippan, Deformation Behavior and Microstructural Evolution of Cu-Ag Alloys Processed by High-Pressure Torsion, Adv. Eng. Mater. 17 (2015) 1828–1834.

[25] R. Pippan, S. Scheriau, A. Hohenwarter, M. Hafok, Advantages and limitations of HPT : a review, Mater. Sci. Forum. 584-586 (2008) 16–21.

[26] M. Hafok, R. Pippan, Post-shear deformation of high pressure torsion-deformed nickel under hydrostatic pressure, Scr. Mater. 56 (2007) 757–760.

[27] A.P. Hammersley, S.O. Svensson, M. Hanfland, A.N. Fitch, D. Häusermann, Two-dimensional detector software: From real detector to idealised image or two-theta scan, High Press. Res. 14 (1996) 235–248.

[28] T.H. de Keijser, J.I. Langford, E.J. Mittemeijer, A.B.P. Vogels, Use of the Voigt function in a single-line method for the analysis of X-ray diffraction line broadening, J. Appl. Crystallogr. 15 (1982) 308–314.

[29] W.C. Oliver, G.M. Pharr, Measurement of hardness and elastic modulus by instrumented indentation: Advances in understanding and refinements to methodology, J. Mater. Res. 19 (2004) 3–20.

[30] V. Maier, K. Durst, J. Mueller, B. Backes, H.W. Höppel, M. Göken, Nanoindentation strain-rate jump tests for determining the local strain-rate sensitivity in nanocrystalline Ni and ultrafine-grained Al, J. Mater. Res. 26 (2011) 1421–1430.

[31] V. Maier, A. Hohenwarter, R. Pippan, D. Kiener, Thermally activated deformation processes in body-centered cubic Cr - How microstructure influences strain-rate sensitivity, Scr. Mater. 106 (2015) 42–45.

[32] C. Gammer, C. Mangler, C. Rentenberger, H.P. Karnthaler, Quantitative local profile analysis of nanomaterials by electron diffraction, Scr. Mater. 63 (2010) 312–315.

[33] R. Pippan, S. Scheriau, A. Taylor, M. Hafok, A. Hohenwarter, A. Bachmaier, Saturation of Fragmentation During Severe Plastic Deformation, Annu. Rev. Mater. Res. 40 (2010) 319–343.

[34] A. Bachmaier, A. Hohenwarter, R. Pippan, New procedure to generate stable nanocrystallites by severe plastic deformation, Scr. Mater. 61 (2009) 1016–1019.

[35] O. Renk, A. Hohenwarter, S. Wurster, R. Pippan, Direct evidence for grain boundary motion as the dominant restoration mechanism in the steady-state regime of extremely cold-rolled copper, Acta Mater. 77 (2014) 401–410.

[36] A.S. Malin, M. Hatherly, Microstructure of cold-rolled copper, Met. Sci. 13 (1979) 463–472.

[37] H. Paul, A. Morawiec, J.H. Driver, E. Bouzy, On twinning and shear banding in a Cu-8 at.% Al alloy plane strain compressed at 77 K, Int. J. Plast. 25 (2009) 1588–1608.

[38] H. Paul, J.H. Driver, Z. Jasieński, Shear banding and recrystallization nucleation in a Cu–2%Al alloy single crystal, Acta Mater. 50 (2002) 815–830.

[39] H. Paul, J.H. Driver, C. Maurice, A. Piatkowski, The role of shear banding on deformation texture in low stacking fault energy metals as characterized on model Ag crystals, Acta Mater. 55 (2007) 575–588.

[40] C.S. Hong, N.R. Tao, X. Huang, K. Lu, Nucleation and thickening of shear bands in nano-scale twin/matrix lamellae of a Cu-Al alloy processed by dynamic plastic deformation, Acta Mater. 58 (2010) 3103–3116.

[41] M. Blicharski, S. Gorczyca, Structural inhomogeneity of deformed austenitic stainless steel, Met. Sci. 12 (1978) 303–312.

[42] T. Morikawa, D. Senba, K. Higashida, R. Onodera, Micro shear bands in cold-rolled austenitic stainless steel, Mater. Trans. 40 (1999) 891 – 894.

[43] W.Y. Yeung, B.J. Duggan, Flow localization in cold-rolled α-brass, Mater. Sci. Technol. 2 (1986) 552–558.

[44] D. Jia, K.T. Ramesh, E. Ma, Effects of nanocrystalline and ultrafine grain sizes on constitutive behavior and shear bands in iron, Acta Mater. 51 (2003) 3495–3509.

[45] A. Bachmaier, R. Pippan, Generation of metallic nanocomposites by severe plastic deformation, Int. Mater. Rev. 58 (2013) 41–62.

[46] M. Hatherly, A.S. Malin, SHEAR BANDS IN DEFORMED METALS, Scr. Metall. 18 (1984) 449–454.

[47] A.L. Greer, Y.Q. Cheng, E. Ma, Shear bands in metallic glasses, Mater. Sci. Eng. R. 74 (2013) 71–132.

IV Deformation-induced supersaturation in immiscible material systems during high-pressure torsion

K.S. Kormout[1], R. Pippan[1,2] and A. Bachmaier[1]

[1]Erich Schmid Institute of Materials Science, Austrian Academy of Sciences

[2]Department of Materials Physics, Montanuniversität Leoben

Abstract. The review focuses on the supersaturation process of immiscible elements induced by severe plastic deformation. A variety of investigated material systems offers the systematic analysis of the controlling factors for mechanical intermixing, which are mainly determined by the level of the heat of mixing and the deformation behavior. The homogeneity of the deformation process strongly influences the degree of intermixing. The material systems can be divided in three groups. First, systems with large hardness mismatch of the phases leading to strong local plasticity in the soft phase. Second, systems with phases with similar ductility, in which both phases co-deform and third, systems, which show a strong tendency for shear band formation. In the fcc-bcc systems the heat of mixing and the hardness differences correlate, and with it the degree of supersaturation. In fcc-fcc systems, shear band formation prevents homogenous deformation of the composites and therefore limits the degree of supersaturation. The fcc-hcp system attains the highest degree of supersaturation, although strength differences are relatively high. Our results show that the fundamental mixing mechanism during deformation is not necessarily the same in all systems, but depends also on the strength differences of the phases and accordingly the deformation behavior.

IV.1 Introduction

The first observations of mechanical alloying or deformation-induced mixing were made in ball milling experiments. Extended solubilities or complete supersaturation was achieved in many material systems, such as Cu-Cr [1], Cu-W [2], Cu-Co [3], Cu-Ag [4–6], Ni-Ag [7], Cu-Fe [8–11], or Ag-Fe [12]. A review on mechanical alloying can be found in reference [13]. Since Li et al. [14] provided evidence that the dissolution of cementite and consequential supersaturation of carbon in ferrite in perlitic steel wires led to extraordinary high strength, the phenomenon of deformation-induced mixing in usually immiscible systems has drawn increased attention to the materials science community. Composites of immiscible elements stand out due to the very high structural and thermal stability compared to single-phase alloys. For instance, developments in the mechanical and electrical properties of Cu-based composites proceed for applications in robotics and high-pulse field magnets [15–19]. Moreover, it is possible to tune magnetic properties by alloying or decomposition. Cu-Fe nanocomposites with small amounts of Cu are expected to have large magnetostrictive effects [20,21], and Cu-Co alloys with nano-sized Co precipitates in a Cu matrix are considered to exhibit a giant magnetoresistance effect [22,23].

Severe plastic deformation (SPD) techniques enable the production of composites with ultra-fine grained (UFG) or nanocrystalline (NC) microstructures. In particular, high-pressure torsion (HPT) deformation is widely used nowadays. This technique allows deformation under high hydrostatic pressure, and therefore enables the processing of a tremendous number of materials to very high strains without fracture of the sample. The possibility to easily change processing parameters such as deformation temperature, pressure, strain rate and applied strain makes this technique additionally attractive. Microstructure and properties can be tailored for specific applications by combining the optimum process parameters with intermediate or post-deformation heat treatments. To optimize the properties of composite materials, the required SPD production steps to generate the desired material need to be known. Thus, the deformation behavior and deformation-induced supersaturation or amorphization processes should be understood in detail. Numerous studies have addressed supersaturation processes in immiscible systems during SPD [24-32]. Because very high strains can be applied easily, the HPT deformation is a convenient technique to link microstructural changes with the deformation-induced mixing process of the constituent phases of the composites.

Despite the large number of studies, the underlying deformation-induced mixing processes and the critical factors defining the maximum solubility are still under debate [28,33–35]. Several studies indicate a strong link between the heat of mixing and the degree of supersaturation. In systems with low positive heat of mixing, as for example Cu-Ag, complete solid solutions are easily reached over the whole composition range during ball milling [36]. In contrast, in systems with high positive heat of mixing, such as Ni-Ag or Ag-Fe, only extended solubilities could be obtained [7,12,37]. Besides thermodynamic considerations, it is proposed that large differences in strength of the individual phases of the composites can lead to strong strain localization, thereby impeding to achieve full supersaturation during deformation. Since dislocations play a key role in the kinetic roughening model and the dislocation shuffling process, which are proposed to be mechanisms for deformation-induced mixing, the crystal structures of the present phases might additionally influence the amount of mixing [35,38].

The aim of this paper is to summarize our results on deformation-induced supersaturation, which is observed during HPT processing of several immiscible binary systems. This includes the Ni-Ag (fcc/fcc), Cu-W, Cu-Cr (fcc/bcc) and Cu-Co (fcc/hcp) systems, which have varying crystal structures and strength differences. Additionally, the combination of ductile metals such as Cu-Ag (fcc/fcc) and Cu-Fe (fcc/bcc) are investigated. All systems have a positive heat of mixing and show no intermetallic phases. The investigated composites are listed in Table 1 providing information about initial crystal structure, second phase content in at% and vol%, and the achieved microhardness and grain size after deformation. The article is divided in the following chapters: First, the differences between HPT processing of single-phase and composite materials are outlined. Second, the HPT technique is described, including a two-step HPT process, which is especially important for the deformation of coarse composites. Then, the microstructural evolution and its influence on the formation of supersaturated solid solutions in the aforementioned material systems is summarized. The mixing mechanisms and the different factors, which influence deformation-induced mixing, are described in the following. Finally, the enhanced thermal stability of the HPT deformed composite materials is shortly discussed.

IV.2 Differences in deformation of single-phase and composite materials

The deformation of pure metals and single-phase alloys by SPD has been investigated intensively in the last two decades and a fundamental understanding of the formation of UFG or NC structures during SPD processing has been provided. During the HPT process, a huge number of dislocations are accumulated. With ongoing deformation these dislocations arrange to new grain boundaries, which subdivide the initial grains and thereby finally transform the material into an UFG structure [39]. A steady state or saturation regime is then reached, in which grain size and hardness are at a constant level, for a detailed review the reader is referred to reference [39]. In the saturation regime, recovery mechanisms have to be active to maintain the grain structure. Renk et al. [40] supposed grain boundary motion to be the prevailing mechanism. In pure metals, the saturation microstructure is independent of the initial state of the material. For example, the same saturation microstructure was obtained for single-crystalline, poly-crystalline coarse-grained and electrodeposited NC Ni by HPT deformation [41,42]. The saturation grain size and consequently the saturation hardness of pure metals in HPT can be mainly varied by the deformation temperature and alloying elements/impurities [39,43]. To a minor degree the strain rate and applied pressure has also an influence [44].

During deformation of composites the same grain refinement processes are observed in the beginning of the deformation process within the respective phases. This is valid for phase dimensions in the micrometer range. In single-phase materials, relatively low applied strains (about $\varepsilon \sim 20$) are usually sufficient to reach saturation. In composites, however, much higher applied strains are needed due to a complex fragmentation processes, if a saturation is ever reached at all (by reasonable amounts of applied strains). To increase the effectiveness of composite processing, a two-step HPT process was developed by Bachmaier et al. [45]. Further details of the two-step process are given in the next chapter.

Different to pure metals or single-phase alloys, the initial structure in composite materials is also essential. The initial arrangement of phases plays a key role, because geometrical changes of the phases dominate the microstructural evolution and the deformation behavior. The volume fraction and mechanical properties (hardness, yield strength and strain hardening capability) of the constituent phases determine if co-deformation or predominant fracture of hard phases and localized plastic deformation of soft phases are the dominating deformation processes. Moreover, alloying and subsequent supersaturation of individual phases together with possible amorphization can lead to further hardening or softening [27], resulting in a very complex deformation behavior. Additionally, the strain path is important, as outlined by Bachmaier et al. [46].

IV.3 HPT deformation process

Nowadays a quasi-constrained HPT setup is widely used. As shown schematically in Figure VI.1a, two anvils with cavities, in which a disk-shaped sample is placed, are loaded under high pressure and rotated with respect to another. These cavities allow on the one hand a centering of the sample for accurate torsional straining and on the other hand a nearly hydrostatic pressure, the used setup has been described in detail in [47]. The deformation can be considered as simple shear and the applied strain γ can be evaluated as [48]:

$$\gamma = \frac{2\pi r}{t} n,$$

with the radius r and the thickness t of the sample and the number of rotations n. This is only valid if no thickness changes occur. The equivalent plastic strain can be calculated with a von Mises equivalent strain as:

$$\varepsilon = \frac{\gamma}{\sqrt{3}}.$$

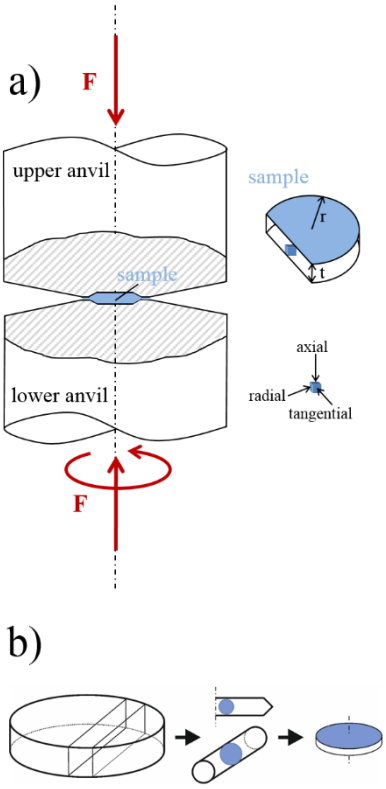

Figure IV.1: a) Schematic of the HPT process. b) Schematic of sample preparation for the two-step HPT process.

Due to the large miscibility gap in the investigated immiscible systems, a production route via conventional casting techniques is problematic. Therefore, one of the main challenges is to receive bulk starting materials. To overcome this problem, a production route via powders was established. Thereby almost unlimited material combinations can be produced by blending of elemental powders, which are either pre-compacted using inductive hot pressing or directly compacted in the HPT tool and subsequently deformed.

In order to accelerate the size reduction of phase elements, a two-step HPT process was introduced by Bachmaier et al. [45]. For this purpose, the powder blends or the initial composite material is first processed in a large HPT tool to obtain a sample with a diameter between 30 and 50 mm and thicknesses up to 10 mm. Afterwards a cylindrical rod is fabricated out of the sample (see schematic in Figure VI.1b). From this rod, new small disks are cut and

deformed with a smaller HPT tool. The new samples have typical diameters between 6 to 8 mm and thicknesses up to 1 mm. By this process the shear direction of the second HPT step is rotated by 90° in respect to the first HPT step. Thus, the alignment of the structural elements of the different phases of the composites from the first step is perpendicular to the shear direction in the second step. This increases the effectiveness of the HPT deformation enormously, but only in case ideal co-deformation occurs. However, as discussed in detail in the next section, this is not the case in many immiscible material systems.

Table 1: Summary of initial crystal structure, compositions in at% and vol%, Vickers microhardness and grain size in the saturation regime of HPT deformation for the investigated composites.

	at%/vol%	Vickers microhardness in saturation (-)	Grain size in saturation (nm)
Cu-Ag (fcc-fcc) [49,50]	Cu-6/12Ag	~355	~30-50 nm
	Cu-16/28Ag	~380	~20-40 nm
	Cu-36/54Ag	~340	~10 nm
Cu-Co (fcc-hcp) [51–54]	Cu-26/25Co	~280	~100 nm
	Cu-54/50Co	~400	<50 nm
	Cu-76/75Co	~450	<50 nm
Cu-Fe (fcc-bcc) [45]	Cu-15/12Fe	~330	<50 nm
	Cu-30/25Fe	~440	<50 nm
	Cu-50/44Fe	~445	<50 nm
	Cu-85/81Fe	~640	<50 nm
Cu-Cr (fcc-bcc) [27,55]	Cu-47/38Cr	~450	~10-20 nm
Ni-Ag (fcc-fcc) [56]	Ni-6/12Ag	~700	30-50 nm
	Ni-19/34Ag	~600	10-20 nm
	Ni-35/54Ag	~480	UFG + NC
	Ni-69/83Ag	~240	UFG + NC
Cu-W (fcc-bcc) [57–59]	Cu-25/69W	~550	~5-15 nm

IV.4 Deformation of immiscible binary systems

IV.4.1 Fcc-bcc

The starting composite material has usually a structural size in the micrometer range, as shown for example for Cu-25at%W (Figure VI.2a). The nearly equi-axed W particles appear bright in the backscatter-electron (BSE) scanning electron microscope (SEM) images and are homogenously distributed in the Cu matrix. Both phases are existent in similar volume fractions (see Table IV.1). After applying a shear strain of ε~16 the W particles are elongated in shearing direction and fracture of few particles is observed (Figure VI.2b). Inside the particles substructures are formed by dislocation accumulation and arrangement, as described in detail for pure metals [39]. Increasing the strain to ε~64 leads to heavy elongation of the W particles and additional refinement in some regions by repeated fractures, which generates very small W fragments distributed in the Cu phase (Figure VI.2c). Further increase in strain to ε~256 leads to a homogenization of the composite and a NC microstructure evolves, as seen in the transmission electron (TEM) bright-field (BF) micrograph in Figure VI.3a. From high-resolution TEM images a grain size of 5 to 15 nm was determined [59]. In the Cu-47at%Cr composite similar observations are made, the Cr particles are elongated and fractured, leading to a fine dispersion of Cr fragments in the Cu matrix. At an applied strain of ε~400 a homogenous NC structure is formed, with a somewhat larger grain size than in the Cu-25at%W alloy of about 10 to 20 nm [27], see TEM image in Figure VI.3b. The selected area diffraction (SAD) patterns displayed in Figure VI.3 reveal that in both composites the initial constituent phases are still present (diffraction rings are labeled for Cu and W in Figure VI.3a and for Cu and Cr in Figure VI.3b). Detailed diffraction analysis of larger volumes by X-Ray diffraction (XRD) measurements are displayed in Figure VI.4. XRD patterns of the Cu-25at%W composite recorded in the undeformed state and at applied strain levels from ε~16 to 512 reveal a strong broadening of the peaks due to the severe grain refinement. Additionally, the peaks are shifted from their position in the undeformed state, indicating lattice parameter changes and hence a dissolution of Cu in W and vice versa. Considering a "theoretical" fcc W lattice and using Vegard´s law, the solved amount can be roughly estimated. For this simple estimation, about 5 at% W is dissolved in the Cu phase and 4 at% Cu in the W phase, these values fit well to recent studies on sputter deposited Cu-W alloys [60].

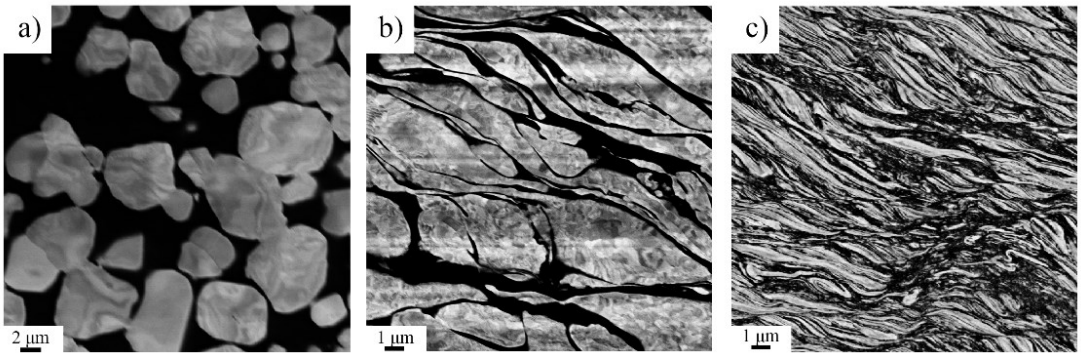

Figure IV.2: BSE-SEM micrographs of Cu-25at%W for a) undeformed bulk material with equi-axed W particles (bright contrast) embedded in the Cu matrix, b) at an applied strain of ε~16 revealing slight elongation of the W phase und the formation of substructures inside the W particles and c) at ε~64 strong elongation and fracturing of the W phase occurs leading to fine-dispersed W phase in the Cu phase.

In the Cu-47at%Cr composite, peak broadening and peak shift occurs in XRD measurements as well, indicating alloy formation (Figure VI.5b). Atom probe tomography (APT) offers information on the atomic scale distribution of the respective elements. An APT reconstruction from the as-deformed Cu-47at%Cr composite is presented in Figure VI.4c showing Cu- and Cr-rich grains separated by diffuse phase boundaries. A local concentration profile measured across a phase boundary reveals that the mixing occurs asymmetric. A considerable amount of about 15 at% of Cu is dissolved in the Cr phase, however, only 2 at% Cr could be solved in the Cu phase. In summary, the final microstructure obtained is a nanocomposite in Cu-25at%W and Cu-47at%Cr with partial supersaturation of the constituent phases at very high applied strains.

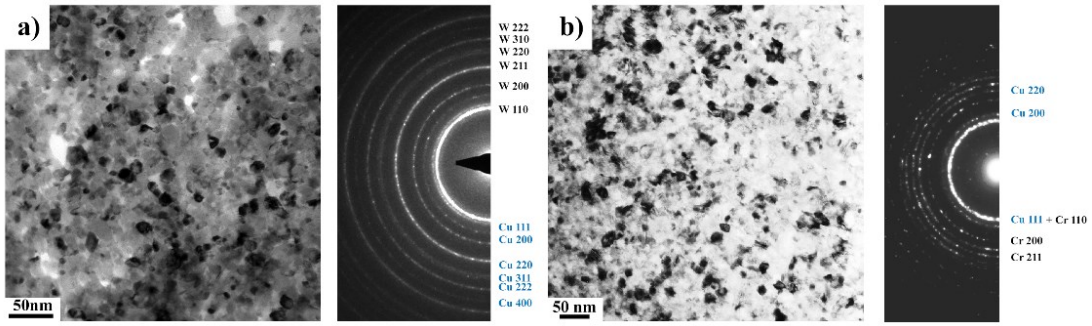

Fig. 3: TEM BF and corresponding SAD pattern in the saturation regime of deformation showing homogenous nanocrystalline microstructures of a) the Cu-25at%W composite at ε~256 with a grain size of 5-15 nm. The SAD pattern reveals both Cu and W phases as labeled. b) Microstructure of the Cu-47at%Cr composite at ε~400 with a grain size of 10-20 nm and SAD pattern with distinct diffraction rings of the Cu and the Cr phase (see labels).

Another investigated fcc-bcc system is Cu-Fe [45]. Four different compositions were deformed by the two-step HPT process as described in the previous chapter. SEM images recorded at low applied strains after the first HPT step (ε~40) reveal a different deformation behavior than in Cu-25at%W and Cu-47at%Cr. Both phases, Cu regions appear bright and Fe regions dark in this case, are elongated and a lamellar structure is formed for all four investigated compositions (exemplarily shown for Cu-85at%Fe and Cu-70at%Fe in Figure VI.5a and b). In the individual Cu and Fe phases an UFG structure with grain sizes between 200 nm and 400 nm develops in the different composites. Further refinement of the composites is realized by continuous thinning of the Cu and Fe lamellae (co-deformation). After the second HPT step, all composites exhibit a NC microstructure (Figure VI.5c-f). Only in the Cu-70at%Fe composite, bright and dark bands are still distinguishable, implying Cu and Fe-rich regions (Figure VI.5d). A homogenous structure is seen for the other three compositions in SEM images (Figure VI.5c, e and f). XRD measurements reveal that in the Cu-15 and 85at%Fe composites the peaks of the minor phase, which are clearly visible after the first HPT step, are not observed after the second HPT step [61]. This indicates that single-phase supersaturated alloys are formed at high and low Fe content. In the medium composition range, Cu-50at%Fe and Cu-70at%Fe, a peak shift is observed after the second HPT step. However, Cu and Fe phases still contribute to the diffraction pattern and Fe-Cu composites composed of fcc Cu-rich and bcc Fe-rich solid solutions are obtained. APT analysis of the Cu-50at%Fe composite reveals that a maximum of about 25 at% Cu is dissolved in the Fe phase and about 20 at% Fe in the Cu phase [61].

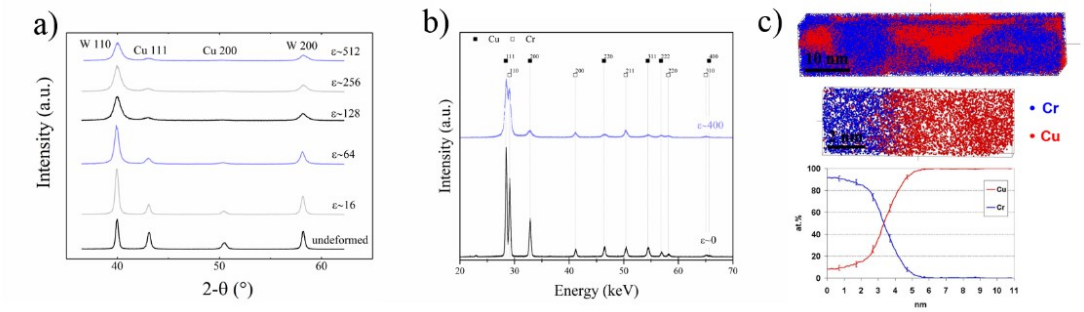

Fig. 4: a) XRD patterns of the Cu-25at%W composite recorded in the undeformed state and at different applied strains from ε~16 to 512, revealing strong peak broadening due to grain refinement and peak shifts indicating dissolution of Cu and W. b) XRD pattern of the Cu-47at%Cr for the undeformed state and at an applied strain of ε~400, peak broadening and shift is observed as well. c) APT analysis for Cu-47at%Cr with reconstructed tip and local concentration profile revealing a dissolution of 15at% Cu in the Cr phase and of 2at% Cr in Cu.

At the highest amount of applied strain a NC microstructure is obtained in all three investigated fcc-bcc systems. Cu-W, Cu-Cr and Cu-Fe form for medium compositions, where the phases exist in similar volume fractions, a nanocomposite with partial supersaturation of the respective phases. In the Cu-Cr and Cu-W system, the deformation is governed by strong plasticity in the softer Cu phase together with heavy elongation and repeated fracture of the harder W and Cr particles. In Cu-Fe, co-deformation of both phases occurs to a greater extent, which leads to complete single-phase supersaturated solid solutions for high and low Fe contents.

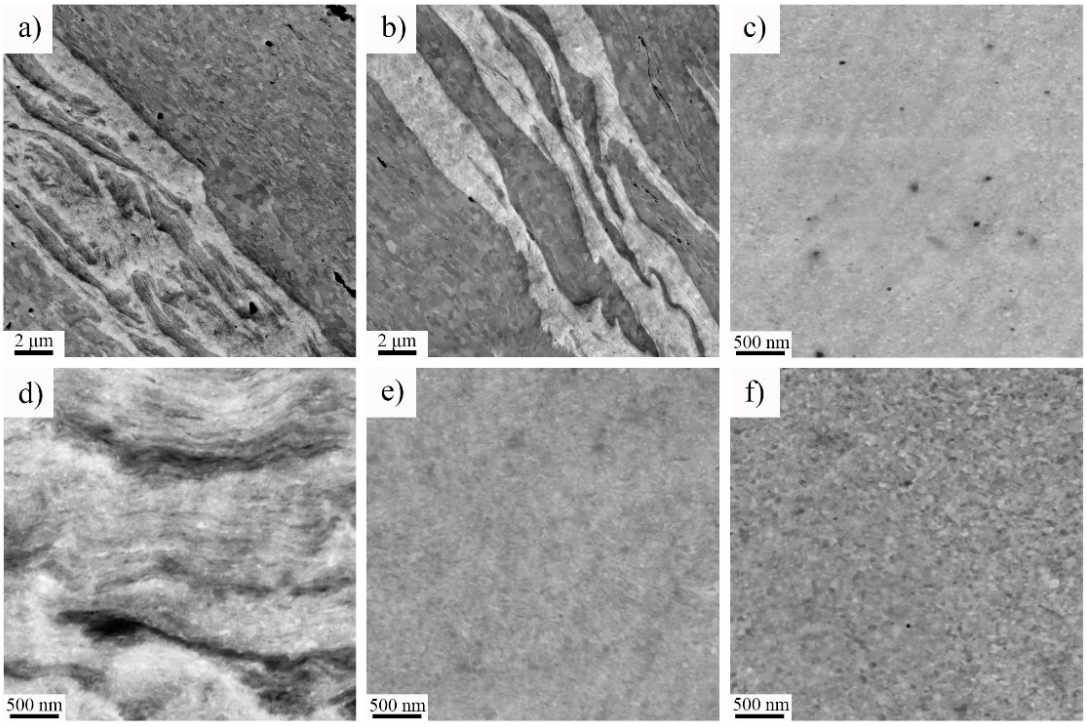

Fig. 5: BSE micrographs after the first HPT step at ε~40 of a) Cu-85at%Fe and b) Cu-70at%Fe showing lamellar composites (Cu phase with bright and Fe phase with dark contrast) with UFG structures in the individual phases. A BSE-SEM micrograph after the second HPT step (minimum ε~1100), showing nanocrystalline microstructures for c) Cu-85at%Fe, d) Cu-70at%Fe, e) Cu-50at%Fe and f) Cu-15at%Fe with chemical contrast only visible in the Cu-70at%Fe (bright and dark bands indicating Cu-rich and Fe-rich regions).

IV.4.2 Fcc-fcc

The fcc-fcc systems have been investigated by our group as well. Elemental powders were mixed in several compositions and processed by a single or two-step HPT process. In the Cu-Ag system, a lamellar structure is formed at low strains independent of composition as shown exemplarily for Cu-6 and 36at%Ag in Figure VI.6 a and d. In the individual Cu and Ag phases, an UFG structure is formed. The obtained saturation grain size is in the same range as observed also for the pure Cu and Ag powders deformed to saturation (see EBSD scans in [50]). At higher applied strains, different deformation behaviors are observed in the composites, depending if the Cu and Ag phases are present in minor or balanced volume fractions. In the Cu-6at%Ag composite, co-deformation and extensive refinement of both phases leads to a homogeneous NC microstructure (Figure VI.6b and c). In the Cu-36at%Ag composite, extensive shear band formation (Figure VI.6e) prevents homogenization of the composite (Figure VI.6f).

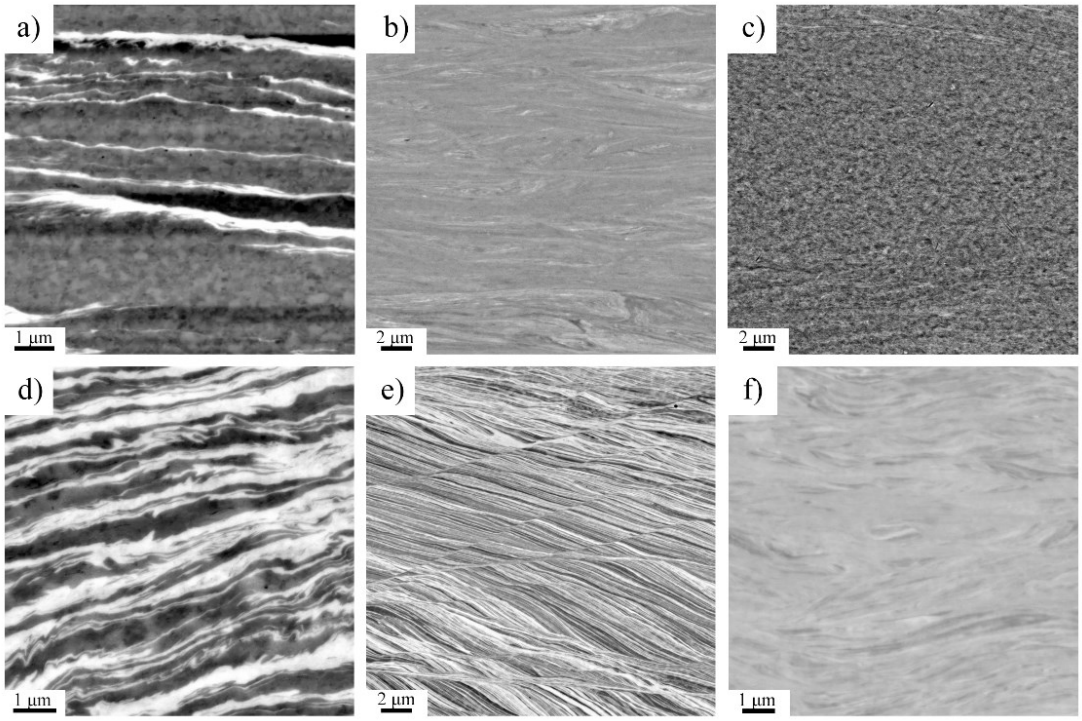

Fig. 6: BSE-SEM micrographs at different applied strains for the Cu-6at%Ag composite a) at ε~75 showing a lamellar structure with thin Ag layers, b) at ε~435 revealing strong refinement of the composite and c) a homogenous nanocrystalline microstructure is obtained in saturation at ε~1100. BSE micrographs of Cu-36at%Ag d) at ε~75 showing also a lamellar composite, e) at ε~220 numerous shear bands are observed, f) at ε~1100 inhomogeneities in the composite are still present.

As revealed by TEM investigations, the lamella thickness is reduced to several nanometer (Figure VI.7a) before shear band formation sets in. Within the shear bands a strong refinement to a nearly equi-axed NC structure is observed (Figure VI.7b and c). With increasing strain, new shear bands are formed continuously and a large part of the sample is transformed into this NC state (Figure VI.7d). The structure is characterized by a very high defect density, as seen from the strong contrast variations in TEM BF and dark-field (DF) images in Figure VI.7e, and from the significant broadening of the diffraction rings in the SAD pattern in Figure VI.7f. Diffraction rings of the Ag, the Cu and a supersaturated phase, which is generated in the shear bands, are present (labeled in Figure VI.7f). The occurrence of the formed supersaturated solid solution, which attains the global composition of Cu-36at%Ag, is also confirmed by synchrotron XRD measurements. In the Cu36at%Ag composite the total imposed shear strain at very high strains is only carried by a limited number of shear bands. This prevents complete supersaturation and homogenization of the sample, instead a nanocomposite is obtained consisting of single-phase supersaturated regions (generated in the shear bands) and remaining lamellar dual-phase regions. Evaluation of peak shifts in the XRD measurements reveal that also in the lamellar matrix a partial supersaturation of the Cu and Ag phase (below 8%) occurs. In Cu-16 and 85at%Ag composites the maximum achievable degree of supersaturation is found to be about 23 at% Cu solved in Ag, while only 12 at% Ag could be solved in Cu. However, in the Cu-36at%Ag composite locally a supersaturated solid solution of 36at% Ag in Cu can be attained inside the shear bands.

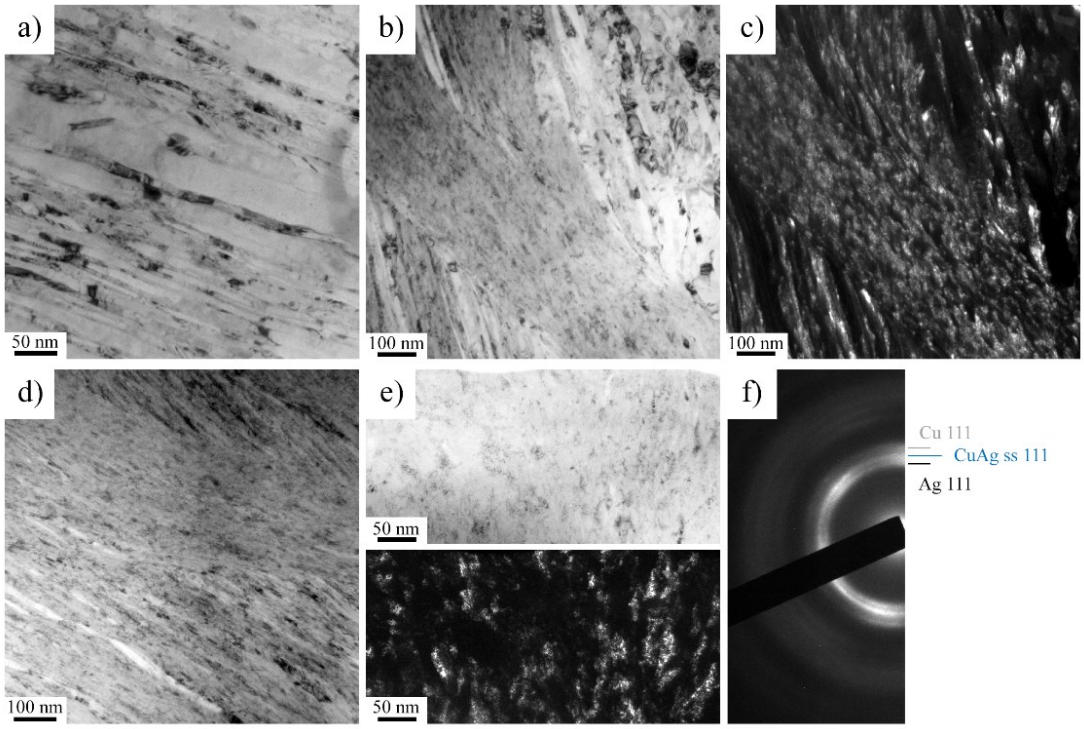

Fig. 7: TEM investigations on Cu-36at%Ag composite. a) nano-lamellar structure at ε~110. b and c) shear band at ε~220 in BF and DF mode revealing an equi-axed structure inside the shear bands. d) strong refinement at ε~1100 by shear bands with remaining lamellar regions. e) BF and DF image at ε~2200 revealing the very high defect density (see strong contrast changes in the images). f) SAD pattern at ε~2200, diffraction rings of Cu, Ag and the supersaturated phase, which is formed in the shear bands, are indicated.

The second fcc-fcc combination which has been investigated are Ni-Ag composites. Ni-35 and 69at%Ag composites were deformed in a single-step HPT process. As seen in Figure VI.8a, the Ni particles show almost no shape change after compaction of the powders, because the hardness is much higher than of the Ag powder. An applied strain of ε~90 results in elongation and fracturing by necking of the elongated Ni particles (Figure VI.8b), which is similar as observed in the Cu-25at%W and Cu-47at%Cr composites (compare with Figure VI.2). Further deformation refines the composite to a lamellar structure (Figure VI.8c), as also observed in Cu-Fe and Cu-Ag composites. At higher applied strains, an inhomogeneous structure evolves due to strain localization in Ag-rich regions and pronounced shear band formation. UFG pure Ni regions are still retained besides strongly refined lamellar regions even at applied strains of ε~1800 (see Figure VI.8d). Due to the higher Ag content this inhomogeneous deformation is even more pronounced in the Ni-69at%Ag composite (see Figure VI.8e and f). Ni-Ag composites with a content of 6 and 19at% Ag were deformed in a two-step HPT process. For these high Ni contents, co-deformation of both phases occurs also at higher strains. Similar as in the Cu-Fe composites both phases are continuously refined. In the saturation regime a NC microstructure is formed and full supersaturation was achieved (for details see reference [56]).

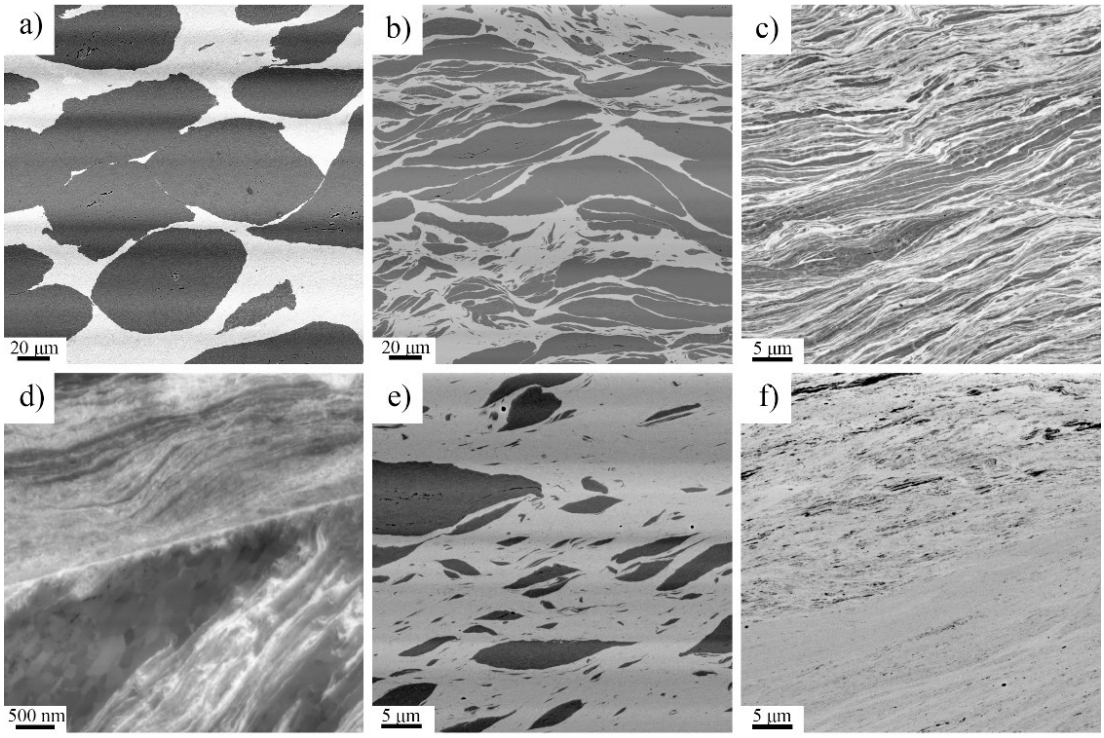

Fig. 8: BSE-SEM micrographs of Ni-35at%Ag at a) ε~0 with Ni powder particles (dark contrast) embedded in Ag phase (bright contrast), b) at ε~90 showing elongation and fracturing of Ni particles. c) at ε~180 a lamellar structure has formed and d) at ε~1800 inhomogeneities are still present. BSE-SEM micrographs of Ni-69at%Ag at e) ε~180, large Ni particles are still present, and f) ε~1800 showing an inhomogeneous structure.

IV.4.3 Fcc-hcp

As fcc-hcp model system Cu-Co composites were chosen and three initial compositions, Cu-26,54 and 76at%Co, were investigated. The microstructure as a function of applied strain is presented in Figure VI.9 exemplarily for the Cu-76at%Co composite. Similar observations are made in all compositions at low strains, the Co particles (dark contrast), which are slightly elongated as a result of the applied shear strain, are inhomogeneously distributed within the Cu (see Figure VI.9a). In the Cu-26 and 54at%Co composites the Co phase is embedded in the Cu matrix, while Cu is the minor phase in Cu76at%Co composite. By increasing the applied strain, further elongation and necking leads to refinement of the Co particles, see Figure VI.9b and c. It is proposed that the Cu matrix carries a large amount of the imposed strain, while the harder Co phase deforms mainly by necking and fracture of the particles, as also observed in Cu-25at%W and Cu-47at%Cr. In the individual Cu and Co phases UFG structures are formed. Exceeding applied strains of about $\varepsilon\sim100$ residual Co particles are still present in the Cu-26 and 54at%Co composite. In the Cu-76at%Co composite a homogeneous microstructure is observed, although bands with bright and dark contrast indicate Cu- and Co-rich regions [54]. However, homogenous microstructures are reached if only a small additional amount of strain is applied. The same is observed in the Cu54-at%Co composite. In contrast, an applied strain of $\varepsilon\sim500$ is needed for the Cu-26at%Co composite to homogenize the microstructure on a microscopic level. Nevertheless, few Co particles are still visible in SEM micrographs. In all three compositions, NC microstructures are obtained at high applied strains, see Figure VI.10d to f for Cu-26, 54 and 76at%Co, respectively. As can be seen from TEM diffraction patterns (Figure VI.9g to h), only fcc lattices are present for all compositions. A phase transformation of Co from hcp to fcc takes place during deformation [62], which might be further promoted by the dissolved Cu.

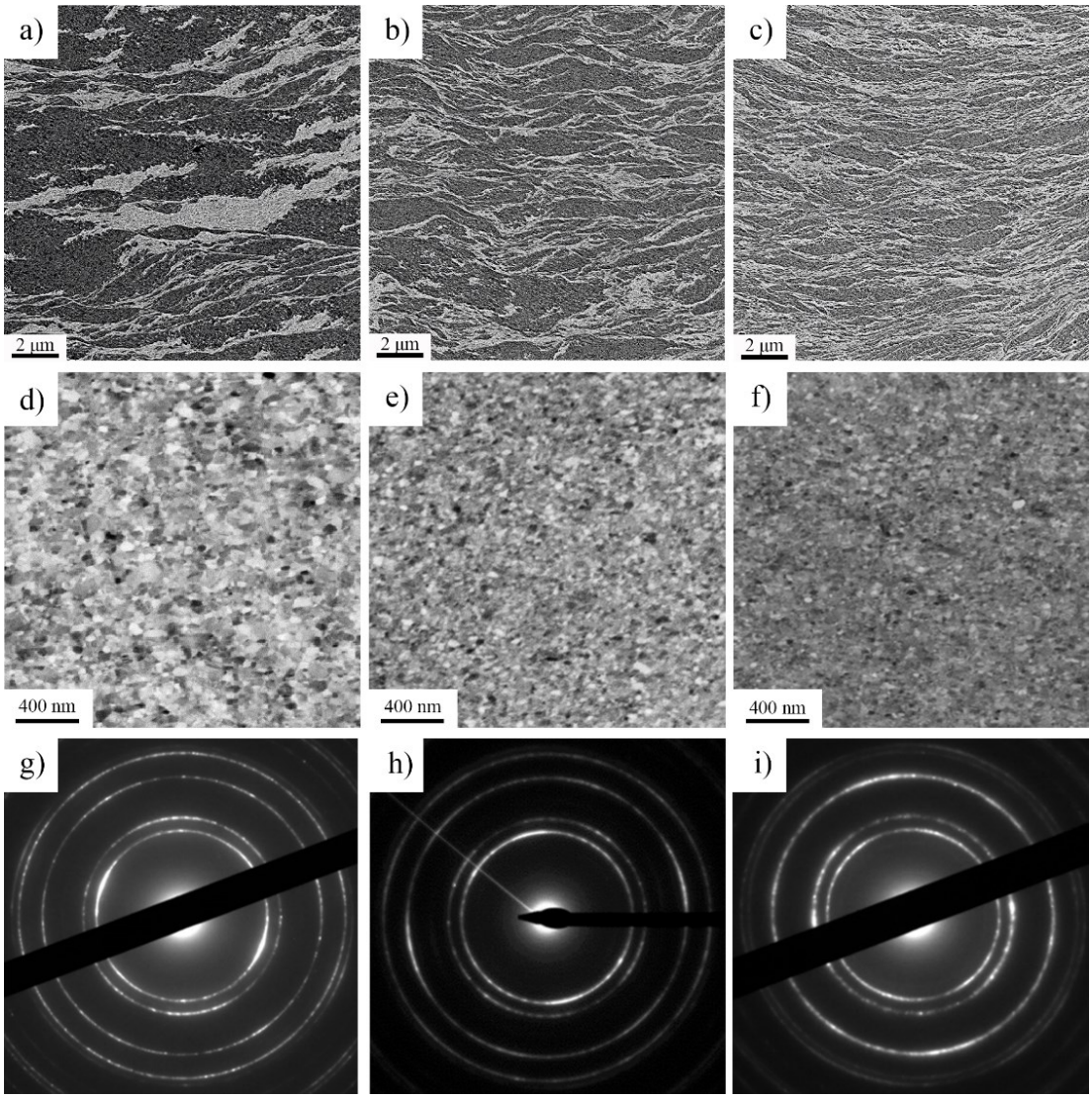

Fig. 9: BSE-SEM micrographs of the Cu-76at%Co composite at a) ε~10, b) ε~25, c) ε~100. BSE-SEM micrographs of the microstructures at the highest amount of applied strain for d) Cu-26at%Co, e) Cu-54at%Co and f) Cu-76at%Co with corresponding diffractions patterns for g) Cu-26at%Co, h) Cu-54at%Co and i) Cu-76at%Co.

To study the chemical intermixing on the atomic level, EELS (electron energy-loss spectroscopy) and APT analyses were conducted at different strain levels. A top view of an APT reconstruction for Cu-76at%Co at low applied strains of ε~30 is shown in Figure VI.10a. The concentration profiles reveal different supersaturation levels in the Cu and Co phase (blue isoconcentration surface corresponding to 54at% Cu). The concentration profile along cylinder A shows substantial dissolution of about 40% Co in the thin Cu region, but in the surrounding Co phase no Cu was detected. Also no Co was solved in the larger Cu region on the left. Contrary, the concentration profile B gives a Cu concentration in Co up to 30at% behind the thin Cu region. A reconstruction of an APT tip in a side and top view is presented in Figure VI.10b and c. The concentration profile (measured along the cylinder indicated in Figure

VI.10c) reveals a Cu concentration of 30at% in the thin Co phase, additionally Co dissolved in the Cu phase as well with concentrations up to 40at%. Thus, it can be concluded that the mixing process starts already at relatively low strains in the Cu-76at%Co composite.

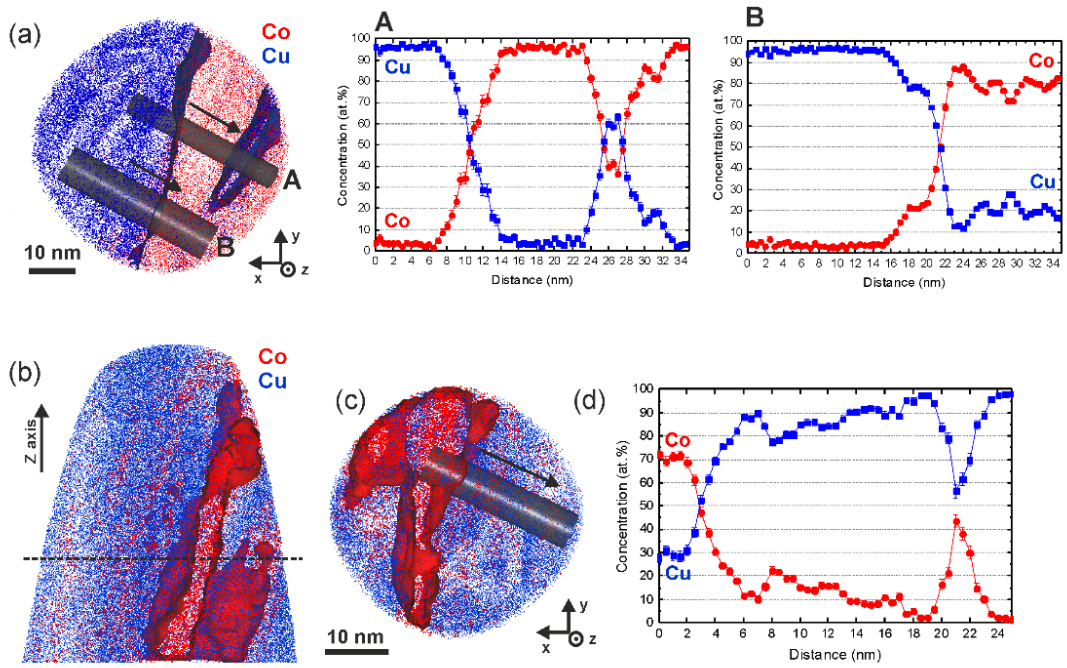

Figure IV.10: APT reconstructions of a Cu phase in Cu-76 at.%Co (ε~30): a) Tomographic slice (top-view, thickness of 10 nm), in which the blue isoconcentration surface corresponds to 54 at.%Cu. 1D-concentration profiles are computed along the region-of-interests ("A" and "B"), b) tomographic slice (side-view, thickness of 10 nm), in which the red isodensity surface corresponds to 14 Co atoms nm^{-3}, c) top-view of a tomographic slice along the z-axis as marked in b) by dotted line with a thickness of 10 nm and (d) 1D-concentration profile plotted along the marked region-of-interest in c). Reproduced with permission from [52]. Creative Commons Attribution License (CC BY 4.0) 2016 Elsevier.

In the Cu-26at%Co composite Co particles persist even at the highest conducted strain level, as revealed by SEM and TEM [53]. Several EELS line measurements performed at a strain of ε~100 across Co particles revealed an asymmetric mixing: a dissolution of up to 30at% Co was observed in the Cu phase, while no Cu was detected in the Co grains. APT analyses at the highest applied strain level gives a local composition of 25.6at% Co, which is in quite good agreement with the nominal composition of 26at% Co. For the Cu-76at%Co composite, the average Cu concentration determined by APT is 22-24at% in Co [53]. The concentration profiles obtained from EELS measurements from the Cu-54at%Co composite at ε~440 include several grains and show a relatively homogenous distribution of Cu and Co (for details see reference [54]).

In the saturation regime of deformation, a homogeneous distribution of Cu and Co atoms is observed as confirmed by APT analysis and EELS measurements in the Cu-Co composites (for details see references [53,54]). TEM diffraction data further indicates that a single-phase fcc solid solution has formed in composites with low and high Co content. Supersaturated solid solutions can be also obtained in the Cu-54at%Co composite. However, due to the very similar

lattice parameters of fcc Cu and fcc Co, it cannot be differentiated if the composite is completely single-phase or consists of a mixture of supersaturated Cu- and Co-rich grains with up to 45-50 at% Cu dissolved in Co and vice versa.

In summary, a deformation-induced supersaturation process during HPT deformation is observed in all studied composites. The maximum achieved solubilities for each investigated system are depicted in Figure VI.11 and summarized in Table IV.2. In the Cu-25at%W and the Cu-47at%Cr composites, the constituent phases are existent in similar volume fractions. Due to the high hardness of the W and Cr phase, the deformation process is characterized by strong local plasticity in the soft Cu phase, and elongation and fracture of the harder W and Cr particles. Contrary the Cu-50at%Fe composite deforms by homogenous thinning of both phases. Nevertheless, in all three composites a partial supersaturation was obtained and the final NC microstructure is composed of Cu-rich grains and W/Cr/Fe-rich grains. In the Cu-Fe system, composites with high and low Fe content (15/85at%) were successfully deformed to single-phase supersaturated solid solutions. In the two fcc-fcc systems, strong shear localization occurs in Cu-36at%Ag and Ni-35 and 68at%Ag, preventing a homogenization of the composites and therefore also only partial supersaturation is obtained. When the Ni content reaches high volume fractions (Ni-6 and 19at%Ag), a more homogenous deformation behavior is observed and single-phase supersaturated solid solutions are formed. The same is observed in Cu-Ag composites with high and low Ag content. The composites of the fcc-hcp Cu-Co system deform very similar to the Cu-25at%W and Cu-47at%Cr composites. The softer Cu phase carries a large amount of the applied strain, while Co is refined mainly by elongation, necking and fracturing. However, although local chemical analyses exhibit high levels of supersaturation, the very similar lattice constants of fcc Cu and fcc Co prevent a clear differentiation between Cu-rich and Co-rich phases in diffraction experiments for medium compositions.

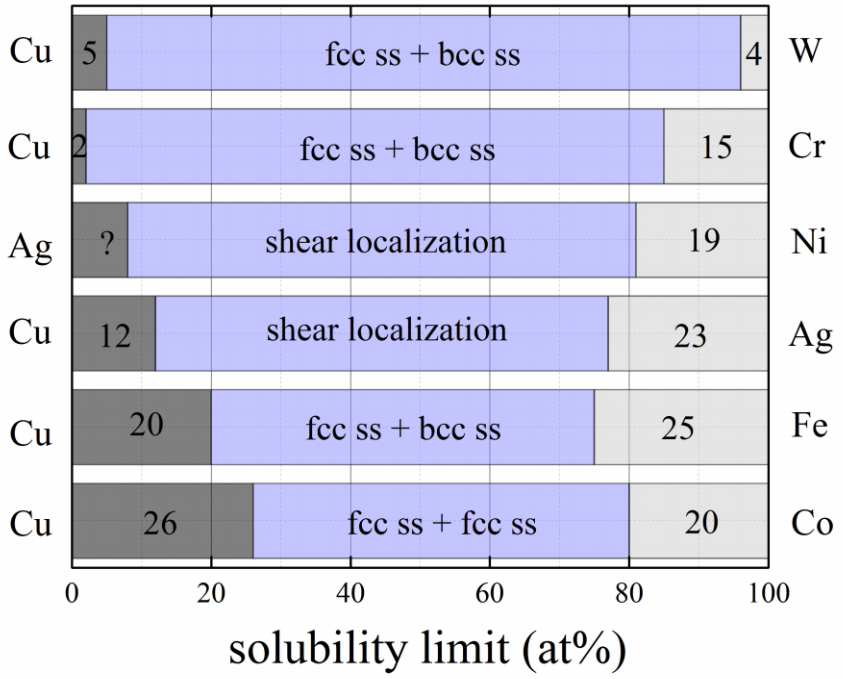

Fig. 11: Maximum achieved solubility in the different investigated systems.

Table 2: Summary of mixing enthalpies taken from literature, atomic radius mismatch (ratio of the atom species with smaller r_{small} and larger r_{large} atomic radius) and maximum obtained solubility from our experiments of the constituent phases in each investigated system.

	Cu-Ag	Cu-Co	Cu-Fe	Cu-Cr	Ni-Ag	Cu-W
ΔHmix	6 kJ/mol [63]	6.3 kJ/mol [3]	12kJ/mol [64]	20 kJ/mol [57]	15 kJ/mol [34]	35.5 kJ/mol [2]
rsmall/rlarge	12 %	2.5 %	1.5 %	0 %	14 %	8 %
Max solubility	~12 at% Ag in Cu ~23 at% Cu in Ag	~22-24 at% Cu in Co 40-50 at% Co in Cu	~20 at% Fe in Cu ~25 at% Cu in Fe	~2 at% Cr in Cu ~15 at% Cu in Cr	~19 at% Ag in Ni	~5 at% W in Cu ~4 at% Cu in W

IV.5 Process of deformation-induced mixing

The mechanism behind deformation-induced supersaturation, although intensively investigated, is still under debate [35,66,67]. The proposed concepts and their relevance to our studies will be summarized in the following section.

To explain the observed intermixing during ball milling experiments, Bellon and Averback proposed a mechanical mixing mechanism, the so-called "kinetic roughening model" [38]. In Monte Carlo simulations they showed a roughening of phase boundaries through extensive dislocation activity across these boundaries in fcc-fcc systems. In later studies they investigated also bcc-fcc phase boundaries by MD simulations, where dislocation transfer is in principal constricted [68]. The simulations showed no roughening of interfaces, however, mixing still occurred, and the authors explained this by dislocation pile-up at the boundaries. This leads to disordered regions, where the energy barriers are lowered, and local mechanical instabilities result in atom exchanges. They also studied the influence of different kind of interfaces on the mixing process. In general, in processes, which implicate a transport of atoms across interfaces by dislocation glide, the phase boundaries have to fulfill certain criteria. Embury et al. [69] defined the following points: the resolved shear stress at the boundary resulting from dislocation pile-up should be a maximum on the activated system, the misorientation of the active slip planes in the two involved grains should be a minimum and the configuration of the boundary should be one of minimum energy. It is evident, that these criteria are easier fulfilled in fcc-fcc systems, however, in fcc-bcc these conditions apply, if a Kurdjumov-Sachs orientation relationship is present, which was indeed observed in Cu-Nb sheets produced by accumulative roll bonding (ARB) [70]. Misra and Hoagland [71] showed that in ARB Cu-Nb the shear stress on dislocation is high enough to cross interfaces when layer thicknesses below 5 nm are reached. Orientation relationships between the constituent phases resulting from a

shear texture, which is often observed in HPT processed materials [41], is seen for example in Cu-Ag composites. An orientation relationship between Cu and Ag could facilitate a mixing process by dislocation glide across phase boundaries. In addition the phase spacing is in the nanometer range, see Figure VI.7, which is necessary to reach stress levels for interface cutting according to the study by Misra and Hoagland [71]. As revealed by XRD synchrotron measurements, massive mechanical mixing occurred in the shear bands, but also in lamellar regions a partial supersaturation of Cu and Ag was observed. While the deformation mechanism in the shear bands is still unclear, it is assumed that the lamellar matrix deforms by dislocation plasticity, which gives indication for a mechanical mixing by dislocations crossing interfaces. In the Cu-Co composites, in which fcc-hcp phase boundaries are present, a lattice change in the Co phase from hcp to fcc could enable such a mixing process. In the saturation regime of deformation the "kinetic roughening model" predicts that the degree of intermixing is determined by an equilibrium between mechanical mixing at interfaces and decomposition by thermal diffusion. Thus, by increasing the deformation temperature, the degree of supersaturation is lowered, this is indeed observed for example in Cu-Ag [49].

Raabe et al. considered as well dislocation motion across phase boundaries in their so-called "dislocation shuffling" model [35]. They assumed that multiple dislocation glide events on several planes across interfaces will move small particles into the other phase, and after repeated dislocation cutting processes, they will eventually dissolve due to the Gibbs-Thomson effect. They also indicated that the mixing process could be assisted by shear banding. A similar approach was contemplated by Yavari et al. [8] for mechanical mixing during ball milling. They assumed that small tips of one phase with a radius of only 2 nm or less are formed, and the atoms on the tip will dissolve due to capillary pressure (Gibbs-Thomson effect). Such small fragments of Fe in a Cu-Fe composite was indeed observed by Sauvage et al. [24].

Other studies take the modification of phase or grain boundaries during SPD processing into account, for example Veltl et al. [72], who suggested that the energy stored in the boundaries facilitates the intermixing. So-called "non-equilibrium" grain boundaries, as proposed by Valiev [73], are suggested to have increased capability to promote diffusion and also influence on the mechanical properties. As assumed by Sauvage et al. [28], such a modification of interfaces is necessary to enable dislocation glide across phase boundaries and subsequently to transfer atoms into the other phase [28]. Additionally, very high vacancy concentrations during HPT deformation together with the special configuration of grain/phase boundaries could enable defect-enhanced diffusion processes [10,74]. However, due to the positive mixing enthalpy there is in principal no thermodynamic driving force for mixing by diffusion.

In HPT processing the very high applied strains, which are obviously needed to induce chemical mixing, must be taken into account. In studies on Al alloys with Al_2O_3 particles it was shown, that it takes enormous strains to homogenously distribute the particles, which agglomerate in clusters [75]. A process similar to erosion was proposed. In systems with a hard minor phase, for example Ni-Ag with low Ni content, such an erosion process could also take place on the atomic scale. Another mechanism, which takes the large amount of applied strain into account, is a fracture and rebonding process [55]. In Cu-W and Cu-Cr, it appeared that the harder particles fracture repeatedly, and the softer phase filled the gap in between the broken particles. This Cu in between is deformed under high pressure, and could eventually dissolve in the other phase. These processes are independent of structural sizes and would start immediately with deformation. In the Cu-Co composites it was indeed shown, that the mixing process starts at relatively low strains ($\varepsilon \sim 30$ in the Cu-76at%Co composite) [53,54]. In APT analysis of Cu-Co an increased solute content was observed near nanometer sized particles, but

no distinct chemical gradients were observed at interfaces, see for example Cu-Cr (Figure VI.4) or Cu-Co (Figure VI.10). The lack of intermixing at phase boundaries and the increased solute content behind small particles at low applied strains in Cu-Co can be attributed to a process similar to abrasion, instead of a mixing based on dislocation motion across phase boundaries. However, it is assumed that the final dissolution at high applied strains could be realized by a dislocation-shuffling mechanism or defect-enhanced diffusion [54].

The first group of proposed mixing mechanism coincide in one point, that the supersaturation process is controlled by the strain level, hence a critical phase dimension in the nanometer regime is needed to induce the mixing process. The following criteria, established in the different approaches, are fulfilled, if this phase dimensions are reached:

1. Stresses on dislocations are high enough to enable dislocation glide across phase boundaries.
2. Possible phase transformations can occur, as for example in Co from hcp to fcc.
3. A huge amount of interfaces is available, which on the one hand show special characteristics in SPD processed materials, and on the other hand offer many sites for the mixing process.
4. Particles reach sizes below a critical level for dissolution by the Gibbs-Thomson effect.

Additionally, shear banding can provide high amounts of strains, accelerating the local mixing process.

The second group of mixing mechanisms account for the large amounts of strain applied during HPT processing. Mechanisms with similarities to erosion or abrasion were proposed. In this case the supersaturation process would start immediately with the deformation process, but it would require very high amounts of applied strain to homogenize the composites. These processes are mainly contemplated for composites with a hard phase, like Cu-W, Cu-Cr and Cu-Co. Similar assumptions are true for defect-enhanced diffusion processes, if a high vacancy concentration level is reached, mixing should start independently of structural sizes.

IV.6 Influencing factors

IV.6.1 Lattice structures

As proposed in several studies dislocation glide across phase boundaries accounts for the dissolution of the constituent phases, and therefore the lattice structures could have an influence on the solubility limit. As seen in Figure VI.11, the system with the highest achieved solubility are the fcc-hcp Cu-Co, in which supersaturated solid solutions with local concentrations of up to 50at% Cu and Co were obtained. In Cu-Co composites the fragmentation process generates Cu and Co particles having nanometer dimensions. APT and EELS analysis revealed that mixing starts already at relatively low applied strains in those nanometer phases. Moreover, it was shown that a lattice change in Co from hcp to fcc occurred at grain sizes below 100 nm [62], this could facilitate further mixing of Cu and Co at high strains. The developed supersaturated solid solutions exhibit therefore a fcc lattice at all compositions. Although in Fe a phase transformation to fcc is possible at grain sizes below 5 nm, no indications for such a lattice change was provided in our studies. In the Cu-Fe system the fcc phase is stabilized in composites with up to 20% Fe, while the bcc phase is stable up to 25% Cu in Fe. In the intermediate composition range a mixture of fcc Cu-rich and bcc Fe-rich phases is obtained. The same is observed in the other fcc-bcc systems, Cu-W and Cu-Cr, in which the Cu-W system is the one with the lowest solubility. Only 5 at% W could be solved in Cu and 4 at %

Cu in W. Based on the results for the different immiscible systems, different lattice structures are not a barrier for the supersaturation process.

IV.6.2 Hardness differences

In contrast to single-phase materials, a complex hardening behavior is usually observed in composites. The hardness as a function of applied strain is shown in Figure VI.12 for Cu-54at%Co, Cu-36at%Ag and Cu-47at%Cr. Such hardness profiles, in which three stages are distinguishable, are characteristic for binary immiscible composites. In the beginning of the deformation process of the composites, the present phases have dimensions in the micrometer regime, see for example bulk materials (Cu-W in Figure VI.2), or powders (Ni-Ag in Figure VI.8), which are usually between 10 and 50 µm. In the very beginning a steep hardness increase from the hardness level of the undeformed material to the first plateau is observed in the hardness evolution, as indicated in the schematic hardness plot in Figure VI.13. This hardness increase is induced by the deformation due to the compression to build up the applied pressure and the subsequent shear deformation, which causes the formation of substructures in the individual phases. However, this first increase is experimentally not captured in the hardness measurements, because it usually begins to saturate at ε~1. In the hardness evolution of the Cu-47at%Cr composite in Figure VI.12c the hardness level of the undeformed material is also included, before ε~1 is reached the hardness already increases from ~100 HV to ~200 HV. At low applied strains, a constant hardness level or a slight increase is observed (continuous and dashed line labeled as stage A in Figure VI.13). In stage B, the hardness strongly increases due to extensive refinement of the structure. Different deformation mechanisms are responsible in different material systems, which depends on kind and volume fraction of the present phases, as discussed in detail in the following. After stage B, a saturation regime is reached (stage C), where the hardness is at a constant level, although a minor increase or decrease can be observed in some cases due to solid solution hardening or softening (indicated by dashed lines).

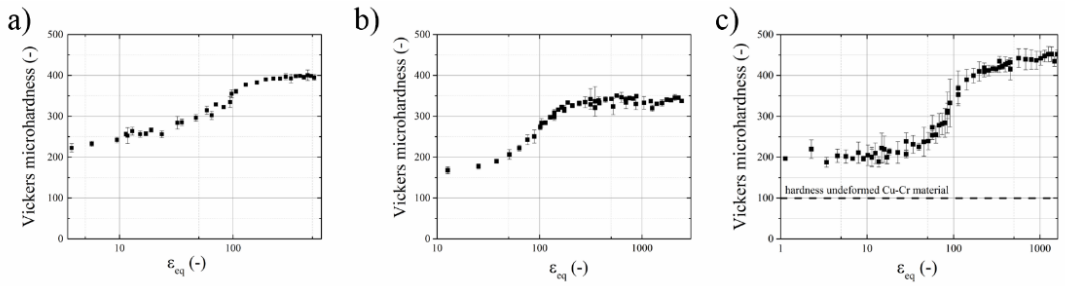

Fig. 12: Vickers microhardness as a function of applied strain for a) Cu-54at%Co, b) Cu-36at%Ag and c) Cu-47at%Cr.

Figure VI.13 displays schematically the influence of the hardness differences and volume fraction of the phases on the microstructural evolution and deformation. In case of large hardness differences between the phases, they will generally not deform to the same extent, as observed experimentally for Cu-W, Cu-Cr, Cu-Co and Ni-Ag. If the hard phase has a minor volume fraction, this is even more pronounced. In the beginning of the deformation process, the softer matrix will form an UFG saturation structure, with a lower hardness level than the hard phase, corresponding to the first stage A in the schematic hardness evolution. As a consequence the soft phase will carry most of the deformation. If the volume fraction is low enough, the hard particles will flow in the soft matrix, see schematic in Figure VI.13, and only

in rare cases, two particles could get bonded and fractured again. This was experimentally observed in Al alloys with ceramic particles (SiC and Al_2O_3) [75], in which an extreme hardness difference between the phases is present. This could be also the case for example in a Cu-W composite with a very low volume fraction of W. If the volume fraction of the hard phase is low enough that contact between particles is limited, the hardness evolution would reflect only the hardening behavior of the soft matrix, in this case no stage B and C are observed.

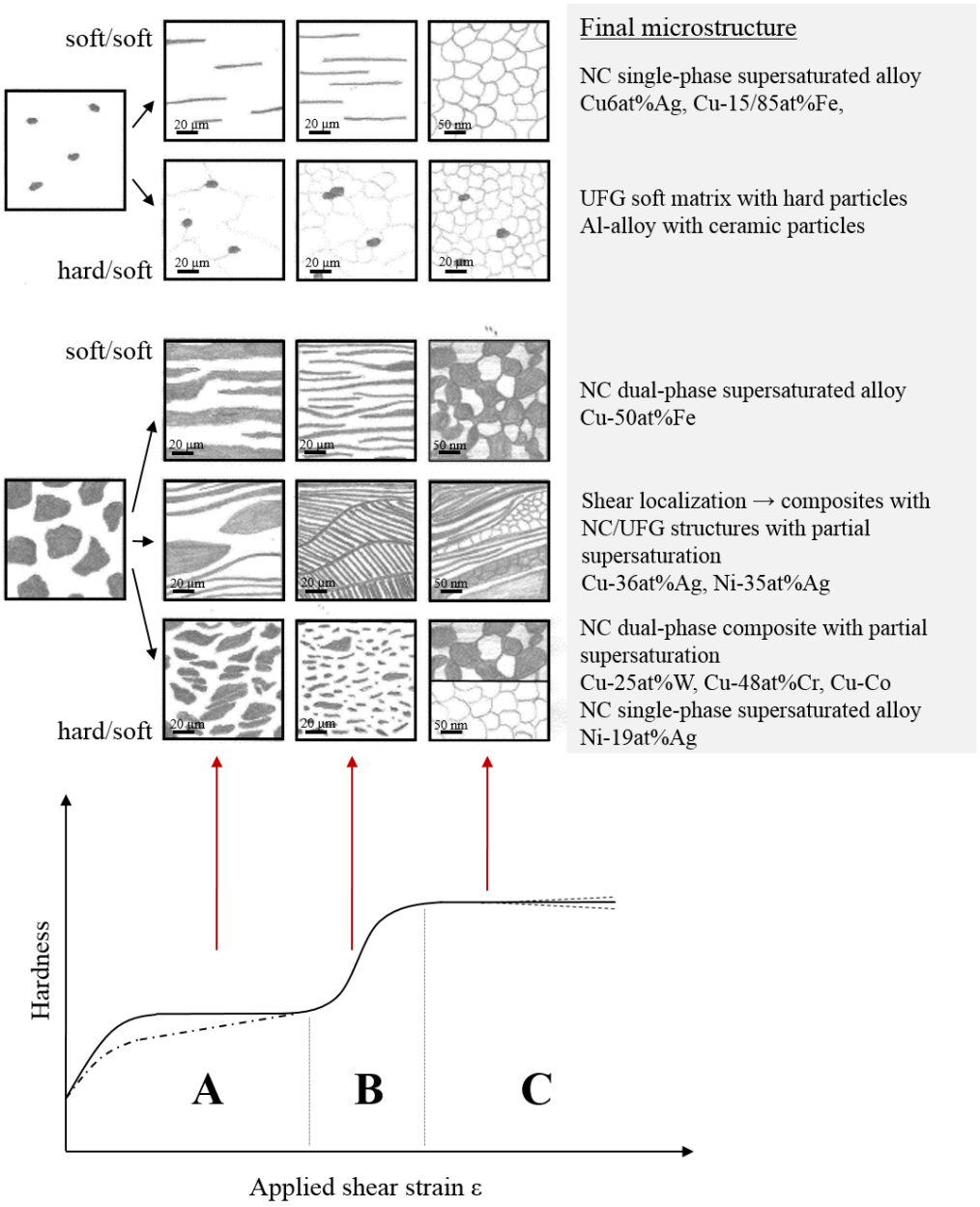

Fig. 13: Schematic of the microstructural and hardness evolution as a function of applied strain depending on hardness differences and volume fraction of the present phases.

The deformation behavior is dependent on the volume fraction of the hard phase, as observed in the Ni-Ag and the Cu-Co system. Comparing the microstructures of Ni-35at%Ag and Ni-69at%Ag at the same applied strain (see Figure VI.8c and e) reveals that the refinement process of the Ni particles is much slower in the Ag-rich sample. However, the volume fraction of Ni in both cases is too high, that they could flow unhindered in the Ag matrix. Therefore a refinement of the Ni particles takes place, which again leads to a strong hardness increase (stage B in the schematic hardness plot) before a constant hardness level is reached (saturation regime C). However, even at very high strains small Ni particles are retained and localized deformation mechanisms like shear banding lead to inhomogeneous microstructures. Similar observations are made in the Cu-Co system. The Cu-26at%Co composite requires higher applied strains than the Cu-54 and 76at% Co composites to homogenize, and even at the highest applied strain level Co particles are retained. Nevertheless mixing occurs in the Cu-26at%Co composite and a homogenous alloy could be obtained, if the strain is further increased. In contrast if the minor phase has a similar hardness than the matrix, both phases will co-deform, as for example in Cu-6at%Ag (see Figure VI.6) and Cu-15 and 85at%Fe, see schematic in Figure VI.13. In the individual phases, the respective UFG saturation microstructures are formed in the beginning (regime A in the hardness plot). The minor phase is continuously thinned until it will dissolve (stage B) and a single-phase NC microstructure is formed (stage C).

When the hard phase has a large volume fraction, as for example in Cu-25at%W (see Figure VI.2), Cu-48at%Cr, Ni-6 and 19at%Ag and Cu-54 and 76at%Co (see Figure VI.10), both phases have to deform, although it is assumed that the soft phase will carry more deformation. The harder phase (W, Cr, Ni and Co) is refined continuously by elongation, repeated fractures or necking and fracture. The soft phase (Cu and Ag) forms its respective UFG saturation microstructure in the very beginning of the HPT process and then plastically deforms by dislocation motion and restores the microstructure by grain boundary motion [40]. During continuing deformation both phases are further thinned, the hardness evolution in some cases shows first a slight hardness increase, see for example Cu-54at%Co (hardness plot in Figure VI.12), as long as the hard phase is still in micrometer regime. Then a strong hardness increase is observed (regime B), when both phases undergo severe refinement. In Cu-25at%W and Cu-47at%Cr no full mixing was observed, and the final NC microstructure obtained in regime C is composed of supersaturated Cu and Cr/W phase. In Ni-19at%Ag, the Ni volume fraction is high enough that all of the soft phase is solved in the hard phase (compared to Ni-35 and 69at%Ag). Hence, the final structure is a NC single-phase supersaturated solid solution.

In the Cu-36at%Ag and the Cu-50at%Fe composites the constituent phases have similar volume fractions and the hardness difference is not very pronounced. In the beginning of the HPT process (regime A) both phases reach their respective saturation grain size and hardness. In the Cu-Fe system, although co-deformation takes place, no supersaturated single-phase alloy is obtained in the medium composition range, instead a composite with partially supersaturated fcc Cu and bcc Fe is obtained, as in Cu-25at%W and Cu-47at%Cr. The Cu-36at%Ag composite behaves differently, see schematic in Figure VI.13. In the beginning (regime A) both phases arrange in a lamellar structure with UFG structures inside the lamellae as in Cu-Fe composites. When a critical strain is reached, strong shear localization occurred, which was also observed in the Ni-35at%Ag composite. In the Cu-36at%Ag composite a supersaturated phase was generated inside the shear bands, which had the global composition of the composite. The steady formation of new shear bands and connected lamella rotation (see Figure VI.6e) results in an accelerated refinement of the composite accompanied by a strong hardening (stage B). Because the shear bands cut through the lamellar regions under certain angles, the deformation is similar as in a two-step HPT process. In the saturation regime C the deformation is mainly carried by shear bands, preventing full supersaturation of the composites. In Cu-36at%Ag dual-

phase lamellar regions are retained even at the highest applied strains. In Ni-35at%Ag strong inhomogeneities in the microstructure are observed, see Figure VI.8d, reaching from pure Ni and Ag regions with UFG structures to nanocomposite regions with partial supersaturation.

In all composites a strong hardness increase is observed due to a refinement to a NC microstructure, as summarized in Table IV.1. The deformation mechanisms, which maintain the microstructure in the saturation regime are not clearly identified. In the case of single-phase supersaturated solid solutions, as for example in Ni-6 and 19at%Ag, Cu-6at%Ag and Cu-15 and 85at%Fe, it can be assumed that the same mechanisms operate as in pure metals or other single-phase alloys [40]. In the alloys with medium compositions in the fcc-fcc systems (Cu-Ag and Ni-Ag), only few shear bands carry most of the imposed strain. When a partially supersaturated composite is formed (as for example in Cu-W, Cu-Cr and Cu-Fe), a possible mechanism is an equilibrium state between dissolution of atoms by deformation and decomposition by thermal diffusion. However, the deformation processes to realize the high shear strains are not understood.

IV.6.3 Heat of mixing

Table IV.2 lists the heat of mixing data available in literature and the atomic radius mismatch for each system. The system with the largest positive heat of mixing, Cu-W (ΔH_{mix} of 35kJ/mol) has indeed the lowest solubility limit. Also the Ni-Ag and Cu-Cr systems follow this trend with ΔH_{mix} of 23 and 20 kJ/mol, respectively, they have maximum solubilities of less than 20at%. Interestingly, the Cu-Ag system, which has the lowest heat of mixing of all studied systems, does not show a higher solubility limit. It is even lower than in Cu-Fe or Cu-Co system. As shown in the previous section, strong strain localization in shear bands leads to the formation of a supersaturated solid solution with 36 at% Ag solved in Cu, which corresponds to the global composition of the alloy, but the absent deformation of the remaining lamellar matrix results in a retardation of supersaturation process. The Cu-based fcc-bcc composites could give evidence if the heat of mixing or hardness differences of the present phases governs the mixing process, however, the level of the heat of mixing correlates with the hardness difference (Cu-W has the highest heat of mixing and hardness difference, followed by Cu-Cr and Cu-Fe). Therefore it cannot be concluded which factor defines the maximum achievable solubility. However, in particular the Cu-Ag system demonstrates that a low positive heat of mixing is no indicator for a successful supersaturation to a single-phase alloy during HPT processing. It seems that the deformation behavior influences the maximum achievable degree of supersaturation in the Cu-Ag system, by limiting homogenous deformation of the composites.

IV.7 Remarks on thermal stability

In general, the metastable supersaturated phases are expected to undergo phase separation upon annealing, which is indeed observed above certain annealing temperatures. In the Cu-47at%Cr composite the deformed microstructure is composed of nanometer sized grains (10 to 20 nm) with partial supersaturation (~15at% Cu is solved in the Cr phase and ~2at% Cr in Cu phase). During annealing at 400°C complete phase decomposition occurs and a nanocomposite with pure Cu and Cr grains evolves, in which grains of the same phase are isolated by grains of the other phase(for details see reference [55]). The hardness after annealing for 30 min is stable up to 600 °C, at annealing temperatures between 200 and 400 °C even a hardness increase is observed (Figure VI.14a). In immiscible systems this phenomenon is a common feature (also documented in Cu-Fe [61], Cu-Ag [49] and Cu-Co [52]), however the details of this hardening during annealing are still unclear.

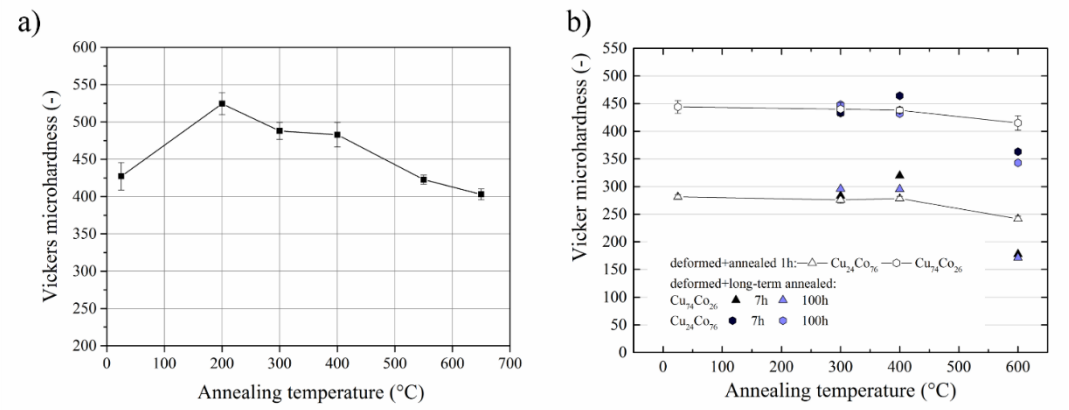

Fig. 14: Hardness as a funtion of annealing temperature: a) for the Cu-47at%Cr composite annealed at different temperatures for 30 min and b) for the Cu-26 and 76at%Co composites annealed up to 600°C for annealing times of 1 to 100 h.

The supersaturated Cu-26 and 76at%Co alloys were annealed for 1 h in air at 300, 400 and 600 °C, corresponding to ~35, 40 and 52% of the melting temperature and additionally, to study the long-term stability, for 7 and 100 h, see Figure VI.14b. At the lowest annealing temperature of 300 °C no significant change in hardness was observed independent of annealing time. A drop in hardness is not observed until the highest annealing temperature of 600 °C is reached. In the Co-rich composite the hardness drops after 7 h annealing treatments, and after 100 h a further slight decrease is observed. In the Cu-26at%Co composite the hardness decreases after 7 h annealing and then keeps a constant level. The thermal stability and decomposition behavior was studied in detail for the Cu26at%Co composite [52]. The grain size of this composite is about ~100 nm. During annealing at medium temperatures (400°C), a process similar to spinodal decomposition presumably takes place. This is indicated by chemical modulations inside the grains in form of an array of alternating Cu and Co, which was analyzed by EELS and APT, for details see reference [52]. This type of decomposition is observed inside the grains because diffusion distances are very limited at 400 °C and beneath and the grain size is relatively large (compared to the other investigated systems, which all exhibit grain sizes well below 50 nm. The formed structures of phase-separated Cu and Co regions in the nanometer regime, together with Cu and Co particles, which formed at grain boundaries, show an extraordinary high long-term stability. In summary, the nanocomposites formed after annealing exhibit a high resistance to grain growth. These nanostructures result either from spinodal decomposition in composites with relatively large grains (Cu-Co), or in composites with grain sizes below 50 nm from decomposition of the partially supersaturated grains.

IV.8 Summary and Conclusions

In summary, the investigated material systems can be divided into three groups with respect to their deformation behavior. On the one hand composites, which exhibit strong hardness differences of the constituent phases, the Cu-W, Cu-Cr, Cu-Co and the Ni-Ag systems. The structural refinement during HPT processing of these types of composites is characterized by strong plastic deformation in the soft phase, while the fragmentation of the hard phase is governed by elongation and repeated fracturing of the particles. If the volume fraction of the hard phase is high enough, homogenization of the composite could be obtained. The final microstructures are either nanocomposites with partial supersaturation of the phases

or full supersaturation with a single-phase structure was achieved. When the hard phase is present in a low volume fraction, the effect of strong strain localization in the soft phase is very pronounced, leading to a retardation of the refinement process of the hard phase, as seen in Cu-26at%Co. On the other hand, if the hardness difference between the phases is not pronounced, as in Cu-Fe and Cu-Ag, the individual phases co-deform to lamellar structures. If one of the phases is existent in a minor volume fraction, homogenous deformation leads to a single-phase supersaturated solid solution. If the phases exist in nearly equal volume fraction, as in the Cu50at%Fe composite, a nanocomposite composed of a Cu-rich and a Fe-rich phase develops. And third, systems which deformed mainly by shear banding, as observed in the Cu-36at%Ag and the Ni-35at%Ag composites. The localized deformation prevented homogenization of the composite and inhomogeneous structures with partial supersaturation are obtained.

From the studies conducted so far it seems that either the level of the positive heat of mixing, triggered mainly by lattice structure and atomic radius differences, or strong variations in the mechanical properties limits the degree of supersaturation in the fcc-bcc material systems. The fcc-fcc systems are prone to shear banding in medium compositions, preventing homogenization of the composites. In the Cu-Ag system in literature complete supersaturation was shown also by HPT processing in medium compositions [76], it is therefore assumed if shear banding can be suppressed, a full mixture of Cu and Ag can be obtained.

The results indicate that the fundamental mixing mechanism leading to supersaturation is possibly not the same in the different analyzed materials systems. In the composites with a hard and a soft phase(for example Cu-Co), an abrasion-like process is proposed, inducing a mixing already at relatively low applied strains. The subsequent final mixing at high strains might be realized by other mechanisms (e.g., dislocation shuffling). This was studied in detail in the Cu-Co system. On the other hand in the Cu-Ag system with two soft phases, the mixing behavior in the lamellar nanocomposites indicates a mixing process by dislocations crossing phase boundaries, triggered by a critical phase dimension. However, no explicit prediction on the degree of supersaturation in a certain material system during HPT deformation can be made on the simple basis of the materials properties. Detailed studies on the deformation behavior at different stages of deformation are inevitable, especially considering the formation of shear bands and the different capabilities for plastic deformation of the individual phases.

Acknowledgement

Funding of this work has been provided by the European Research Council under ERC Grant Agreement No. 340185 USMS and by the Austrian Science Fund (FWF): J3468-N20.

References

[1] Y. Ogino, T. Yamasaki, S. Murayama, R. Sakai, *J. Non. Cryst. Solids* **1990**, *117/118*, 737.

[2] E. Gaffet, C. Louison, M. Harmelin, F. Faudot, *Mater. Sci. Eng. A* **1991**, *134*, 1380.

[3] C. Gente, M. Oehring, R. Bormann, *Phys. Rev. B* **1993**, *48*, 244.

[4] K. Uenishi, K.F. Kobayashi, K.N. Ishihara, P.H. Shingu, *Mater. Sci. Eng. A* **1991**, *134*, 1342.

[5] R. Najafabadi, D.J. Srolovitz, E. Ma, M. Atzmon, *J. Appl. Phys.* **1993**, *74*, 3144.

[6] Z.Q. Li, H. Shen, L. Chen, Y. Li, B. Günther, *Philos. Mag.* **1995**, *72*, 1485.

[7] J. Xu, U. Herr, T. Klassen, R.S. Averback, **1996**, *79*, 3935.

[8] A.R. Yavari, P.J. Desre, T. Benameur, *Phys. Rev. Lett.* **1992**, *68*, 2235.

[9] J. Eckert, J.C. Holzer, C.E. Krill III, W.L. Johnson, *J. Appl. Phys.* **1993**, *73*, 2794.

[10] J. Eckert, J.C. Holzer, W.L. Johnson, *J. Appl. Phys.* **1993**, *73 (1)*, 131.

[11] E. Gaffet, M. Harmelin, F. Faudot, *J. Alloys Compd.* **1993**, *194*, 23.

[12] J. Kuyama, H. Inui, S. Imaoka, S. Nasu, K.N. Ishihara, P.H. Shingu, *Jpn. J. Appl. Phys.* **1991**, *30*, 854.

[13] C. Suryanarayana, *Prog. Mater. Sci.* **2001**, *46*, 1.

[14] Y. Li, D. Raabe, M. Herbig, P.P. Choi, S. Goto, A. Kostka, H. Yarita, C. Borchers, R. Kirchheim, *Phys. Rev. Lett.* **2014**, *113*, 1.

[15] J.D. Verhoeven, W.A. Spitzig, L.L. Jones, H.L. Downing, C.L. Trybus, E.D. Gibson, L.S. Chumbley, L.G. Fritzemeier, G.D. Schnittgrund, *J. Mater. Eng.* **1990**, *22*, 127.

[16] J. Bevk, J.P. Harbison, J.L. Bell, *J. Appl. Phys.* **1978**, *49*, 6031.

[17] J.D. Embury, M.A. Hill, W.A. Spitzig, *MRS* **1993**, 57.

[18] J. Freudenberger, N. Kozlova, A. Gaganov, L. Schultz, H. Witte, H. Jones, *Cryogenics (Guildf).* **2006**, *46*, 724.

[19] D. Raabe, K. Miyake, H. Takahara, *Mater. Sci. Eng. A* **2000**, *291*, 186.

[20] P. Gorria, D. Martínez-Blanco, J.A. Blanco, M.J. Pérez, A. Hernando, L.F. Barquín, R.I. Smith, *Phys. Rev. B - Condens. Matter Mater. Phys.* **2005**, *72*, 1.

[21] P. Gorria, D. Martínez-Blanco, R. Iglesias, S.L. Palacios, M.J. Pérez, J.A. Blanco, L. Fernández Barquín, A. Hernando, M.A. González, *J. Magn. Magn. Mater.* **2006**, *300*, 229.

[22] A.E. Berkowitz, J.R. Mitchell, M.J. Carey, A.P. Young, S. Zhang, F.E. Spada, F.T. Parker, A. Hutten, G. Thomas, *Phys. Rev. Lett.* **1992**, *68*, 3745.

[23] J. Wecker, R. Von Helmolt, L. Schultz, K. Samwer, *Appl. Phys. Lett.* **1993**, *62*, 1985.

[24] X. Sauvage, F. Wetscher, P. Pareige, *Acta Mater.* **2005**, *53*, 2127.

[25] X. Sauvage, R. Pippan, *Mater. Sci. Eng. A* **2005**, *410-411*, 345.

[26] S. Ohsaki, S. Kato, N. Tsuji, T. Ohkubo, K. Hono, *Acta Mater.* **2007**, *55*, 2885.

[27] X. Sauvage, P. Jessner, F. Vurpillot, R. Pippan, *Scr. Mater.* **2008**, *58*, 1125.

[28] X. Quelennec, A. Menand, J.M. Le Breton, R. Pippan, X. Sauvage, *Philos. Mag.* **2010**, *90*, 1179.

[29] H.W. Sheng, G. Wilde, E. Ma, *Acta Mater.* **2002**, *50*, 475.

[30] E.H. Ekiz, T.G. Lach, R.S. Averback, N.A. Mara, I.J. Beyerlein, M. Pouryazdan, H. Hahn, P. Bellon, *Acta Mater.* **2014**, *72*, 178.

[31] M. Wang, N.Q. Vo, M. Campion, T.D. Nguyen, D. Setman, S. Dillon, P. Bellon, R.S. Averback, *Acta Mater.* **2014**, *66*, 1.

[32] S.N. Arshad, T.G. Lach, M. Pouryazdan, H. Hahn, P. Bellon, S.J. Dillon, R.S. Averback, *Scr. Mater.* **2013**, *68*, 215.

[33] P. Bellon, R.S. Averback, S. Odunuga, Y. Li, P. Krasnochtchekov, A. Caro, *Phys. Rev. Lett.* **2007**, *99*, 110602.

[34] S. Odunuga, Y. Li, P. Krasnochtchekov, P. Bellon, R.S. Averback, *Phys. Rev. Lett.* **2005**, *95*, 045901.

[35] D. Raabe, S. Ohsaki, K. Hono, *Acta Mater.* **2009**, *57*, 5254.

[36] K. Uenishi, K.F. Kobayashi, **1991**, *134*, 1342.

[37] E. Ma, J.H. He, P.J. Schilling, *Phys. Rev. B* **1997**, *55*, 5542.

[38] P. Bellon, R.S. Averback, *Phys. Rev. Lett.* **1995**, *74*, 1819.

[39] R. Pippan, S. Scheriau, A. Taylor, M. Hafok, A. Hohenwarter, A. Bachmaier, *Annu. Rev. Mater. Res.* **2010**, *40*, 319.

[40] O. Renk, A. Hohenwarter, S. Wurster, R. Pippan, *Acta Mater.* **2014**, *77*, 401.

[41] M. Hafok, R. Pippan, *Mater. Sci. Forum* **2007**, *550*, 277.

[42] B. Yang, H. Vehoff, A. Hohenwarter, M. Hafok, R. Pippan, *Scr. Mater.* **2008**, *58*, 790.

[43] R. Pippan, F. Wetscher, M. Hafok, A. Vorhauer, I. Sabirov, *Adv. Eng. Mater.* **2006**, *8*, 1046.

[44] A. Bachmaier, M. Hafok, R. Pippan, *Mater. Trans.* **2010**, *51*, 8.

[45] A. Bachmaier, M. Kerber, D. Setman, R. Pippan, *Acta Mater.* **2012**, *60*, 860.

[46] A. Bachmaier, R. Pippan, *Int. Mater. Rev.* **2013**, *58*, 41.

[47] A. Hohenwarter, A. Bachmaier, B. Gludovatz, S. Scheriau, R. Pippan, *Int. J. Mat. Res.* **2009**, *100*, 1653.

[48] H.P. Stüwe, *Adv. Eng. Mater.* **2003**, *5*, 291.

[49] K.S. Kormout, B. Yang, R. Pippan, *IOP Conf. Ser. Mater. Sci. Eng.* **2014**, *63*, 012092.

[50] K.S. Kormout, B. Yang, R. Pippan, *Adv. Eng. Mater.* **2015**, 1828.

[51] A. Bachmaier, C. Motz, *Mater. Sci. Eng. A* **2015**, *624*, 41.

[52] A. Bachmaier, M. Pfaff, M. Stolpe, H. Aboulfadl, C. Motz, *Acta Mater.* **2015**, *96*, 269.

[53] A. Bachmaier, H. Aboulfadl, M. Pfaff, F. Mücklich, C. Motz, *Mater. Charact.* **2015**, *100*, 178.

[54] A. Bachmaier, J. Schmauch, H. Aboulfadl, A. Verch, C. Motz, *Acta Mater.* **2016**, *115*, 333.

[55] A. Bachmaier, G.B. Rathmayr, M. Bartosik, D. Apel, Z. Zhang, R. Pippan, *Acta Mater.* **2014**, *69*, 301.

[56] A. Bachmaier, J. Keckes, K.S. Kormout, R. Pippan, *Philos. Mag. Lett.* **2013**.

[57] I. Sabirov, R. Pippan, *Scr. Mater.* **2005**, *52*, 1293.

[58] I. Sabirov, R. Pippan, *Mater. Charact.* **2007**, *58*, 848.

[59] D. Edwards, I. Sabirov, W. Sigle, R. Pippan, *Philos. Mag.* **2012**, *92*, 4151.

[60] F.T.N. Vüllers, R. Spolenak, **2015**, *99*, 213.

[61] A. Bachmaier, M. Kerber, D. Setman, R. Pippan, *Acta Mater.* **2012**, *60*, 860.

[62] K. Edalati, S. Toh, M. Arita, M. Watanabe, Z. Horita, *Appl. Phys. Lett.* **2013**, *102*, 1.

[63] E. Ma, *Prog. Mater. Sci.* **2005**, *50*, 413.

[64] J. Eckert, J.C. Holzer, C.E. Krill, W.L. Johnson, *J. Appl. Phys.* **1993**, *73*, 2794.

[65] T.D. Shen, C.C. Koch, *Acta Mater.* **1996**, *44*, 753.

[66] X. Quelennec, A. Menand, J.M. Le Breton, R. Pippan, X. Sauvage, **2010**, 1179.

[67] Y. Ashkenazy, N.Q. Vo, D. Schwen, R.S. Averback, P. Bellon, *Acta Mater.* **2012**, *60*, 984.

[68] N.Q. Vo, J. Zhou, Y. Ashkenazy, D. Schwen, R.S. Averback, P. Bellon, *Jom* **2013**, *65*, 382.

[69] C.. Sinclair, J.. Embury, G.. Weatherly, *Mater. Sci. Eng. A* **1999**, *272*, 90.

[70] N.A. Mara, I.J. Beyerlein, *J. Mater. Sci.* **2014**, *49*, 6497.

[71] A. Misra, R.G. Hoagland, *J. Mater. Sci.* **2007**, *42*, 1765.

[72] G. Veltl, B. Scholz, H.D. Kunze, *Mater. Sci. Eng. A* **1991**, *134*, 1410.

[73] R.Z. Valiev, *Nat. Mater.* **2004**, *3*, 511.

[74] E. Ma, H.W. Sheng, J.H. He, P.J. Schilling, **2000**, *286*, 48.

[75] I. Sabirov, O. Kolednik, R. Pippan, *Metall. Mater. Trans. A* **2005**, *36*, 2861.

[76] M. Pouryazdan, D. Schwen, D. Wang, T. Scherer, H. Hahn, R.S. Averback, P. Bellon, *Phys. Rev. B* **2012**, *86*, 144302.

V Effect of processing temperature on deformation and supersaturation behavior during severe plastic deformation of Cu-Ag composites

K.S. Kormout[1], P. Ghosh[1], R. Pippan[1]

[1]Erich Schmid Institute of Materials Science, Austrian Academy of Sciences

Abstract. The key factors influencing deformation-induced supersaturation in the Cu-Ag system are the processing temperature, the volume fractions of the phases and the total applied strain. In the present study a systematic variation of these parameters during severe plastic deformation is used to analyze their effect on the degree of supersaturation by synchrotron X-Ray measurements and make correlations to microstructural changes by transmission electron microscopy. For this purpose high-pressure torsion processing of initial micrometer-sized powder blends (Cu-6/37/84at%Ag) is used. It appears that there is a transition from complete supersaturation to complete phase separation with increasing processing temperature. In the saturation regime of hardness evolution the critical temperature for full supersaturation strongly depends on the composition. In composites with low and high Ag content single-phase alloys are obtained up to processing temperatures of 100 °C after applied strains of about γ~780. In the medium composition range strain localization in shear bands prevents fully supersaturation at room temperature deformation. Only in regions deformed by shear bands a complete single-phase supersaturated solid solution is obtained, while the lamellar matrix remains dual-phase. By lowering the processing temperature to liquid nitrogen temperature a homogenous single-phase alloy is also attainable in medium compositions. The present results unravel a clear correlation between dominating deformation mechanisms and strain-induced supersaturation.

V.1 Introduction

Although Cu and Ag partly fulfill the well-known Hume-Rothery rules, they show a eutectic phase diagram with a solubility limit well below 1 at% at room temperature and a positive heat of mixing, which can be mainly attributed to the lattice mismatch of about 12%. Nevertheless, by forcing the metals into a non-equilibrium state using certain production techniques, intermixing of Cu and Ag can be realized. Rapid quenching, film deposition and severe plastic deformation (SPD) proved to form supersaturated solid solutions in several immiscible systems. The phenomenon of deformation-induced mixing was extensively studied in ball-milling experiments, in which the solubilities were extended or even fully supersaturated solid solutions were obtained. It was shown that in systems with low positive heat of mixing, as for example Cu-Ag and Cu- solid solutions are easily reached over the whole composition range [1,2]. In contrast in systems with high positive heat of mixing, such as Ni-Ag or Ag-Fe, only very limited extended solubilities could be obtained [3,4]. The cause of this effect, either the positive heat of mixing or the strength differences of the constituent phases, possibly accompanied by strain localization, is still under debate [5].

Due to the loosely defined processing parameters during ball-milling other SPD techniques such as accumulative roll bonding (ARB) or high-pressure torsion (HPT) are widely used nowadays to study deformation-induced mixing. In general, similar observations are made concerning the degree of supersaturation in different material systems. Additionally, SPD techniques are feasible to study the basic deformation mechanisms in immiscible composites, which indirectly influence the degree supersaturation. For example in studies on Cu-W and Cu-Cr alloys it appeared that the deformation behavior is governed by strain localization of the Cu phase and the fragmentation of the harder W and Cr phase so that SPD is realized mainly by elongation and repeated fracturing of the particles [6,7]. The supersaturation in these systems was found, however, to be very limited. On the other hand, in studies on Cu-Ag composites, where the constituent phases exhibit similar mechanical properties, it was shown that during HPT deformation at room temperature (RT) a homogenization and complete supersaturation in the medium composition range is prevented by pronounced shear band formation. At low and high Ag content instead a more homogenous co-deformation led to single-phase alloys in a supersaturated state. Along with the mechanical properties and volume fraction of the constituent phases the processing temperature is another important parameter influencing the deformation behavior and the supersaturation process.

The present study focuses on the correlation between the basic deformation mechanisms and the process of deformation-induced supersaturation in the Cu-Ag system. For this purpose a systematic variation of the key parameters, namely composition and temperature, during HPT deformation was used to study their effect on the degree of supersaturation by synchrotron X-Ray measurements and make correlations to microstructural changes by transmission electron microscopy (TEM).

V.2 Experimental

As initial material commercially pure powders of Cu and Ag (99.97%, 625 mesh and 99.99%, 500 mesh, from Alfa Aesar) were used and mixed to obtain the desired compositions Cu-6/37/84at%Ag. The powder blends were filled directly into the steel anvils, compacted and subsequently deformed in the HPT tool. The HPT processing was performed with an applied pressure of 7.5 GPa and a rotational speed between 0.2 and 0.6 rot/min at liquid nitrogen temperature, room temperature (RT), 100°C, 200°C and 300°C. Samples were deformed between 5 and 100 rotations, the applied shear strain γ during HPT is calculated with

$$\gamma = \frac{2\pi r}{t} n, \qquad \text{(V.1)}$$

where r is the radius, t the thickness of the disk and n is the number of rotations. The produced samples are disks with a diameter of 8 mm and a thickness between 0.45 and 0.6 mm. Information on the used HPT process can be found elsewhere [8]. Due to measurement uncertainty in the sample preparation process regarding exact sample thickness and radial position of the investigated area, for the calculated shear strains only approximate values are given.

The microstructures evolving with different processing parameters were studied with a Zeiss Leo 1525 scanning electron microscope (SEM) and a Philips CM12 operated at 120 kV and an image-side C_S-corrected JEOL JEM-2100F operated at 200 kV transmission electron microscope (TEM).

The TEM sample preparation was conducted after a standard procedure with dimple grinding and subsequent ion milling. Samples were cooled with liquid nitrogen during ion milling to avoid any heating.

Synchrotron X-ray experiments were performed at the PETRA III P07 beamline at the DESY Photon Science facility (Hamburg). The diffraction measurement was conducted on samples deformed to $\gamma \sim 1887$ using a beam energy of 111 keV. The primary and secondary slit of 0.5×0.5 mm and 0.7×0.7 mm, respectively were used to improve the microstructure statistics. The measured transmission diffraction pattern was analyzed with FIT 2D software [9].

Vickers hardness measurements were performed with a Buehler Micromet 5100 using a maximum load of 500 gf along the cross section of the HPT disk in distances of 250 µm between each indent.

V.3 Results and Discussion

V.3.1 Microstructural and hardness evolution during HPT

The hardness evolution as a function of applied strain for the Cu-37at%Ag composite deformed at LN temperature, RT and 200°C is displayed in Figure V.1a revealing the characteristic profiles with three distinct stages, labeled as regime A, B and C, as usually observed in binary immiscible composites [10,11]. The hardness evolution during RT deformation of Cu-6/16/64/84at%Ag composites can be found in reference [12]. In the present Cu-37at%Ag composite the fluctuations in hardness are larger at RT and 200 °C than at LN processed composites, particularly in regime C. Figure V.1b displays the hardness values from regime C, averaged for $\gamma > 1000$, of the different processing temperatures. The obtained mean hardness values measured at RT exhibit only minor differences between samples processed at LN and 200 °C until at 300 °C a distinct drop in hardness is observed. The microstructural changes in the three stages leading to different saturation microstructures will be described first for RT deformation for Cu-6 and 37at%Ag composites and then for the Cu-37at%Ag composite for varying processing temperatures.

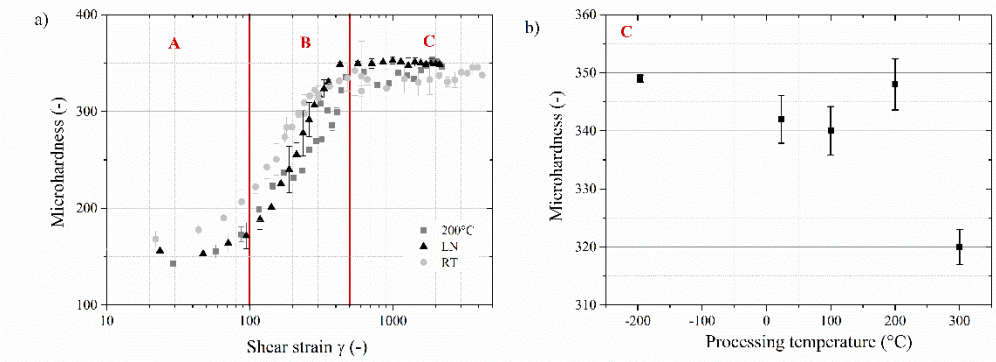

Figure V.1: Vickers microhardness for the Cu-37at%Ag composite. a) Plotted as a function of applied strain for processing at LN, RT and 200 °C. b) The saturation hardness as a function of processing temperature. (As an error the standard deviation is inserted.)

Figure V.2 presents SEM micrographs of the microstructural evolution for the Cu-6 and 37at%Ag composite with increasing applied strain deformed at RT. The Cu lamellae appear in dark and the Ag in bright contrast. In the Cu-6at%Ag composite the Ag phase was successively refined from the micrometer range after compaction to below 500 nm at γ~190 (Figure V.2a). Further increase in strain to γ~380 led to continuous thinning of the Ag phase with a fairly uniform distribution in the Cu matrix, see Figure V.2b, which finally results in a saturation of microstructural features and hardness. At applied strains of γ~1900 a homogeneous nanocrystalline elongated microstructure was formed, see Figure V.2c, and a single-phase supersaturated state was reached, as will be shown in synchrotron XRD measurements in the last section. For the Cu-84t%Ag a comparable deformation behavior was found and thus not explicitly shown.

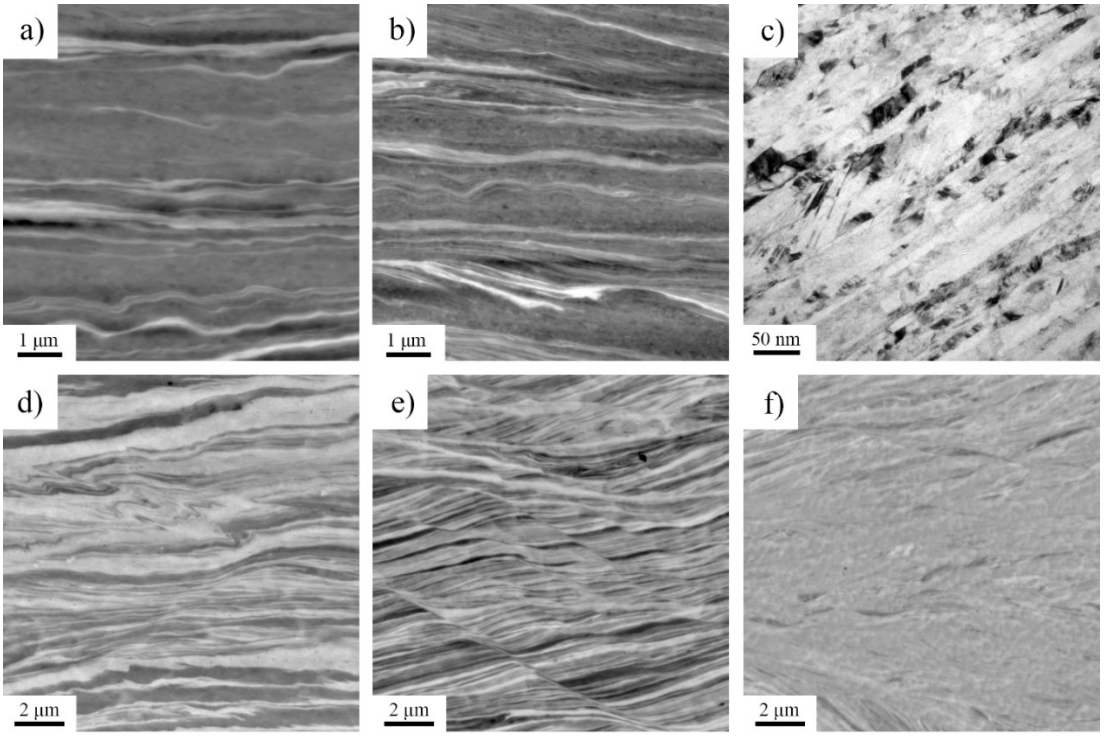

Figure V.2: SEM micrographs of the Cu-6at%Ag composite deformed at RT in radial direction for applied strains of a) γ~190 showing a lamellar composite with the Ag phase (bright contrast) uniformly distributed within the Cu matrix (dark contrast), b) γ~380 showing further refinement of the lamellar composite and c) γ~1900 showing the nanocrystalline saturation microstructure. SEM micrographs of the Cu-37at%Ag composite at d) γ~190, e) γ~380 and f) γ~1900.

A different microstructural evolution was observed during RT processing of the Cu-37at%Ag composite. Co-deformation of the lamellar structure as in Cu-6at%Ag occurred only up to strains of γ~190. At this strain level shear band formation set in (see Figure V.2d) and by increasing the applied strain new shear bands were formed continuously (Figure V.2e). Due to the localized deformation even at the highest applied strain levels no homogeneous microstructure was obtained, see Figure V.2f, and the final composite is composed of nano-lamellar dual-phase regions and homogeneous regions generated by shear bands.

Additionally, microstructural investigations were conducted on the Cu-37at%Ag composite deformed at LN temperature and 200 °C and compared to the RT-behavior. At an equally applied strain, γ~380, samples processed at LN (Figure V.3a) and RT (Figure V.3b) have similar microstructures consisting of shear bands embedded in lamellar regions as main features. At RT shear bands showed a regular pattern, running through the whole sample and thereby causing a rotation of the lamellae out of the HPT shear plane. At LN temperature the shear bands are not as regularly distributed. At a deformation temperature of 200 °C a uniform lamellar structure, Figure V.3c, inclined to the HPT shear plane about ~11° was formed without the occurrence of shear bands.

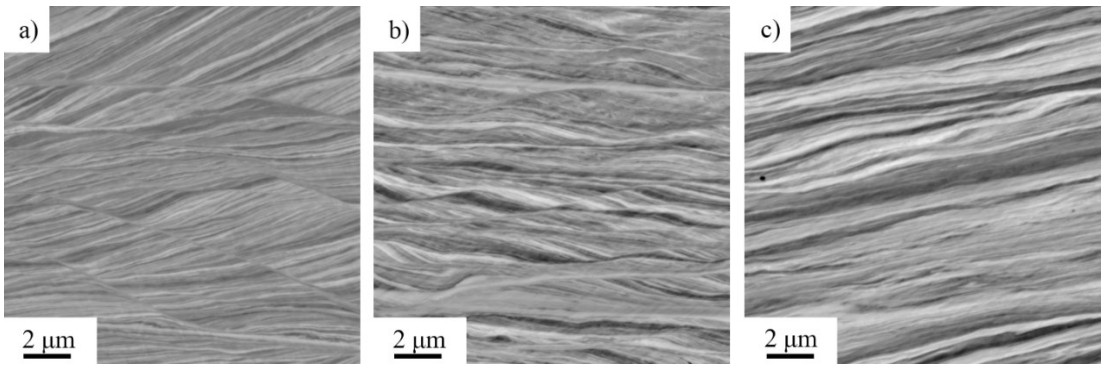

Figure V.3: BSE-SEM images taken in radial direction of the Cu-37at%Ag composite at an applied strain of γ~380 for processing at a) RT, b) LN and c) 200 °C.

In contrast to RT deformation, in the LN and 200 °C deformed Cu-37at%Ag composites homogenous saturation microstructures were reached after an applied strain of γ~1900.

Further insights into the microstructure are granted by TEM-investigations (Figure V.4). At LN temperature a slightly elongated structure was obtained with a grain size well below 50 nm, see Figure V.4a. The SAD pattern showed that a complete single-phase supersaturated solid solution with a shear texture apparent from the non-uniform intensities of the diffraction rings was formed. At RT an inhomogeneous microstructure showing nano-lamellar and nanocrystalline nearly equi-axed regions, see Figure V.4b, were typical. SAD analyses demonstrated that within shear bands a supersaturated solid solution was formed, while lamellar regions retained dual-phase, as indicated in the SAD pattern in Figure V.4b. At 200°C and higher processing temperatures completely phase-separated dual-phase nanocomposites were found, see Figure V.4c. The almost defect-free grains ranging between 50 and 100 nm were slightly elongated and exhibited clearly discriminable grain boundaries.

Although in the saturation regime the Cu-37at%Ag composites deformed at LN, RT and 200 °C have distinctly different final microstructures, the obtained hardness level are very similar, see Figure V.1b. From the comparison of the TEM micrographs it becomes clear that the composite formed at 200 °C has an apparently larger grain size ranging between 50 and 100 nm than the single-phase alloy at LN with a grain size of about 20-30 nm. Although the grain size is larger in 200 °C deformed sample, other factors raise the hardness to the level of the LN processed sample. These are the high number of phase boundaries acting as barrier for dislocation and the lack of dislocation sources in the almost defect-free grains and the clear phase boundaries. Additionally, the higher number of twins raises the hardness.

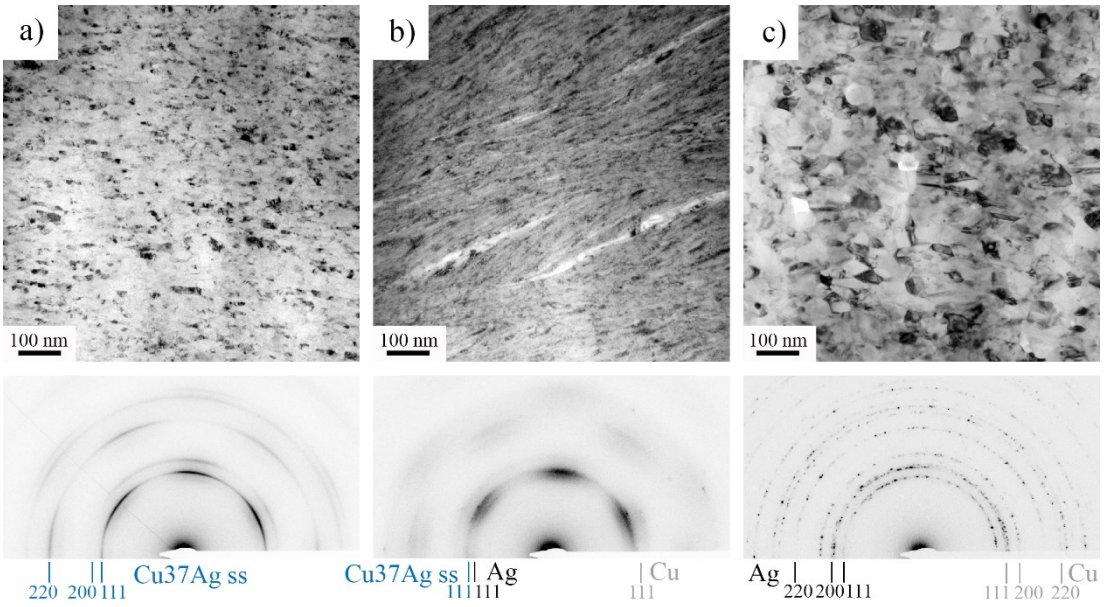

Figure V.4: TEM micrographs for the Cu-37at%Ag composite deformed to an applied strain of γ~1900 processed at a) LN, b) RT and c) 200 °C with corresponding SAD patterns, The Cu, the Ag and supersaturated phase are labeled.

A detailed comparison of the microstructures obtained for the Cu-37at%Ag composite processed at RT and at LN is presented in Figure V.5. In the micrograph of the RT deformed composite (TEM BF and DF in Figure V.5a and b) a shear band adjacent to a lamellar region is presented. Both structural configurations exhibit an extremely high defect density apparent from the strong contrast variations in BF as well as in DF images. The diffuse phase boundaries in the lamellar regions partially impede a clear distinction between single lamellae which becomes even more pronounced in the single-phase shear band regions where a clear identification of single grains is difficult, see also high resolution TEM image in Figure V.5e. Contrary, the microstructure of the LN deformed sample (TEM BF and DF in Figure V.5c and d) exhibits clearly distinguishable grains with a lower defect density and a larger grain size than in the RT deformed composite. The differences are also noticeable from the SAD patterns. As shown in Figure V.5f the LN microstructure exhibits a sharp single set of fcc rings contrary to the very broad diffraction rings in the microstructure obtained by RT processing, indicating the very small grain size and the high defect density. Additional broadening of the diffraction rings could also arise from chemical inhomogeneities in the Cu-rich, Ag-rich and supersaturated phase leading to a relatively wide variation of the lattice parameter.

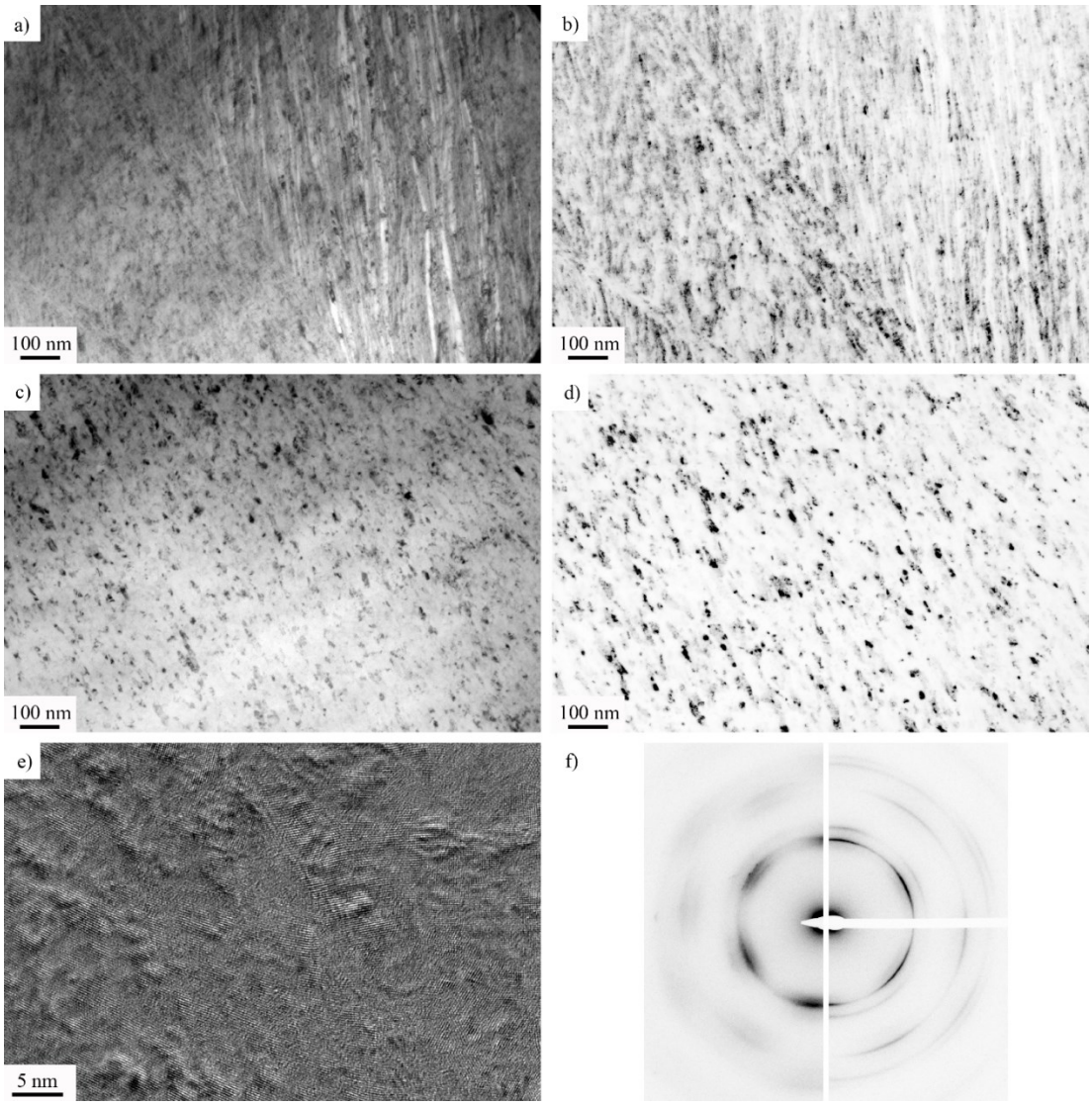

Figure V.5: TEM images of the Cu-37at%Ag composite at an applied strain of γ~1900. a) TEM BF and b) TEM DF of the RT processed sample. c) TEM BF and b) TEM DF of the LN processed samples. e) HRTEM image of the RT deformed sample. f) comparison of the SAD patterns of the LN and the RT processed samples. For the indexed patterns see Figure V.4 a and b. (For better visibility the contrast of the DF images is inverted.)

V.3.2 Local analysis of the deformation behavior

To get deeper insights into the deformation process depending on composition and temperature several local deformation experiments capable of scrutinizing the deformation mechanisms for relatively small strain increments near the saturation regime of the hardness were applied.

V.3.2.1 Regime A and B

During the HPT deformation process the initial micrometer-sized powder particles are first compressed under high pressure and then further deformed by torsional straining. Due to the relatively high ductility of Cu and Ag a lamellar arrangement of the phases is obtained directly after compaction in the HPT tool. In regime A nearly ideal co-deformation of the individual phases leads to a continuous thinning of the lamellae, although as shown in a previous study broader retained lamellae accommodate more deformation than finer lamellar regions leading to structural homogenization of the composite. Simultaneously within the phases the respective UFG saturation grain structures are formed [12]. When the lamella thicknesses approach the grain sizes inside the lamellae, denoting the beginning of regime B, further co-deformation takes place resulting in a hardness increase. With increasing strain the deformation behavior depends on the volume fraction of the constituent phases. Up to processing temperatures of 100 °C in composites with low and high Ag content, Cu-6 and 84at%Ag, further uniform deformation results in homogenous microstructures in the saturation regime C. In contrast, in Cu-37at%Ag composites the balanced volume fraction of nearly 50% of Cu and Ag leads to a nano-lamellar structure with alternating Cu and Ag phases. This structural configuration strongly restricts dislocation activity and induces shear band formation at a critical strain level of $\gamma \sim 190$, when lamella thicknesses are below 20 nm, for a detailed analysis of shear band formation and propagation see reference [13]. At higher deformation temperatures no shear band formation occurred irrespective of composition and applied strain. The obtained saturation microstructure is composed of separate Cu and Ag grains and is presumably generated by necking and fragmentation of the lamellae.

Interestingly, in the Cu-37at%Ag composite deformation at LN temperature is realized by shear bands as well, but in this case leads to a complete single-phase alloy compared to RT deformation where a multi-phase structure consisting of Cu-rich, Ag-rich and a supersaturated Cu-37at%Ag phase is reached. To identify the differences between shear band formation at RT and LN leading to distinctively different microstructures, additional experiments at RT and LN and a combination of RT deformation followed by LN processing subjected to the same accumulated strain was performed. RT processing did not result in pronounced further refinement (compare Figure V.3a with Figure V.6a). In contrast, at LN a much stronger refinement took place towards a homogenous microstructure with increasing strain (compare Figure V.3a with V.6b). By changing the processing temperature from RT to LN, as shown in Figure 6c for a sample processed for $\gamma \sim 380$ at RT and subsequently for $\gamma \sim 190$ at LN, apparently led to stronger refinement compared to only RT deformation to the same strain.

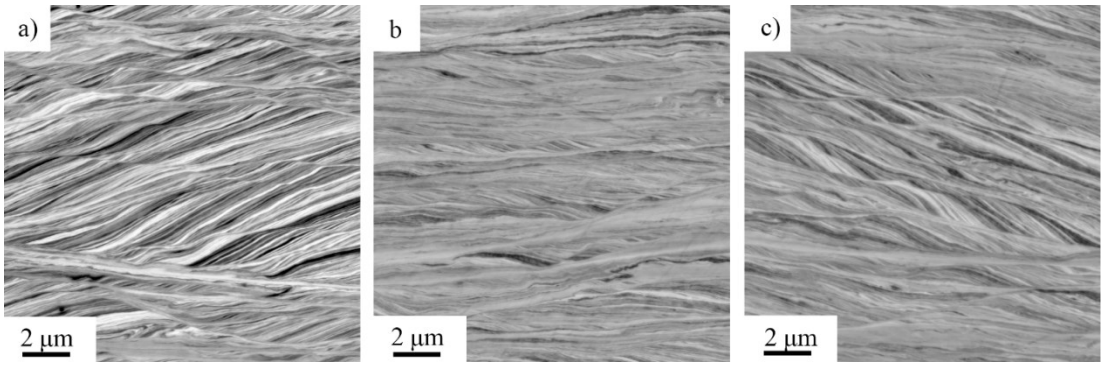

Figure V.6: BSE-SEM micrographs in radial direction for the Cu-37at%Ag composite. At an applied strain of γ~570 processed d) at RT, b) at LN temperature c) processed at RT for γ~380 and additionally for γ~190 at LN temperature revealing a stronger refinement after the LN processing compared to only RT deformation.

In earlier studies on a RT processed Cu-37at%Ag composite [13] it was shown in nanoindentation experiments that in the saturation regime C the nano-lamellar and the single-phase shear band regions exhibit no distinct differences in hardness and strain rate sensitivity. Because the grain size within shear bands is similar in regime B and C, it is plausible to assume that the hardness in these regions is similar irrespective of the applied strain. Thus a hardening in the shear bands in regime B cause a continuous formation of new shear bands until the hardness of the lamellar regions approaches the hardness of the shear bands in regime C. Then the deformation is mainly carried by a limited number of shear bands [13].

To explain the difference between RT and LN shear banding leading only at LN to complete single-phase microstructures, it is concluded that the difference in the hardness levels of the shear bands and lamellar regions is apparently more pronounced at LN temperature, leading at LN to progressive deformation of the lamellar matrix by shear bands until a homogeneous single-phase alloy is obtained.

This assumption is further supported by the results of split sample experiments in regime C, for details see [14]. For this purpose grids were cut by FIB into the polished sample cross-section in radial direction. The sample was deformed to an additional small applied strain together with a matching counterpart and analyzed by SEM before and after. A sample deformed to a total applied strain of γ~2500 was marked with FIB grids and deformed for two additional deformation steps at RT (Figure V.7a and b) and one step at LN temperature (Figure V.7c). The shear band carrying the deformation during the first RT step continued to carry the imposed strain in the second RT step, while in the last step at LN new shear bands were formed. This proves the above-raised assumption that the relative difference in strength between lamellar regions and shear bands as a result of lowering the temperature controls the shear band frequency and thus the final microstructure in the saturation regime.

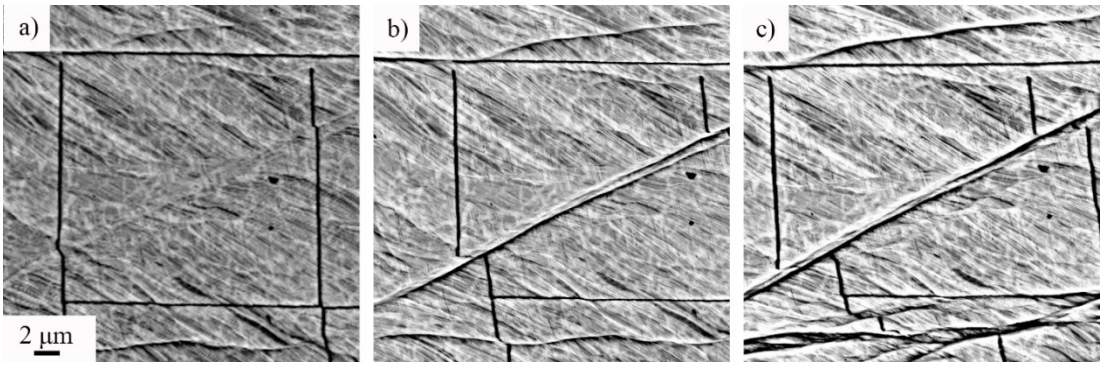

Figure V.7: SEM micrographs of Cu-37at%Ag composite split sample pre-deformed to an applied strain of γ~2500. A) after the first HPT step at RT with an additional strain of γ~1, b) after the second HPT step at RT for γ~0.33 and c) after the third HPT step conducted at LN temperature for γ~0.33.

V.3.2.2 Regime C

To study the deformation behavior at elevated processing temperatures in the saturation regime C in detail, another split sample experiment was used. A sample deformed at 200 °C to an applied strain of γ~1900 with a nanocrystalline dual-phase microstructure (see Figure V.4c) was HPT processed for an additional strain of γ~0.33 at 200 °C. During deformation the FIB grid was uniformly sheared, compare the as-cut grid (Figure V.8a) with the grid after the additional deformation step (Figure V.8b). In the upper right corner a single shear band is visible, which was generated during the compression at RT before the shear strain was applied. A sample deformed to the same strain level (γ~1900) at RT was also marked with FIB grids. Then it was first deformed for an additional strain of γ~1 at RT, and afterwards for γ~0.33 at 200 °C. During RT deformation the composite deformed mainly by shear bands, which can be seen from the stepwise distortion of the FIB grid in Figure V.8c. Applying an additional strain at 200 °C caused a change in the deformation behavior, the grid is homogeneously sheared, see Figure V.8d, comparable with the sample processed at 200 °C in Figure V.8b.

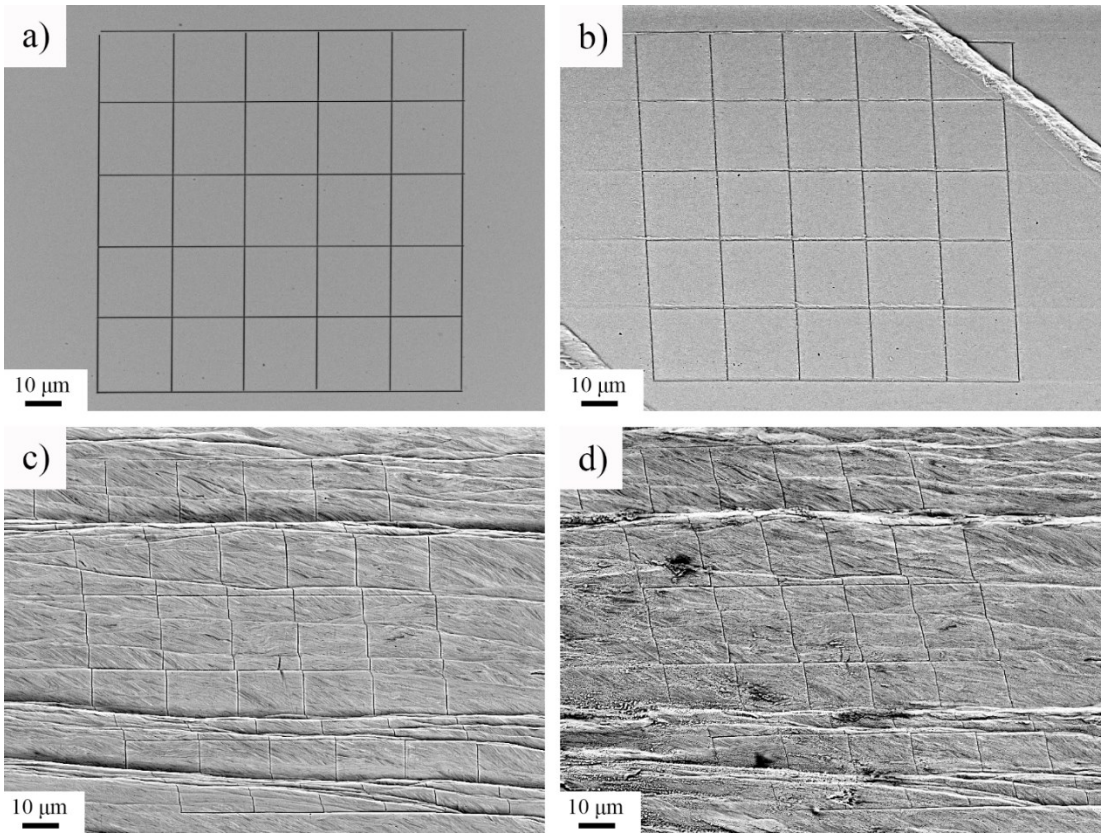

Figure V.8: SEM micrographs of split samples for the Cu-37at%Ag composite, a) as-cut FIB grid on a sample deformed to γ~1900 at 200°C with b) grid after an additional HPT deformation step of γ~0.33 showing uniform shear of the grid, c) FIB of a RT processed sample after an additional applied strain of γ~1 at RT identifying shear banding as main deformation mechanism and d) the same grid as in c) after an additional HPT step of γ~0.33 at 200°C revealing a change in deformation mechanism from shear banding to uniform shear.

V.3.3 Influence of composition and deformation temperature on the degree of supersaturation

Systematic synchrotron XRD measurements were performed on Cu-6/37/84at%Ag composites to evaluate the degree of supersaturation on a large scale as a function of applied shear strain and processing temperatures. The analyzed samples together with the obtained results are listed in Table V.1. The coherent domain sizes (CDS) and solute concentration of Cu are given for the Cu phase, the Ag phase and the newly formed solid solution phases.

Table V.1: Summary of the synchrotron XRD results for the Cu-6/37/84at%Ag composites for the Cu-phase, the Ag-phase and the formed supersaturated solid solution phases (solid sol.). Numbers in parentheses represent the errors.

	Shear	**Coherent domain size L (nm)**			**Solute concentration (at% Cu)**		
Cu-6at%Ag		Ag	Solid sol.	Cu	Ag	Solid sol.	Cu
5 rot RT	190	9.8 (1.1)		26.4 (8.9)	4		99.4
10 rot RT	380	4.0 (0.2)	3.0 (0.1)	15.9 (3.2)	8.6	86	98.8
20 rot RT	760		9.9 (1.2)			92	
50 rot RT	1900		11.6 (1.7)			92	
50 rot 100°C	1900		10.6 (1.4)			92	
50 rot 200°C	1900	3.4 (1.5)		12.1 (1.9)	7		96
50 rot 300°C	1900	18.6 (4.2)		46.3 (27.4)	3.6		99.8
Cu-84at%Ag		Ag	Solid sol.	Cu	Ag	Solid sol.	Cu
5 rot RT	190	26.6 (8.6)		12.7 (2.1)	1	11.8	99.6
10 rot RT	380	10.8 (1.4)	7.4 (0.7)	3.9 (0.2)	7	20	92
50 rot RT	1900		9.6 (1.1)			13	
50 rot 100°C	1900		7.6 (0.7)			13	
50 rot 200°C	1900	15.6 (2.9)		7.2 (0.7)	2.5		96.2
50 rot 300°C	1900	38.4 (17.8)		17.4 (3.8)	3.1		99.8
Cu-37at%Ag		Ag	Solid sol.	Cu	Ag	Solid sol.	Cu
5 rot RT	190	23.8 (8.2)		31.1 (14.7)	0		99
10 rot RT	380	14.9 (3.2)		28.9 (12.7)	0		99
50 rot RT	1900	4.6 (3)	3.4 (2)	8.5 (1.1)	7.8	66	95
100 rot RT	3800	4.1 (2)	4.2 (3)	11.2 (1.9)	6.8	62	94
5 rot 200°C	190	83.0 (99.0)		-	0		99
10 rot 200°C	380	21.2 (6.4)		26.1 (10.4)	0		99
50 rot 200°C	1900	18.1 (4.7)		26.3 (10.5)	0		98
10 rot LN	380	16.4 (3.9)		53.7 (43.9)	0		99
50 rot LN	1900		7.3 (0.8)		-	62	-
50 rot 300°C	1900	62.0 (55.1)		64.7 (63.8)	0		98

The synchrotron XRD patterns obtained for the Cu-6at%Ag composite at different strain levels for RT deformation and the highest strain level for processing at 100, 200 and 300 °C are displayed in Figure V.9. With increasing strain the intensity of the Ag peaks is reduced until it completely diminished at γ~760. Simultaneously a pronounced peak shift of the Cu phase was observed due to a change in lattice parameter induced by the dissolution of Ag atoms. Between γ~760 and γ~1900 no difference in the XRD patterns occurred implying that

the saturation was already reached at γ~760. At elevated deformation temperatures no change occurred up to 100 °C. At 200 °C the Cu peak position approached the peak position of the pure Cu indicating that phase separation took place. Nevertheless, about 7 at% Cu are still dissolved in Ag and 4 at% Ag in Cu, see Table V.1. At 300 °C the phases remain nearly completely decomposed as revealed from the XRD pattern with distinct Cu and Ag peaks, although as calculated from the lattice parameter change 3.6 at% Cu are dissolved in Ag, see Table V.1.

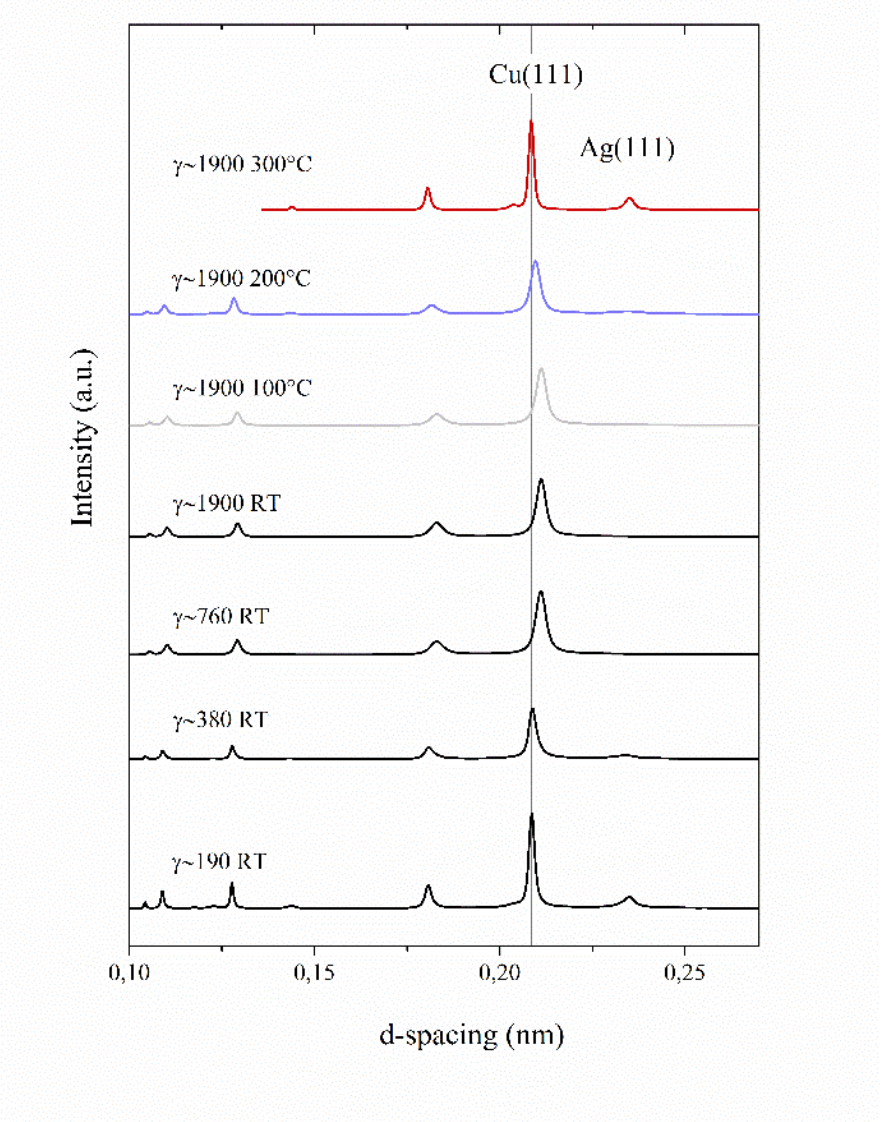

Figure V.9: XRD patterns recorded for the Cu-6at%Ag composite at different applied strain levels defromed at RT and at the highest applied strain for different deformation temperatures.

The XRD patterns recorded the Cu-37at%Ag composite on samples deformed at RT for different strains are summarized in Figure V.10. At the critical strain level for shear band formation, γ~190, distinct peaks of the Cu and the Ag phase are apparent. With increasing

strain gradual broadening of the Cu and Ag peaks was observed, compare XRD patterns for γ~190, 380 and 1130. At a strain of γ~1900 the newly formed supersaturated phase appeared. Additionally, the Cu and Ag phase peaks shifted towards larger and smaller d-spacings due to dissolution of Ag in Cu lamellae and vice versa. The partial supersaturation in the lamellar matrix was determined to about 7.8 at% Cu in the Ag phase and up to 5 at% Ag in the Cu phase, see Table V.1. A comparison of the XRD patterns for Cu-37at%Ag recorded on samples deformed to γ~1900 at LN, RT and 200 °C is presented in Figure V.11. In accordance with TEM analyses of samples deformed at LN temperature a complete single-phase supersaturated solid was formed, while at 200 °C a phase-separated composite was obtained. At RT an intermediate microstructural state was obtained with single-phase regions generated within shear bands and a partially supersaturated lamellar matrix.

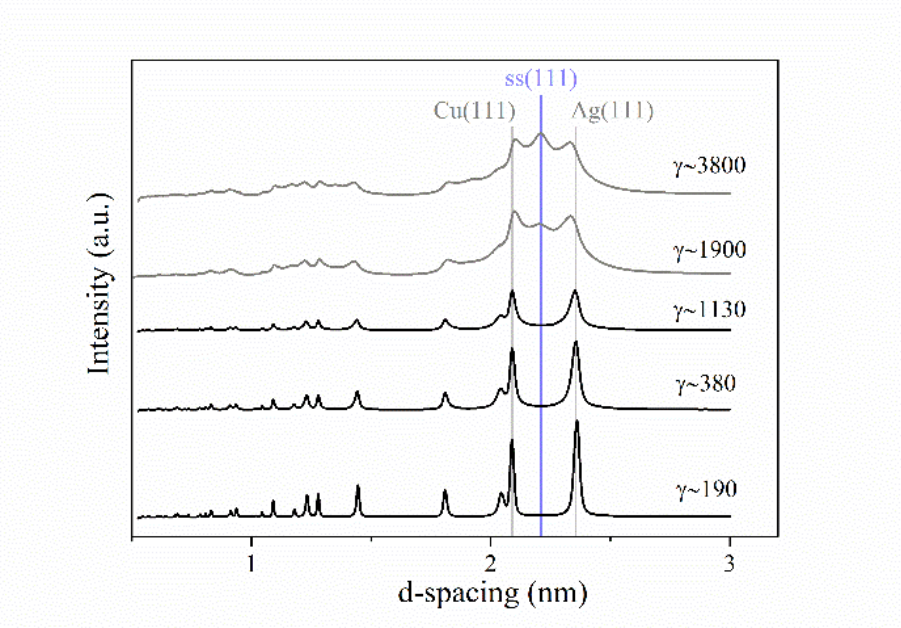

Figure V.10: Synchrotron XRD patterns recorded on Cu-37at%Ag samples deformed at RT to different strain levels. The 111 peaks of the Cu phase, the Ag phase and the supersaturated phase (ss) are indicated.

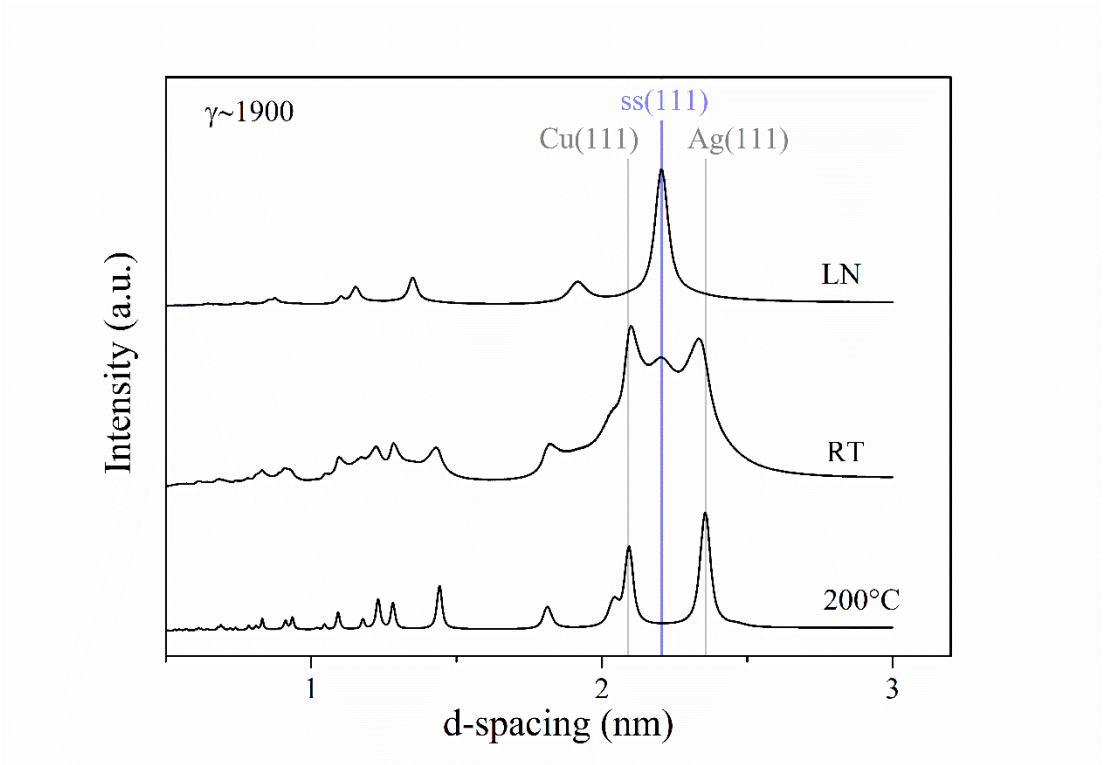

Figure V.11: Synchrotron XRD patterns of the Cu-37at%Ag composite recorded at and applied strain of γ~1900 for the LN, RT and 200 °C deformed sample. At LN a single-phase supersaturated solid solution was formed, at RT a composite of single-phase regions and partially supersaturated Cu and Ag phases was obtained and at 200°C a complete phase-separated composite of pure Cu and Ag was formed. The 111 peaks of the Cu phase, the Ag phase and the supersaturated phase (ss) are indicated.

The general trends in grain refinement in the Cu and Ag phases with increasing applied strain as shown in SEM and TEM micrographs are well reflected in the evolution of the CDS, although as commonly CDS gives much smaller values than TEM imaging, compare for example the CDS of 11 nm for the Cu-6at%Ag composite with the TEM micrograph in Figure V.2c. The CDS of the supersaturated phases, see Table V.1, however, exhibit an opposing evolution. The supersaturated phases, for Cu-6at%Ag, initially formed at γ~380, obtains a very small CDS of only 3 nm. With ongoing deformation the DCS increases to about 10 nm. Similar observations are made in the Cu-37at%Ag and Cu-84at%Ag at RT. Simultaneously with the gain in CDS the composition in the solid solution phase approaches the nominal composition of the composite, see Table V.1.

Figure V.12 compares the XRD patterns obtained for a Cu-50wt%Ag sample deformed at RT to γ~3800 and for a sample deformed first at RT for γ~3800 and subsequently for γ~1130 at LN temperature. Additional deformation at LN temperature led to homogenization of the composite towards a single-phase alloy, although residual peaks from the Cu- and Ag-phase are still existent, as indicated by arrows. This result further supports the assumption that during LN-processing a pronounced difference in hardness between shear band and lamellar regions exists leading to the successive transformation of lamellar structures into a single-phase state by shear bands.

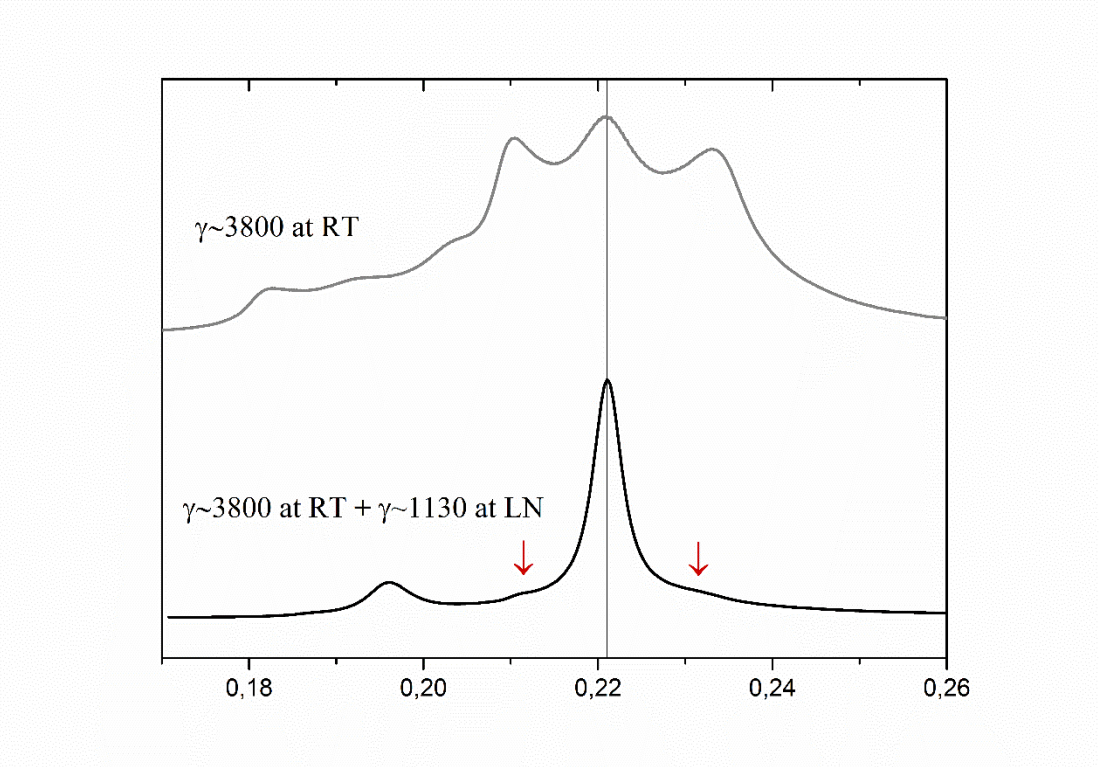

Figure V.12: Synchrotron XRD patterns measured on a sample deformed for γ~3800 at RT and for a sample deformed for γ~3800 at RT and subsequently for γ~1130 at LN temperature.

The obtained single-phase, dual-phase and multiphase microstructures are summarized in a "saturation phase diagram" in Figure V.13. Below a critical deformation temperature, which lies for the Cu-37at%Ag composite below RT and for the other investigated concentrations around 100 °C, complete supersaturation to single-phase alloys can be achieved.

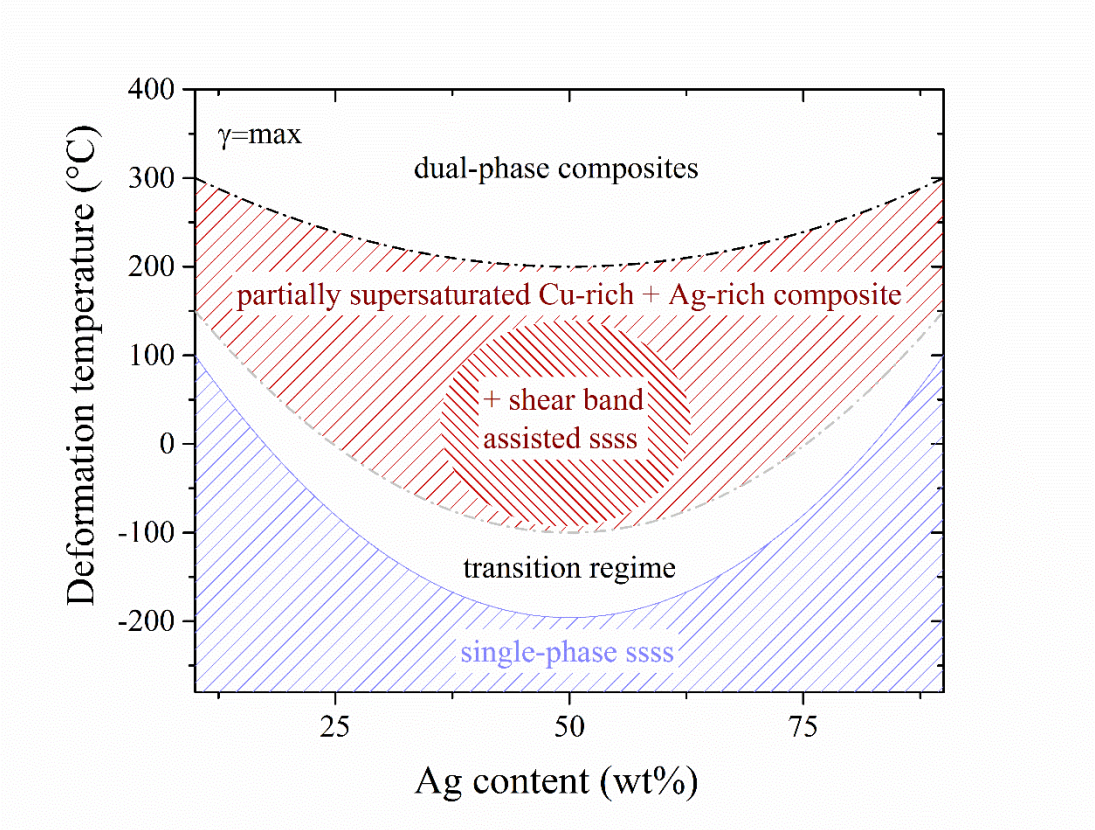

Figure V.13: "Saturation phase diagram" for the Cu-Ag system with a single-phase supersaturated solid solution (ssss) zone at low processing temperatures and a dual-phase pure Cu and Ag zone at elevated temperatures. In between a dual-phase zone with Cu- and Ag-rich solid solutions exists. Additionally, in the medium composition range a shear band assisted supersaturated solid solution with the nominal composition is formed leading to a tri-phase zone.

V.3.4 Deformation in the saturation regime

To maintain microstructural features as grain size, boundary length and boundary misorientation in the saturation regime, a dynamic equilibrium between grain refinement and restoration processes is required. During HPT deformation of Cu-Ag composites three different saturation microstructures are obtained.

Below a critical processing temperature depending on the composition complete single-phase supersaturated solid solutions are formed. It is plausible to assume that the mechanisms maintaining the microstructure in the saturation regime in these single-phase alloys are similar as in pure metals or conventional single-phase alloys [15].

In the Cu-37at%Ag composite between the single-phase region at low deformation temperatures and the phase-separated dual-phase regions at higher temperatures an intermediate microstructural state was observed. Processing at RT led to a composite consisting of Cu-rich, Ag-rich and supersaturated regions obtaining the global composition. In the saturation regime C the material deforms mainly by a limited number of shear bands preventing

further deformation of the rest of the materials and consequently hinders a homogenization of the microstructure.

At elevated deformation temperatures phase-separated composites are formed in all compositions. In the Cu-37at%Ag composition, a nanocomposite at 200 °C composed of separate Cu and Ag with a grain size between 50 and 100 nm evolved. Due to the nearly equal volume fraction of Cu and Ag, grains of one phase are isolated by grains of the other phase. To maintain this microstructure in the saturation regime several mechanisms could contribute. On the one hand grain boundary sliding, which is sometimes considered in ultrafine-grained or nanocrystalline grain size regimes, could realize the deformation. On the other hand a dislocation-based mechanism assisted by atom exchanges enabled by the high defect density such as vacancies or phase boundaries could occur. In this case an equilibrium between the continuous dissolution of grains, when their size is reduced below a critical level, and simultaneous diffusion of atoms back to their phase would prevail. However, the mechanisms responsible for retaining the microstructure during deformation at elevated temperatures in the saturation regime are still unclear.

V.3.5 Supersaturation process

The underlying mechanisms and key factors for deformation-induced supersaturation are still topic of controversial discussions in the material science community [5,7,16–19]. In general, there is no agreement if the atomic scale process is the same in different material systems or rather depends on the characteristics of each system.

However, most concepts coincide that the phase dimension has to fall below a critical level. The so-called kinetic roughening model proposed by Bellon and Averback [17] predicts an equilibrium between mechanical mixing and decomposition promoted by thermodynamic driving forces. The roughening of phase boundaries is realized by repeated dislocation glide events across the interfaces. In studies on Cu-10at%Ag alloys HPT-deformed at RT it was shown that the required imposed strain for complete supersaturation correlates linearly with the size of Ag precipitates [20]. Although not explicitly discussed, their XRD patterns show a similar evolution as in the present study. At lower applied strain a newly formed supersaturated phase is formed, while simultaneously a gradual increase of the mutual solubility is observed, see Table V.1. This experimental evidence indicates that at phase boundaries a zone of a supersaturated solid solution is formed in accordance with the kinetic roughening model. Atoms are then further transported from this zone into the grain interior enabled by the high defect density typically existent in SPD deformed materials until at higher strains homogenization to a single-phase alloys is completed. The chemical composition of the supersaturated phase formed at low strains differs from the nominal composition presumably due to an asymmetric decomposition behavior that is Ag atoms with a larger atomic radius diffuse back to the Ag phase easier.

With increasing deformation temperature the equilibrium between mechanical mixing and decomposition dictated by thermal diffusion shifts to more phase-separated states. In the Cu-6 and 84at%Ag composites this is observed at 200 °C, see Table V.1. In the Cu-37at%Ag, however, the mutual solubility at this temperature is much lower. This could be explained by the much shorter diffusion paths in the medium composition allowing easier decomposition. However, a comparison of the Cu-37at%Ag solid solutions formed at RT and LN indicates that the suppression of thermally activated decomposition at LN leads to a much more homogenous solid solution than at RT, where the very broad diffraction signals from TEM and XRD analyses indicate chemical fluctuations within the formed solid solution.

The present experimental findings could be also explained by the dislocation shuffling model of Raabe et al. [18]. They suggested a two-step mechanisms realized by repeated dislocation glide across phase boundaries on different planes resulting in the generation of small particles of one phase embedded in the other phase. In the following these particles are further reduced in size by dislocation cutting until they will dissolve eventually due to the Gibbs-Thomson effect. Studies by Gubicza et al. [21] found that a Ag precipitate size of 4 nm is required for dissolution at 350 °C. In general it is conceivable that small particles arise during the deformation and a Gibbs-Thomson effect accounts for the observed supersaturation.

However, the described mechanisms require that dislocation can cross phase boundaries and therefor the interfaces have to fulfill certain criteria as defined by Embury et al. [22]. First, the misorientation of the active slip systems in adjacent grains should be a minimum. Second, the configuration of the phase boundary should be one of minimum energy. And third, the resolved shear stress from dislocation pile-up should be a maximum. The latter requirement is fulfilled if the lamella thickness reaches a critical level, as shown for Cu-Nb by Misra and Hoagland [23]. This becomes especially clear from the Cu-37at%Ag composite, where at low applied strains no supersaturation in lamellar regions occurs and phase boundaries remain sharp even when the lamella thickness is below 10 nm (see reference [13]). In contrast, at high applied strains the retained lamellar matrix exhibits a mutual solubility of a few atomic percent causing a diffuse appearance of phase boundaries, see Figure V.4b and Figure V.5a and b.

Lastly, it must be noted that the dominating deformation mechanisms can strongly influence the supersaturation process. The shear band formation in the Cu-37at%Ag composite at RT prevents homogenization and leads to a multi-phase structure consisting of a Cu-rich, a Ag-rich and a supersaturated phase. In the composites with low and high Ag content instead, a more homogenous deformation results in single-phase supersaturated alloys.

V.4 Summary and conclusions

As summarized in Figure V.13 different material states were obtained after HPT processing of Cu-Ag composites to very high strains into a saturation regime. By varying the HPT processing temperature a transition from single-phase supersaturated solid solutions at low temperatures to completely phase-separated composites at elevated temperatures was observed. The temperature window for complete supersaturation strongly depends on the composition and accordingly the volume fraction of the constituent phases. In the Cu-6 and 84at%Ag composites it was found that homogenous deformation promotes the supersaturation process up to a critical processing temperature of 100 °C and single-phase alloys can be obtained. In Cu-37at%Ag inhomogeneous composites formed during RT deformation due to strong strain localization in form of shear bands. Inside the shear bands a supersaturated solid solution was formed, while the remaining matrix retained a nano-lamellar dual-phase structure. To achieve complete supersaturation to a homogenous single-phase alloy, a reduction of the processing temperature to LN was necessary. At processing at LN the deformation is governed by shear bands as well and the difference in shear band formation at RT and at LN was attributed to the different flow stress levels of the microstructural states in these composites depending on the temperature. At elevated temperatures the composites deformed by homogeneous shear independent of composition and thermodynamic driving forces cause a phase separation leading to nano-composites.

Acknowledgment

Funding of this work has been provided by the European Research Council under ERC Grant Agreement No. 340185 USMS.

References

[1] K. Uenishi, K.F. Kobayashi, K.N. Ishihara, P.H. Shingu, Formation of a supersaturated solid solution in the Ag-Cu system by mechanical alloying, Mater. Sci. Eng. A 134 (1991) 1342–1345.

[2] C. Gente, M. Oehring, R. Bormann, Formation of thermodynamically unstable solid solutions in the Cu-Co system by mechanical alloying, Phys. Rev. B. 48 (1993) 244–253.

[3] E. Ma, J.-H. He, P.J. Schilling, Mechanical alloying of immiscible elements: Ag-Fe contrasted with Cu-Fe, Phys. Rev. B. 55 (1997) 5542–5545.

[4] J. Xu, U. Herr, T. Klassen, R.S. Averback, Formation of supersaturated solid solutions in the immiscible Ni–Ag system by mechanical alloying, J. Appl. Phys. 79 (1996) 3935–3945.

[5] Z.C. Cordero, C.A. Schuh, Phase strength effects on chemical mixing in extensively deformed alloys, Acta Mater. 82 (2015) 123–136.

[6] D. Edwards, I. Sabirov, W. Sigle, R. Pippan, Microstructure and thermostability of a W-Cu nanocomposite produced via high-pressure torsion, Philos. Mag. 92 (2012) 4151–4166.

[7] X. Sauvage, P. Jessner, F. Vurpillot, R. Pippan, Nanostructure and properties of a Cu-Cr composite processed by severe plastic deformation, Scr. Mater. 58 (2008) 1125–1128.

[8] R. Pippan, S. Scheriau, A. Hohenwarter, M. Hafok, Advantages and limitations of HPT : a review, Mater. Sci. Forum. 584-586 (2008) 16–21.

[9] A.P. Hammersley, S.O. Svensson, M. Hanfland, A.N. Fitch, D. Häusermann, Two-dimensional detector software: From real detector to idealised image or two-theta scan, High Press. Res. 14 (1996) 235–248.

[10] A. Bachmaier, G.B. Rathmayr, M. Bartosik, D. Apel, Z. Zhang, R. Pippan, New insights on the formation of supersaturated solid solutions in the Cu–Cr system deformed by high-pressure torsion, Acta Mater. 69 (2014) 301–313.

[11] A. Bachmaier, H. Aboulfadl, M. Pfaff, F. Mücklich, C. Motz, Structural evolution and strain induced mixing in Cu-Co composites studied by transmission electron microscopy and atom probe tomography, Mater. Charact. 100 (2015) 178–191.

[12] K.S. Kormout, B. Yang, R. Pippan, Deformation Behavior and Microstructural Evolution of Cu-Ag Alloys Processed by High-Pressure Torsion, Adv. Eng. Mater. (2015) 1828–1834.

[13] K.S. Kormout, P. Ghosh, V. Maier-Kiener, R. Pippan, Deformation mechanisms during severe plastic deformation of a Cu-Ag composite, J. Alloys Compd. (2016) accepted for publication.

[14] M. Hafok, R. Pippan, Post-shear deformation of high pressure torsion-deformed nickel under hydrostatic pressure, Scr. Mater. 56 (2007) 757–760.

[15] O. Renk, A. Hohenwarter, S. Wurster, R. Pippan, Direct evidence for grain boundary motion as the dominant restoration mechanism in the steady-state regime of extremely cold-rolled copper, Acta Mater. 77 (2014) 401–410.

[16] J. Eckert, J.C. Holzer, C.E. Krill III, W.L. Johnson, Mechanically driven alloying and grain size changes in nanocrystalline Fe-Cu powders, J. Appl. Phys. 73 (1993) 2794–2802.

[17] P. Bellon, R.S. Averback, Nonequilibrium Roughening of Interfaces in Crystals under Shear: Application to Ball Milling, Phys. Rev. Lett. 74 (1995) 1819–1822.

[18] D. Raabe, S. Ohsaki, K. Hono, Mechanical alloying and amorphization in Cu–Nb–Ag in situ composite wires studied by transmission electron microscopy and atom probe tomography, Acta Mater. 57 (2009) 5254–5263.

[19] A. Bachmaier, J. Schmauch, H. Aboulfadl, A. Verch, C. Motz, On the process of co-deformation and phase dissolution in a hard-soft immiscible Cu-Co alloy system during high-pressure torsion deformation, Acta Mater. 115 (2016) 333–346.

[20] S.N. Arshad, T.G. Lach, M. Pouryazdan, H. Hahn, P. Bellon, S.J. Dillon, R.S. Averback, Dependence of shear-induced mixing on length scale, Scr. Mater. 68 (2013) 215–218.

[21] J. Gubicza, Z. Hegedüs, J.L. Lábár, V.S. Sarma, A. Kauffmann, J. Freudenberger, Microstructure evolution during annealing of an SPD- processed supersaturated Cu–3 at.% Ag alloy, IOP Conf. Ser. Mater. Sci. Eng. 63 (2014) 012091.

[22] C.W. Sinclair, J.D. Embury, G.C. Weatherly, Basic aspects of the co-deformation of bcc/fcc materials, Mater. Sci. Eng. A 272 (1999) 90–98.

[23] A. Misra, R.G. Hoagland, Plastic flow stability of metallic nanolaminate composites, J. Mater. Sci. 42 (2007) 1765–1771.